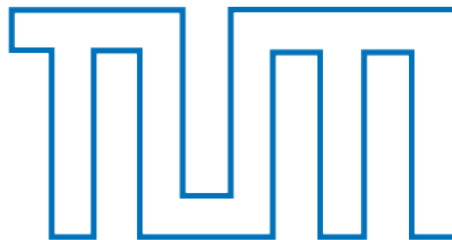# Background Suppression through Pulse Shape Analysis in the DEAP-3600 Dark Matter Detector

April 3, 2018

Master's thesis submitted by
**Paul Moritz Burghardt**

Supervisor:
**Dr. Tina Pollmann**

First corrector:
**Prof. Dr. Stefan Schönert**



Department of Physics,
Technical University of Munich

**Abstract**

DEAP-3600 is a dark matter direct detection experiment in SNOLAB, Canada, using a single phase liquid argon target. Upon energy deposition of ionising particles, liquid argon emits light through the decay of a short-lived singlet state and a long-lived triplet state with a lifetime of approx 1400 ns. In DEAP-3600 this makes up the only DM-signal which is detected by an array of 255 photomultiplier tubes. In order to reach its projected sensitivity to WIMP-nucleon cross sections of $10^{-46}$ cm$^2$ for 100 GeV WIMPs, its electronic recoil background dominated by the beta-decaying $^{39}$Ar has to suppressed by a factor of $10^{-8}$. This is achieved through pulse shape discrimination (PSD): electronic recoils produce a different singlet to triplet dimer ratio than the WIMP-nuclear recoil signal and therefore have a distinct time structure. In this work, prompt-window-based and likelihood-based PSD-parameters are presented and evaluated using their discrimination power in DEAP-3600.

# Contents

# 1 The search for dark matter

## 1.1 Dark matter in the universe

The most well-known evidence for dark matter comes from the measurement of rotational velocities of stars within spiral galaxies. Here, stars generally move on stable circular orbits around the galactic centre, which requires the centrifugal force $\frac{mv^2}{r}$ to be equal to the gravitational force. Because gravitation is a central force, the gravitational force for stars at a given radial distance from the center $r$ only depends on the mass contained in the disk $0 < r' < r$, $M(r) = \int_0^r \rho(r')dr'$, where $\rho(r')$ is the radial density profile of the galaxy. By setting both forces equal an expression can be found for the rotational velocity $v$:

$$v(r) = \sqrt{\frac{GM(r)}{r}}.$$

(1)

The radial distance and rotational velocity of stars as well as the visible mass profile of the galaxy can be inferred from observations. It results that the rotational velocities are much greater than expected from equation 1, indicating mass contributions from invisible (dark) matter (DM) [1].

Another strong line of evidence for the existence of dark matter was found in 2006 by observation of the two colliding clusters of galaxies, typically referred to as the Bullet Cluster [2]. Here, the effective mass distribution within the cluster estimated through gravitational lensing was found to severely differ from the visible mass distribution. The DM-hypothesis is also consistent with interpretations of precise measurements of the Cosmic Microwave Background by the Planck telescope [3].

A number of restrictions can be imposed on dark matter and the particle(s) it is composed of. Dark matter has to make up for a larger share of the universe's energy content than visible matter, 27 % overall. It's lack of visibility suggests that it only interacts weakly. In order to allow for structure formation and concentrate in galaxies it also has to be cold and stable.

There are a variety of models that intend to explain the phenomena above without the assumption of non-baryonic dark matter. These include alternative theories of gravity (e.g. MOND) and non-luminescent baryonic matter such as dark holes, neutron stars and white and brown dwarfs, commonly referred to as Massive Compact Halo Objects (MACHOs). Among others, the bullet cluster measurement suggest that MACHOs are unlikely to account for large amounts of dark matter in the universe [4].

An unknown particle beyond the standard model that comprises all the above is the Weakly Interacting Massive Particle (WIMP). It is electrically neutral, only interacts via the weak interaction and has a mass loosely between 10 GeV and 1 TeV. WIMPs belong to the most supported DM candidates with there being suitable well-motivated candidates within popular beyond-the-standard-model theories such as the neutralino in Supersymmetry theory. Another, much lighter candidate is the axion [5].

## 1.2 Dark matter detection principles

There are a variety of avenues to detect DM and efforts have been made for over 20 years to detect it. Some experiments have claimed WIMP detection, however, these findings are inconsistent with the results of newer experiments with higher sensitivities. This indicates the tremendous challenge of distinguishing a weak dark matter signal from a variety of background sources in these experiments.

Collaborations like ATLAS are searching for dark matter by looking at collider events. In proton-proton collisions a variety of particles are produced and detected. As WIMPs are expected to escape the detector undetected, a produced WIMP would yield in a large missing momentum. So far, no WIMP-production was indicated by these measurements [6].

Indirect detection experiments try to measure DM particle decay or annihilation by measuring their decay products. IceCube e.g. is using a large ice target to detect multi-GeV neutrinos which could originate from dark matter annihilating in the sun [7]. The Fermi Gamma Ray Space Telescope looks for features in the cosmic gamma ray spectrum that could originate from DM-annihilation [8].

Strong limits on the WIMP-nucleon cross section are currently achieved by direct detection experiments. Here, a target medium is set up on earth such that energy depositions of WIMPs in the target can be detected. These manifest in scintillation, ionisation, heat production, or a combination of the prior. Because of the low expected number of these events, detectors are operated for years and backgrounds (i.e. events originating from any other source) have to be suppressed to an extremely high degree. This involves both careful detector construction with highly radiopure materials as well as mechanisms to tag events as background or signal on an event-by-event basis.

Examples include CRESST which measures phonons and scintillation light and uses the ratio as a parameter to discriminate between signal and background [9]. Another example is PICO which uses the principle of a bubble chamber to detect WIMPs [10].
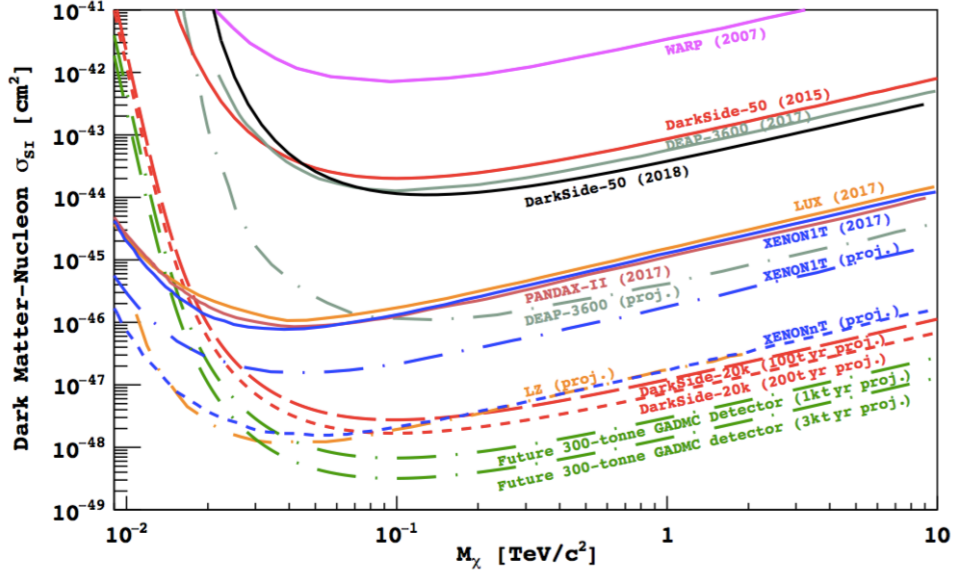
Figure 1: WIMP-Exclusion curves from current and planned argon and xenon experiments (taken from [11]).

Liquid noble gases, specifically neon, argon, and xenon, are a suitable DM detection medium and different direct detection experiments measure the scintillation and ionization yield that is caused by WIMPs in these target materials. Many of these are operated in a dual-phase (liquid + gas) or TPC (Time Projection Chamber) setup. Here, through application of an electric field, electrons freed by a WIMP-nuclear-recoil are accelerated towards the gas, causing a secondary light signal to the primary scintillation yield through gas discharge. The ratio between the primary and secondary signal carries information about the type of particle that caused the event and is used for background rejection. Another advantage is the strong achievable position reconstruction which can be used to tag events from e.g. radioactive material in the detector walls. Both argon (e.g. DarkSide, ArDM, WArPs) and xenon (e.g. XENON, LUX, PandaX) are commonly used as targets in TPCs. This technology currently achieves the strongest limits among DM experiments with XENON1T (see figure 1).

Argon offers background rejection in a simple single-phase setup without external fields through pulse shape discrimination (PSD). Here, freed electrons recombine and contribute to the scintillation yield, which makes up the only signal channel. This setup is used by DEAP collaboration.

Because the exposure to dark matter scales linearly with the detector mass in the absence of backgrounds, larger detectors are planned by many of the collaborations above to explore lower WIMP-nuclear cross sections. DEAP started with a 7 kg liquid argon (LAr) prototype (DEAP-1) to demonstrate the potential of PSD in a single-phase argon target [12] and currently operates a single-phase 3600 kg liquid argon detector. A 20 tonne-LAr TPC is planned as the next generation liquid argon detector [13].

## 1.3 WIMP flux and exclusion curve

Direct detection dark matter experiments typically put limits on the WIMP-nuclear cross section as a function of WIMP mass. Several assumptions enter such limit curves such as WIMPs accounting for the full DM content of our universe. Assumption like this have to be made as the calculation of a cross section requires knowledge of the WIMP-number density. A mass density of 0.3 GeV/cm$^3$ is inferred from cosmological considerations and hence a number density for a given WIMP mass can be calculated [14]. In principle, the WIMP mass also alters the WIMP-nuclear recoil spectrum, however due to the low number of expected events given the current leading limits it is hard to make meaningful statements about the shape of the spectrum.

The energy-deposition mechanism for WIMPs that direct detection experiments are sensitive to is elastic scattering with a nucleus, i.e. a nuclear recoil. Assuming a nuclear form factor of 1, in the center-of-momentum frame the WIMP scatters off a nucleus through an angle $\theta$, with $\cos\theta$ uniformly distributed between -1 and 1. If the WIMP's initial energy in the lab frame is $E_i = M_\chi \frac{v^2}{2}$, the nucleus recoils with energy $E_R = E_i r(1 - \cos\theta)$ with $r = 4\frac{M_\chi M_A}{(M_\chi + M_A)^2}$, where $M_A$ is the mass of the target nucleus. $E_R$ for a given $E_i$ is therefore uniformly distributed between 0 and $rE_i$ and values from $E_R/r$ to $\infty$ contribute to a $E_R < rE_i$. The recoil spectrum $\frac{dR}{dE_R}$ can then be calculated with $\int_{rE_i}^{\infty} \frac{dR(E_i)}{E_i r}$, where $1/(E_i r)$ normalises the uniform distribution.

In order to obtain the distribution for $E_i$ we assume that the WIMP's velocities in the frame of the galaxy follow the Maxwellian distribution. For direct detection experiments the velocities then have to be corrected for earth's velocity relative to the galaxy $v_E$.

$$f(\vec{v} + \vec{v}_E) \sim e^{(\vec{v} + \vec{v}_E)^2 / v_0^2} \tag{2}$$

where $v_0 = 220 \pm 20$ km/s is the local orbiting speed. The contribution from a velocity $\vec{v}$ to the event rate per target nucleus is then

$$dR = \sigma n_\chi f(\vec{v} + \vec{v}_E) v \mathrm{d}^3 \vec{v}. \tag{3}$$

Here, $n_\chi =$ is the WIMP number density. It is instructive (and reasonably accurate, as shown in [14]) to consider the simplified case of ignoring the earth's velocity and the galaxy's escape velocity (i.e. integrating the velocity distribution from 0 to $\infty$). With $E_0 = M_\chi \frac{v_0^2}{2}$ the energy spectrum can now be calculated

$$\int_{E_R/r}^{\infty} \frac{dR}{E_i r} \quad = \quad \int_{E_R r}^{\infty} \frac{1}{(\sqrt{\pi}v_0)^3} \sigma n_\chi v \frac{1}{M_\chi v^2/2r} e^{v^2/v_0^2} (4\pi v^2 \mathrm{d}v) \tag{4}$$

$$= \quad \frac{2v_0 \sigma n_\chi}{\sqrt{\pi}E_0^2 r} \int_{E_R/r}^{\infty} e^{-E_i/E_0} \mathrm{d}E_i \tag{5}$$

$$= \quad \frac{2v_0 \sigma n_\chi}{\sqrt{\pi}E_0 r} e^{-E_R/E_0 r}. \tag{6}$$
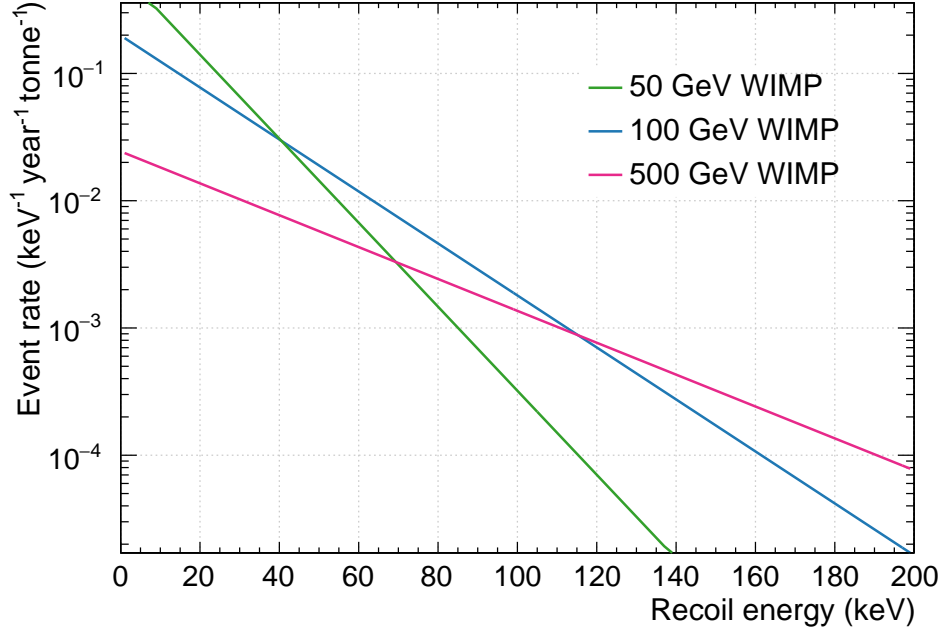


Figure 2: WIMP recoil spectrum from equation 6 in argon for $M_\chi = 50$ GeV, 100 GeV and 500 GeV

**Example for a DEAP-like detector**  Figure 2 shows the WIMP spectrum obtained from this simple model for a WIMP mass of 100 GeV. The mean recoil energy increases with the WIMP mass, e.g. for an argon target on earth ($M_A = 37.21$ GeV, $v_0 = 7.3 \cdot 10^{-4}c$) the mean recoil energy $E_0 r$ for a 50 and 100 GeV WIMP is 13 keV and 21 keV, respectively. Using a more realistic model by introducing a finite escape velocity of 540 km/s alters the recoil spectrum only slightly and produces a cut-off at 100 keV. Since the energy spectrum follows a falling exponential, a low energy threshold is critical to being sensitive to WIMPs. For example, for a 100 GeV-WIMP, the detection efficiency at energy thresholds of 40 keV, 60 keV and 80 keV is 15 %, 6 % and 2 %.

Integrating the spectrum above from $E_{\mathrm{thr}}$ to infinity gives the expected number of WIMP events $N$, assuming that above $E_{\mathrm{thr}}$ all WIMPs are detected. Solving for $\sigma$ yields

$$\sigma = \frac{\sqrt{\pi}N}{2v_0 T n_i n_\chi} e^{E_{\mathrm{thr}}/E_0 r}, \tag{7}$$

where $n_i$ is the number of target nuclei and $T$ is the detector lifetime. Typically, the excluded cross

section at 90% confidence level is cited (such as in e.g. figure 1), i.e. the cross section at which the experiment in 90% of cases would have measured more WIMP-like events than it actually did. In a detector with zero expected backgrounds and zero measured WIMP-like events, this number of events $N_{90\%\ \text{C.L.}}$ is with Poisson statistics $P(N_{90\%\ \text{C.L.}} > 0) = 0.9 \rightarrow P(N_{90\%\ \text{C.L.}} = 0) = 0.1 \rightarrow \exp(-N_{90\%\ \text{C.L.}}) = 0.1 \rightarrow N_{90\%\ \text{C.L.}} = 2.3$. Using formula 7, this can be converted into a limit on the cross section. With the simplified model above using a 3 tonne argon target and an energy threshold of 60 keV this corresponds to $\sigma_{90\%\ \text{C.L.}} = 1 \cdot 10^{-46}$ for a runtime of 3 years.

Because this work is focused on the reduction of a background to the WIMP signal, it is instructive to study the implications of a background on the excluded cross section. For example, if in the same experiment 10 background events are predicted and 10 events are observed, the excluded cross section at 90% confidence level would be $\sigma_{90\%\ \text{C.L.}} = 2.5 \cdot 10^{-46}$ or more than double as high as in the prior example. This is because the larger total number of total events (background + signal) $n$ increases the statistical uncertainties on the number of WIMP-events by $\sqrt{n}$. Therefore, in particular backgrounds with a high rate have to be discriminated, i.e. excluded from the WIMP search in order to achieve a competitive sensitivity, even if that means that a fraction of potential WIMP events will also be falsely classified as background.

## 2 Argon as a dark matter detection medium

Natural argon consists to $> 99.99\%$ of the stable isotopes $^{36}$Ar, $^{38}$Ar, $^{40}$Ar, with an $^{40}$Ar abundance of 99.6 % and is typically obtained by distillation of atmospheric gas. It also includes a $(8.0 \pm 0.6) \cdot 10^{-16}$ fraction of beta-decaying $^{39}$Ar with a lifetime of 269 years (equivalent to a rate of $(1.01 \pm 0.08)$ Bq per kg of natural argon) [15]. The $^{39}$Ar beta-spectrum has its endpoint at 565 keV [16].

| | |
|---|---|
| melting point (at 1 bar) | -189.35 C (83.80 K) |
| boiling point (at 1 bar) | -185.9 C (87.30 K) |
| density at 0 C | 1.784 g/l |
| density at -186 C | 1.4 kg/l |

Table 1: Properties of argon [17].

Gaseous, liquid and solid argon scintillates upon incident ionizing particles through the production of excited dimers ($Ar_2^*$-excimers) which ultimately decay under photon emission. Argon excitons $Ar^*$ are produced either directly or indirectly by ionization and recombination:

$$Ar^+ + Ar+ \rightarrow Ar_2^+ \tag{8}$$

$$Ar_2^+ + e^- \rightarrow Ar^{**} + Ar \tag{9}$$

$$Ar^{**} \rightarrow Ar^* + \text{heat} \tag{10}$$

This process is estimated to take about 500 ps. Light is then produced via

$$Ar^* + Ar + Ar \rightarrow Ar_2^* + Ar \tag{11}$$

$$Ar_2^* \rightarrow 2Ar + h\nu. \tag{12}$$

Here, $h\nu$ is a UV photon and it is assumed that each excited argon dimer $Ar_2^*$ emits a single photon. Argon dimers can be produced in either a short-lived singlet or a long-lived triplet state. In the liquid, the emission for both states is dominated by a peak at 128 nm with a width of approximately 10 nm [18]. Argon is transparent to the UV light which allows for good scalability of LAr detectors [19]. The argon scintillation properties vary under the type of interaction which excites the argon. Here, one distinguishes between electronic and nuclear recoils. In an electronic recoil a particle scatters with an electron in the shell of an argon atom. In a nuclear recoil a particle imparts some of its energy into the argon nucleus. Nuclear recoils are the main interaction channel for neutrons and WIMPs, whereas gammas and betas mainly interact via electronic recoils. Some of the different scintillation properties of argon under both excitation types are believed to be due to the higher linear energy transfer (LET) of nuclear recoils [18].

The average energy required to produce a single 128 nm or 9.7 eV-photon in an electronic recoil event is 19.5 eV [20]. The light yield is found to be heavily reduced under high deposited energy densities or LETs of the ionizing particle. A proposed non-luminescent deexcitation-mechanism under high exciton densities is

$$Ar^* + Ar^* \rightarrow Ar + Ar^+ + e^-, \tag{13}$$

sometimes referred to as biexcitonic quenching [21]. The electron and ion can recombine and emit a single photon instead of two for the two excitons. It was measured that for nuclear recoils the effective scintillation light yield is $0.29 \pm 0.03$ times the light yield for electronic recoils for 6 keV electronic recoils [22]. The corresponding quenching factor for alpha particles is 0.74. In this work the energy unit $keV_{ee}$, i.e. the estimated event energy under the assumption that the event is an electronic recoil is used.

The fraction of singlet excimer states was found to be higher at high LET [18]. Most notably, above 100 $keV_{ee}$ about 75 % of excimers are produced in the singlet state for nuclear recoils vs 25 % for electronic recoils. The resulting difference in the time structure of the scintillation yield is big enough to

allow for particle type identification on a event-to-event basis (pulse shape discrimination). The precise singlet-to-triplet ratios also depend on the particle energies and have been measured, among others, by the SCENE collaboration for nuclear recoils [23] and the CLEAN collaboration for electronic recoils [24]. The lifetimes of the argon dimers themselves are independent of the type of excitation [18].

Literature values for the triplet lifetime range from 1300 to 1600 ns [12, 18, 24, 25]. The form of the argon scintillation pulse shape also suggests the existence of an intermediate decay component with a lifetime of around 40 ns and intensity of 10% which has been discussed for several years [26]. The effective triplet lifetime strongly decreases as argon purity deteriorates. This can be explained by non-luminescent deexcitation of $Ar_2^*$ excimer states through collision with these impurities, e.g. for nitrogen:

$$Ar_2^* + N_2 \rightarrow 2Ar + N_2 + \text{heat}. \tag{14}$$

With a constant nitrogen contamination this deexcitation channel can be modelled with a simple rate law that competes with the radiative deexcitation. This results in a light yield and triplet lifetime decrease and was quantified for nitrogen in [27, 28] and oxygen contamination in [29]. Triplet excimers are more exposed to this process than singlet excimers due to their smaller radiative decay rate. Therefore, high purity of argon is of upmost importance for PSD, as it relies on the large difference in singlet and triplet lifetimes.

# 3 The DEAP-3600 experiment

## 3.1 Detector overview

DEAP is using a single phase liquid argon target to directly detect WIMPs which makes it unique in the otherwise TPC-dominated liquid scintillator dark matter search landscape. It was designed for a target mass of 3600 kg and an energy threshold of 60 keV or 17 $keV_{ee}$ for nuclear recoils. The projected sensitivity to the WIMP-nucleon cross-section is $10^{-46}$ cm$^2$ for 100 GeV WIMPs [30].
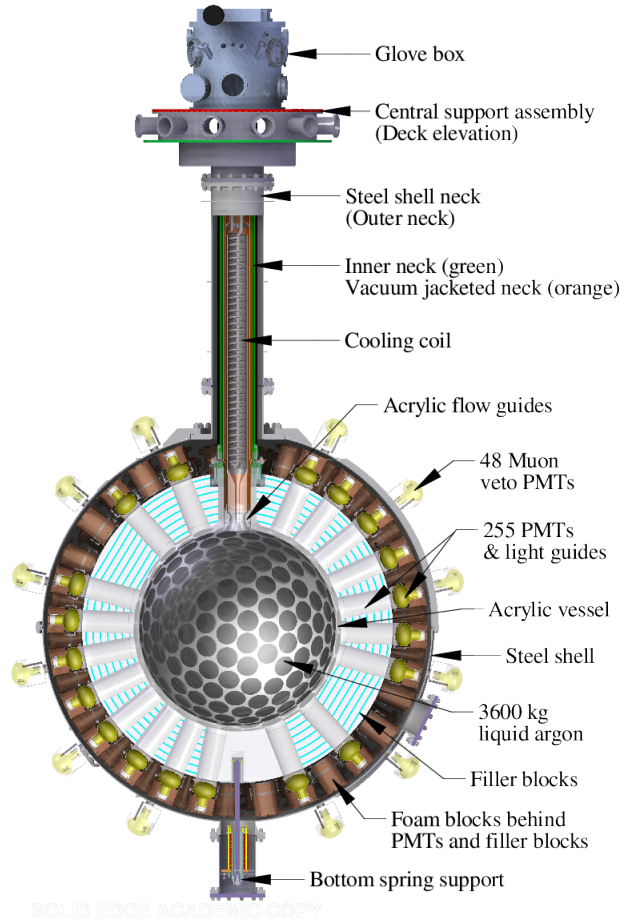
Figure 3: The DEAP-3600 detector design showing the acrylic vessel, light guides, and filler blocks, steel shell, neck, and glove box (taken from [30]).

The detector is located 2 km underground in SNOLAB, Canada. Figure 3 shows an illustration of the detector. The liquid argon is contained in a spherical vessel made of acrylic (plastic) with a radius of 85 cm. Advantages of acrylic include its high achievable radiopurity and its high concentration of hydrogen, which acts as a neutron shield. It also tolerates a large thermal gradient which allows for photomultiplier tube (PMT) operation at room temperature on the outer detector shell. The 255 Hamamatsu R5912 high quantum efficiency PMTs used for light detection are connected to the Argon by 45-cm long acrylic light guides. A thin layer of 1,1,4,4-tetraphenyl-1,3-butadiene (TPB) is applied to the inner surface of the acrylic vessel to shift the argon scintillation photons to the peak-efficiency-wavelength of the PMTs.

The target volume can be accessed through a vertical tube (neck). Cooling of the argon is achieved through a liquid nitrogen filled cooling coil reaching down the neck. The detector is enclosed in a stainless steel vessel. The steel vessel is submerged in ultra-pure water which is used as a muon veto target and viewed by 48 PMTs on the outer vessel side. Radioactive calibration sources can be placed close to

12

the detector through tubes inside of the water tank as shown in figure 13.

Because of an overfill and consecutive nitrogen leakage during the first fill attempt, the acrylic sphere was not fully filled with argon during the consecutive argon fill. For all data discussed in this work, the argon target mass is approximately 3300 kg.

## 3.2   Photomultiplier tubes

Photomultiplier tubes (PMTs) are sensitive light detectors that allow for single photon counting.
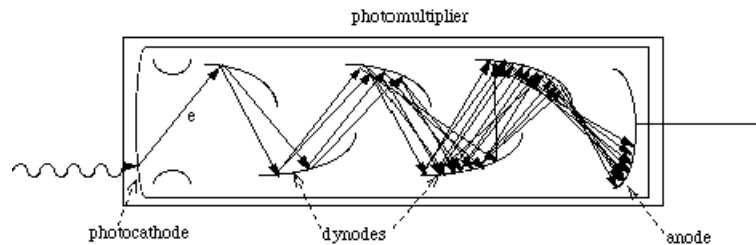


Figure 4: Illustration of the PMT work principle taken from [31].

A simplistic illustration of a PMT is shown on figure 4. A cathode, several dynodes and an anode are arranged in a vacuum as shown. Incident photons strike the cathode and eject electrons due to the photoelectric effect. These electrons are then consecutively accelerated towards a cascade of dynodes, where upon each impact more electrons are emitted. The amplified electron charge is collected by the anode and the resulting current is measured.

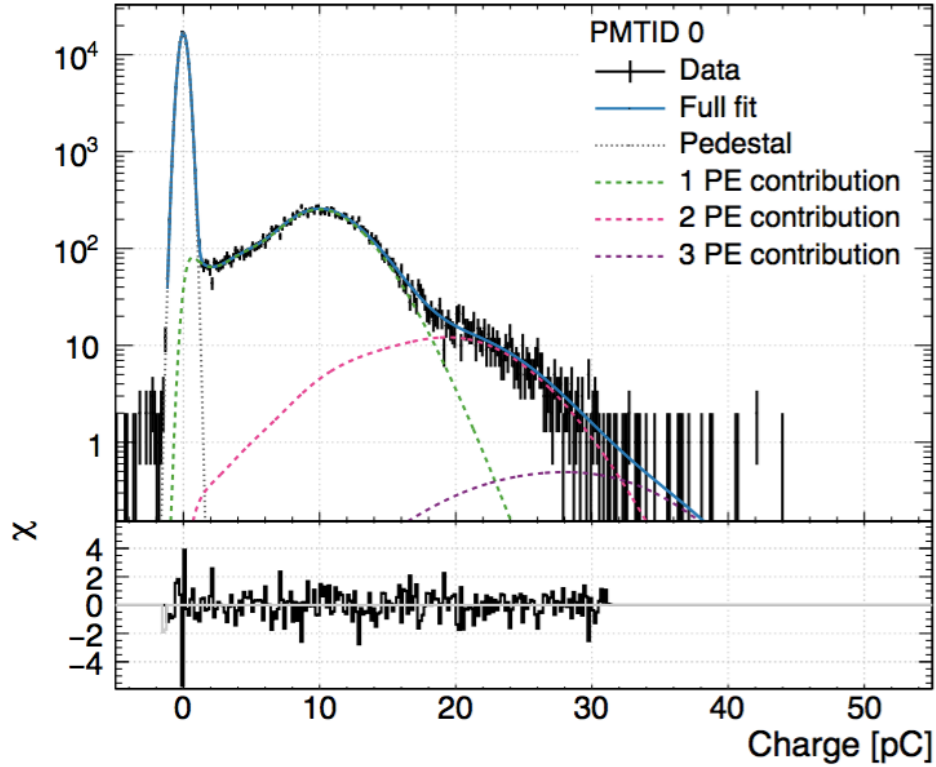Figure 5: The low light charge distribution for PMT 0 with the model and its components is shown. The figure is taken from [32], where also the model is discussed in detail.

Ultimately, the collected charge is only an arbitrary unit and the physical quantity of interest is the number of photons producing the charge. To obtain an estimate of this number, a charge calibration is performed for each PMT. Figure 5 shows the low light charge spectrum for a single PMT used in DEAP-3600. The spectrum is the sum of contributions from different discrete numbers of photoelectrons (PE). The large peak at low charge is referred to as pedestal and represents charge fluctuations due to noise. Using a sophisticated fit the average charge produced by a single photoelectron (SPE) can be determined for each PMT. One standard energy measure used in this work is the charge collected normalised by the SPE-charge of the corresponding PMT and referred to as $Q$ with unit QPE.

With a certain rate a PMT signal can be measured in the absence of light. This is due to thermionic emission of electrons inside the tube and referred to as dark rate [33]. This effect can also be observed in the DEAP-3600 PMTs, however, in DEAP, the dark rate is dominated by 'stray light', i.e. light from prior events which is detected at a delay, as most of the PMTs are too cold for thermionic emission.
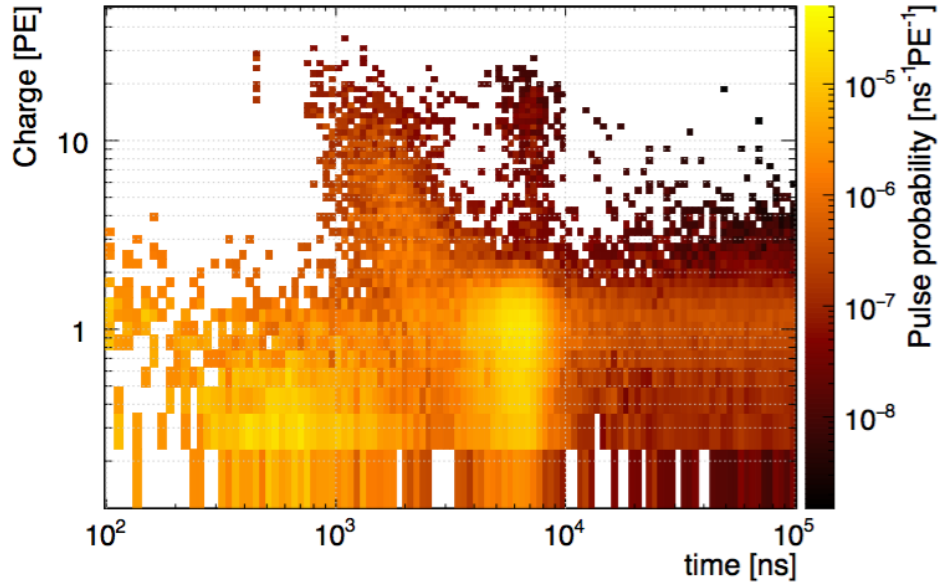
Figure 6: The measured probability for a typical PMT to observe a pulse following a primary pulse as a function of both the second pulse's charge (in units of the mean SPE charge) and of time. The primary pulses were required to have a charge between 10 pC and 14 pC in this example taken from [32].

There is a low (typically 1 - 10%) probability for a PMT to produce a signal several hundreds of ns to a few µs after an initial pulse. This is caused by residual gas in the tube and is referred to as afterpulsing: accelerated electrons in a primary pulse can hit and ionise a residual gas molecule in the vacuum tube. The ionised molecule is then accelerated towards a dynode, where upon impact it ejects electrons causing a secondary pulse. The delay of the second pulse is positively correlated to the inertia of the ionised molecule [34]. For DEAP-3600 an in-situ afterpulsing calibration is conducted: a light flash was induced through a LED calibration system in the inner detector and the time and charge of pulses following the initial pulse was measured. The probabilities for a secondary pulse as a function of their charge and time delay are shown in figure 6. This measurement is used for both pulse shape validation, simulations and an afterpulsing removal algorithm as described later.

## 3.3   DAQ & data flow

The data acquisition system (DAQ) records the signals of the 255 inner PMTs, the 4 PMTs in the neck forming a veto-system and the 48 muon veto PMTs viewing the water tank. This work focuses on the scintillation signal of the inner PMTs which is sampled at 250 MHz. Due to the high corresponding data rate, data is not digitized and written continuously. A trigger module computes rolling integrals of the PMT signals and adds them over all PMTs. Given this information the digitizers are triggered such that a large share of $^{39}$Ar beta decays are not digitized while keeping all events in the WIMP region of interest. The trigger information is always recorded. The data is stored in a DEAP-specific data structure and saved in ROOT data format.
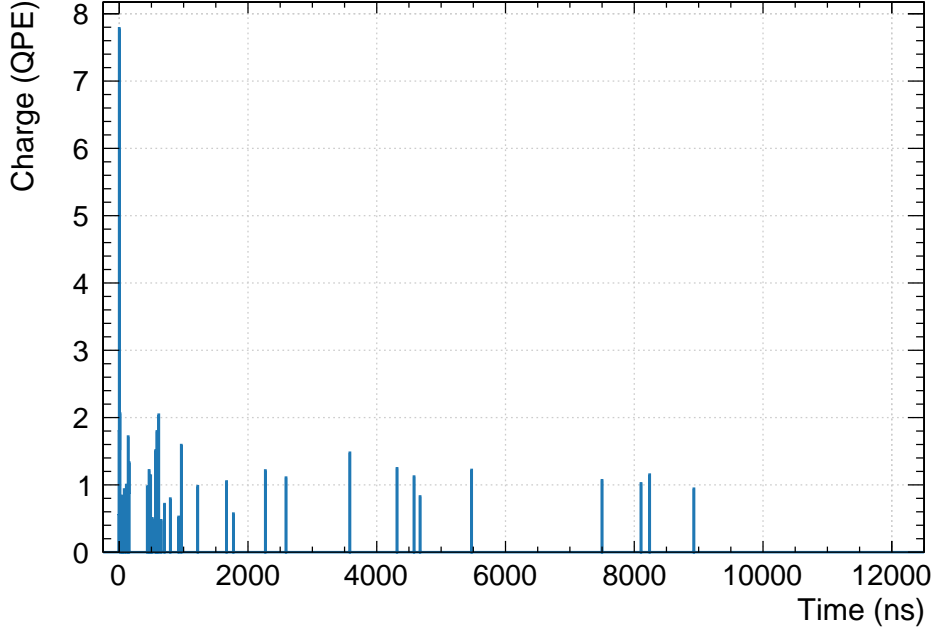
Figure 7: PMT trace for a typical electronic recoil event (QPE = 66.4). This is obtained by adding up the pulses detected by the full PMT array.

The digitizers only digitze the part of the PMT waveforms where a signal threshold of about 10 % of the SPE signal-height is crossed. These parts are referred to as pulses. The raw PMT signal, where a single PE typically produces a pulse with a width of > 50 ns, is converted into delta-peaks with height of the integrated charge of the pulse [32]. The time resolution achieved by the PMTs for standard SPE-pulses is estimated to be < 2 ns. If multiple photons are seen by the same PMT within a short time window, such that their raw PMT traces overlap, the time of the resulting subpeaks in the PMT traces are also saved. For the rest of this work, these subpulses will be used exclusively and simply referred to as pulses.

An approximately linear dependency of the total detected charge $Q$ in an event on the energy of the detected particle is expected. This proportionality varies by particle type as the light yield in liquid argon is particle dependent. The light yield for electronic recoils can be estimated through a fit of the $Q$-spectrum with the theoretical $^{39}$Ar spectrum. The estimate for the light yield used in this work is 7.7±0.2 QPE per keV (or keV$_{\mathrm{ee}}$) for electronic recoils. As an in-situ energy calibration for nuclear recoils is not available, the light yield for nuclear recoils is obtained using the quenching factor measured by the SCENE collaboration. This introduces a non-linearity into the energy calibration, as the quenching factor is energy-dependent.

In addition to the number of photon estimated via charge, a more sophisticated measure, $n_{\mathrm{nsc}}$, is used in this work. This estimate only considers pulses which are unlikely to be afterpulses and is obtained by performing a Bayesian analysis on each pulse as described in detail in appendix B.

## 3.4 Background mitigation

There are a number of sources of events other than WIMPs in the DEAP-3600 experiment. Events produced by some of these sources differ in their characteristics from WIMP-events and can be removed with sophisticated data-cuts. Others could produce a signal indistinguishable from WIMPs and thus have to be suppressed by the detector design.

Like WIMPs, neutrons interact via nuclear recoils and produce a similar argon scintillation time structure. Hence, neutrons present a particularly dangerous background to the experiment and low abundance of neutron sources in all detector components has to be achieved. The hydrogenous inner detector material additionally provides a strong shielding against neutrons coming from outside the detector [35]. Neutrons produced by cosmic muons are suppressed through placement of the detector underground and the outer detector veto system.

Another background are alpha sources which can also produce an event time structure similar to WIMPs. Even though highly radiopure materials are deployed, among others the unpure PMT glass-windows cause an alpha and gamma-rate of multiple Bq. When exciting the liquid argon, both backgrounds produce a signal far above the WIMP energy spectrum, however they still pose a relevant WIMP-background as they can induce neutrons [36]. Also, alpha sources on the acrylic vessel surface or inside the TPB layer could knock the daughter nucleus into the argon which then scatters in a low energy nuclear recoil. Charged particles in the acrylic may produce Cherenkov light. These events will typically cause a short flash in only few PMTs which is an incompatible topology to argon scintillation and can be removed with corresponding data cuts.
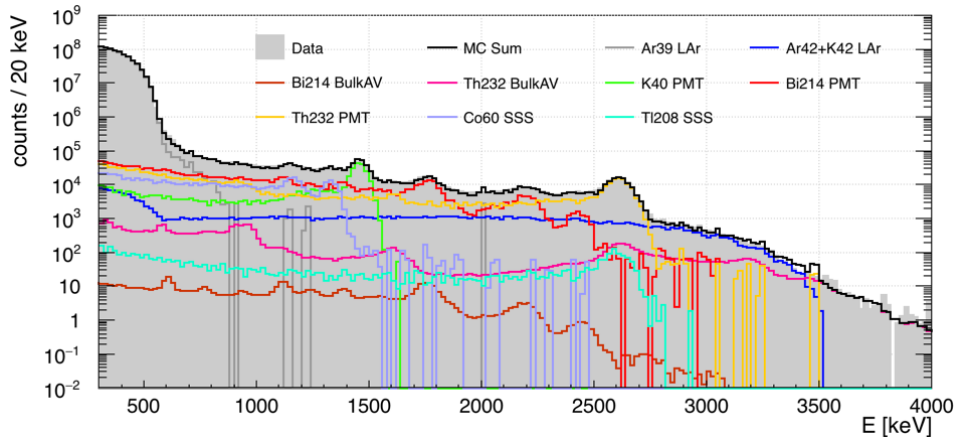


Figure 8: Data and background comparison of DEAP electronic recoil data taken from [37]. Known background components are simulated and scaled to screening measurements or known specific activities of radioactive isotopes in LAr. This is not a fit but an illustration of the electronic recoil background components and the match of previously determined activities of detector components. The energy resolution and pile-up is empirically adjusted to match the data.

The highest background rate comes from the beta-decaying isotope $^{39}$Ar with approximately 1 Bq/kg

of natural argon which dominates the overall event rate. This is illustrated by figure 8 which shows electronic recoil background spectrum that is seen by DEAP. Here, below 500 keV, the $^{39}$Ar activity surpasses all other backgrounds by over 3 orders of magnitude. Beta-radiation interacts in the argon via electronic recoils and hence can be discriminated using PSD. $^{39}$Ar still limits the detector sensitivity at low energies where PSD becomes less powerful. It also could produce a WIMP-like signal when piled up with Cherenkov light. For this, algorithms are implemented that recognize features that are characteristic for pile-up events.

The data selection cuts applied in this work are designed to select argon scintillation events and are listed in appendix A.

# 4    The liquid argon scintillation pulse shapes in DEAP

PSD relies on understanding the difference in PMT traces produces by electronic and nuclear recoils. While these differences are ultimately caused by the different singlet-to-triplet ratios caused by both event types, the PMT traces in a real detector include components that are not due to the decay of argon excimers. In order to understand how large the impact of these detector effects is and at which time windows they occur, the average pulse shape is built by averaging over the PMT traces of a large number of events. Pulse shapes are built over the full PMT array as well as for each for PMT individually to isolate PMT-specific features. In addition to their importance for PSD, these can be used to validate and estimate the afterpulsing rate (see appendix D), to extract an estimate of the dark rate from the pre-trigger window of the pulse shapes, and to fit out the lifetime of the argon triplet lifetime in DEAP-3600 (see appendix C).

## 4.1 The $^{39}$Ar background pulse shape

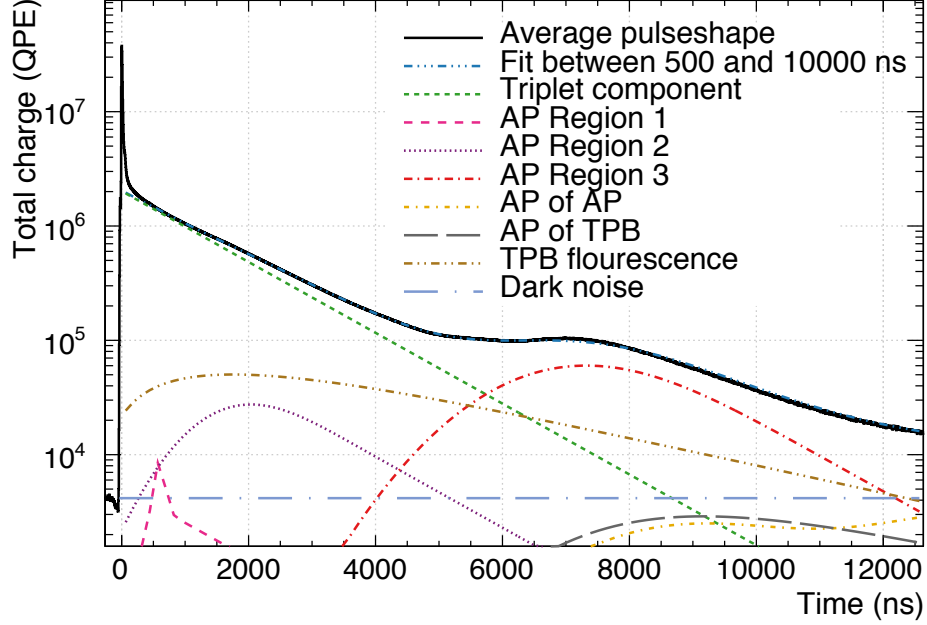### 4.1.1 Charge-based pulse shapes



Figure 9: The average $^{39}$Ar pulse shape built using the pulse-charge over 600491 events. Also shown is a fit function which highlights the different components of the pulse shape after 500 ns: argon triplet scintillation, TPB fluorescence, afterpulsing and dark noise. Afterpulsing is subdivided into different regions where each region represented by a Gaussian convoluted by the argon scintillation response in time. The TPB fluorescence function is the exponential found in [38] convoluted by the argon singlet and triplet component. The fit and its parameters are further discussed in appendix C.

Figure 9 shows the average pulse shape over the full PMT array for a dataset (run) taken five days after the completion of the argon fill and the same pulse shape with a simple fit function highlighting the different components. The fit function and its parameters are discussed in detail in appendix C, where it is also used to extract and monitor the triplet lifetime over a one-year-dataset. The runs used have a total duration of 5.6 h and 600491 events are used in the pulse shape. Data-cuts are applied such that argon scintillation events between 30 keV$_{ee}$ and 80 keV$_{ee}$ are selected. Due to its dominant rate practically all of these events are $^{39}$Ar electronic recoils. The pulse shape peaks sharply at the estimated event time. This is expected because most of the argon singlet excimers decay within a few nanoseconds after formation. The precise shape of this peak is determined by the PMT response functions and optical properties of the detector. From 200 to 4000 ns the pulse shape decreases exponentially as triplet scintillation dominates. At 5000 ns the number of pulses increases again because of afterpulsing and peaks around 6500 ns. The tail of the pulse shape, at 13000 ns or almost 10 triplet lifetimes after the event start is significantly above the dark noise level extracted from the pre-event level. Some of this might be due to a delayed TPB fluorescence component that was investigated in [38,39]. The fit function here

uses the long-lived component of the TPB-fluorescence-model found by E. Segreto et al.

The delayed TPB light emission time structure is hard to extract from the electronic recoil data because here, the delayed light intensity is dominated by the triplet component. However, by comparison of pulse shape-fits that include and exclude the delayed TPB fluorescence component it can be concluded that this component is likely also seen in DEAP with the $\chi^2$ of fits including the Segreto TPB model being reduced by a factor of 3 (without adding any additional free fit parameters).

Another component that can be extracted from the pulse shapes is afterpulsing. While this is difficult in the case of the first two afterpulsing regions as afterpulsing is very subdominant here, it is possible in the case of AP region 3. Here, the mean, width and height of the Gaussian that used to describe the AP are left as free parameters in the fit above. The fit result can then be compared to the time structure that is expected from the afterpulsing calibration. Here, it is found that the mean of the Gaussian is shifted against what is expected from the calibration by 500 ns. The origin of this shift has not been resolved yet.
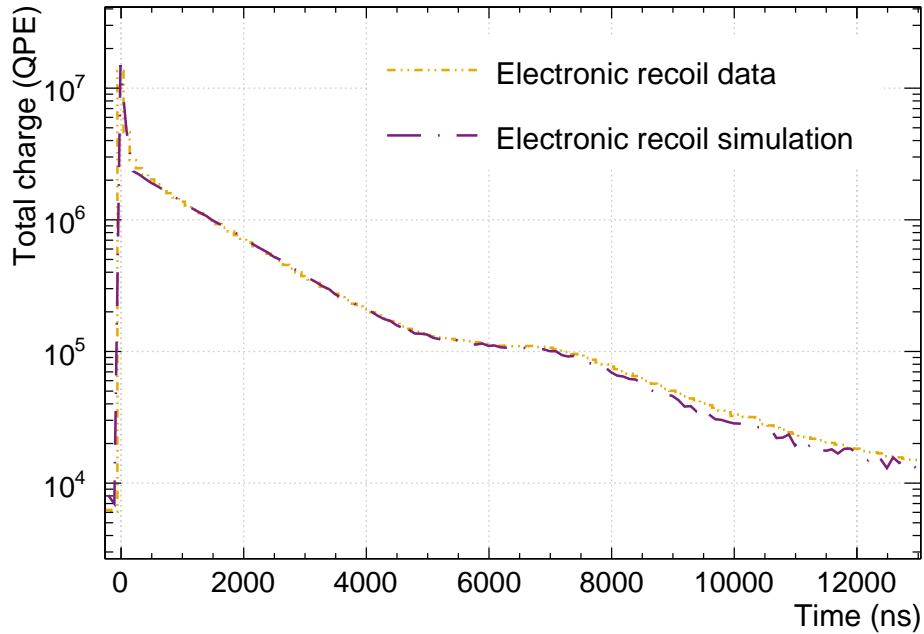


Figure 10: Pulse shapes of electronic recoils from data (580416 events) and Monte Carlo (24282 events). The Monte Carlo is scaled such that the integrals of the two pulse shapes agree.

A way to generate the detector response to any given physical process in the detector is a Monte Carlo simulation (MC). This technique will be used throughout this work, in particular to estimate the signal pulse shape and PSD-distribution. The DEAP-Monte Carlo software uses a modified Geant4-based physical model. The Monte Carlo comprises the full detector geometry and PMT and DAQ response. This includes usage of the afterpulsing calibration data (figure 6) to generate afterpulsing with the measured properties of each PMT. Delayed light from TPB fluorescence is not simulated.

20

The $^{39}$Ar electronic recoil background is a suitable event source to verify the MC given its high abundance of events. Figure 10 shows the pulse shapes obtained from data and Monte Carlo. Here, the same cuts are applied to both datasets. Up to 6000 ns there is very good agreement between the two pulse shapes. Above 6000 ns, the data-pulse shape is approximately 10 % higher than the MC-pulse shape. A plausible explanation for this could be the missing TPB fluorescence simulation, which only becomes significant late in the pulse shape (see figure 9).

### 4.1.2 Afterpulsing-corrected pulse shapes

In addition to charge, the photon count $n_{nsc}$ will be used as an estimate for the number of photons in the PMT traces. Because afterpulsing and scintillation follow very different distributions in time, the $n_{nsc}$-pulse shape is expected to differ from the charge-weighted pulse shape.
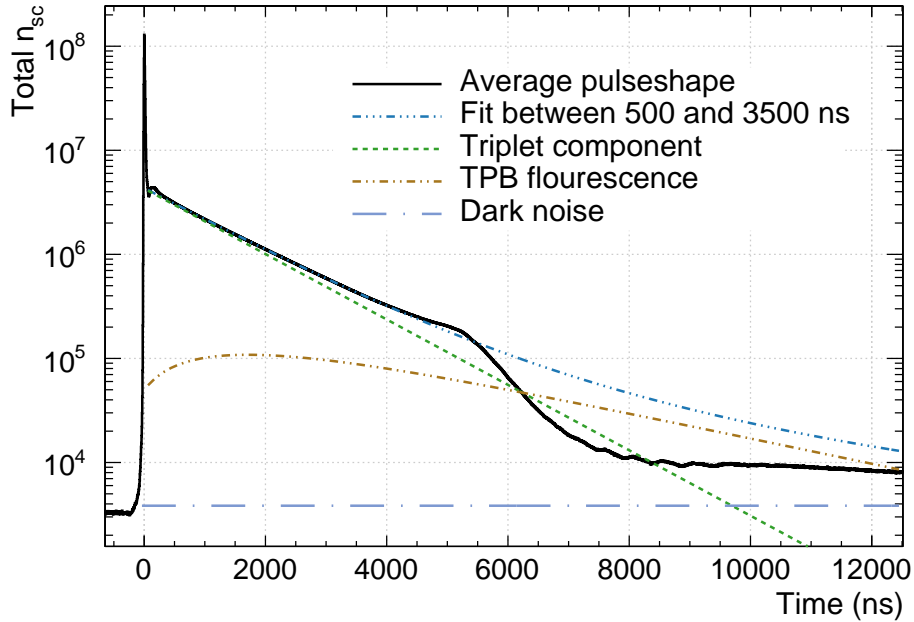


Figure 11: Pulse shape of electronic recoil events using the photon count $n_{nsc}$.

Figure 11 shows the pulse shape from the same run using $n_{nsc}$ instead of charge with the same fit function without the afterpulsing components. The pulse shape behaves similar to the charge-weighted pulse shapes until 5000 ns. From 5000 to 6000 ns the pulse shape declines sharply and stays then relatively flat until end of the pulse shape. Beyond 5000 ns the behaviour therefore differs severely from the scintillation model. The estimated loss of the scintillation yield, i.e. difference between the integral of the fit function and the data from 0 to 13000 ns is 3%. A possible explanation for this feature could be the estimator that is used to calculate $n_{nsc}$: $n_{nsc}$ is set to the value that maximizes its posterior (also known as a maximum a posteriori (MAP) estimator). At 6000 ns afterpulsing is on average more likely than scintillation as indicated by the afterpulsing peak in the charge-weighted pulse shapes. Because

$n_{\mathrm{nsc}}$ is set to its most likely value, the scintillation contribution will be ignored in many cases where it still makes up a significant (but subdominant) share of the total pulse shape. An alternative explanation would be that the simplifications made by the model cause this bias.
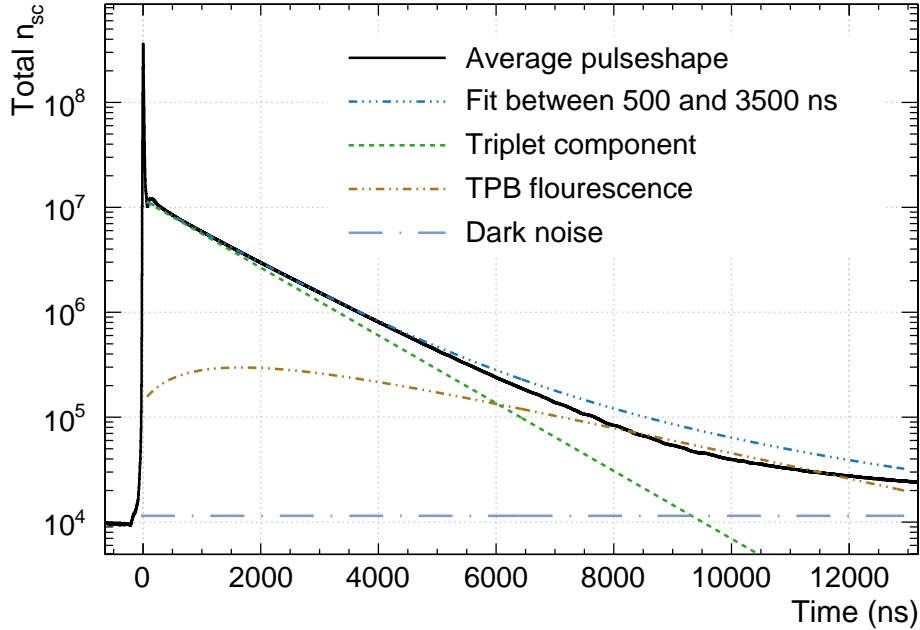


Figure 12: Pulse shape of electronic recoil events using the photon count $n_{\mathrm{nsc}}$ estimated using an MMSE estimator.

To test the first hypothesis, an $n_{\mathrm{nsc}}$-variation is implemented that uses the same physical model, but estimates $n_{\mathrm{nsc}}$ as its mean over the posterior (minimum-mean-squared-error or MMSE estimator). The MMSE-pulse shape (figure 12) is much more compatible with a scintillation pulse shape and does not show a sharp drop as in figure 11. This suggests that this feature is indeed a threshold effect produced by the estimator and indicates that the model describes the data appropriately. It should be noted that the MMSE-pulse shape does not match the fit function perfectly either. In particular, the TPB fluorescence component appears to be lower in data than in the parameters found in Segreto's paper [38]. It is unclear whether that is due to a bias in the estimator or whether the TPB fluorescence trace indeed differs from the values found by Segreto.

The $n_{\mathrm{nsc}}$ photon count using the MMSE estimator will later be used as a photon estimate for PSD and requires a separate energy calibration. This has not been done yet by fits of for example the $^{39}$Ar-spectrum. The relative LYs between charge and $n_{\mathrm{nsc}}$ can still be found by finding the average charge that correspond to a $n_{\mathrm{nsc}}$-value. The LY in the energy region of interest found this way is $7.0\mathrm{NSC}\pm0.3n_{\mathrm{sc}}/\mathrm{keV}$ for the MMSE estimate, where NSC is the unit of $n_{\mathrm{nsc}}$.

For a more detailed comparison of the MAP and MMSE estimators in the context of the PE counting

problem, see appendix B.4.

## 4.2 The nuclear recoil signal pulse shape

For PSD, the difference between the nuclear and electronic recoil pulse shape is critical. The nuclear recoil pulse shape can not be built easily from data as nuclear recoils in the liquid argon are suppressed by detector design. Nuclear recoil datasets can still be produced in two ways: placement of a neutron source close to the detector and Monte Carlo simulations. Additionally, pulse shapes can be built using a model of the scintillation and PMT-response time structure.

### 4.2.1 Charge-based pulse shapes

To see what a WIMP interaction in the detector could look like, a neutron source calibration is performed. Neutrons, like WIMPs, interact via nuclear recoils.

Neutrons can be produced by a composite source consisting of an alpha emitter and a light element. Typically, the alpha-emitter and light element used are Americium ($^{241}$Am) and Beryllium ($^{9}$Be), respectively, forming an AmBe source [40]:

$$^{241}\text{Am} \rightarrow {}^{237}\text{Np} + {}^{4}\text{He} \tag{15}$$

$$^{9}\text{Be} + {}^{4}\text{He} \rightarrow {}^{12}\text{C} + \text{n}. \tag{16}$$

Here the C-atom can be produced in an excited state which quickly decays emitting a 4.4 MeV gamma-ray. The AmBe-neutron spectrum has a non-trivial multimodal form that extends down to low energies.
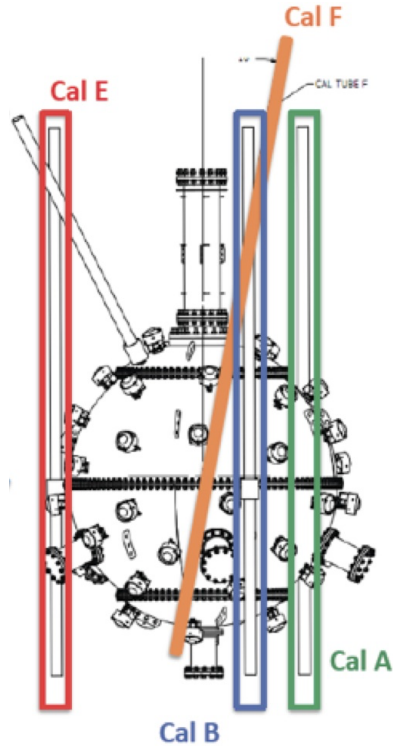
Figure 13: The calibration tubes for radiative sources and the outer steel shell of the DEAP-3600 detector are shown taken from [41]. The CAL F tube is wrapped around the detector. The neutron source data discussed in this section was taken with the AmBe source in CAL tube E at the detector equator over 2.7 days.

DEAP uses an AmBe source with an activity of 74 MBq. The closest the AmBe source can be placed to the liquid argon is in tubes around the outer steel shell (see figure 13). Neutrons have to pass the steel shell and the acrylic shielding before entering the argon. Therefore, only few detector events caused by the AmBe source interact in the detector like WIMPs do, i.e. in a single scatter nuclear recoil in the liquid argon. For example, in many events, the emitted gamma or neutron may scatter in the acrylic before entering the argon, producing a primary Cherenkov signal. Also, neutrons may scatter multiple times in the argon unlike WIMPs. To understand what the dominant event populations caused by the source are and to extract the single scatter nuclear recoil events, the data is compared to simulations of these populations.
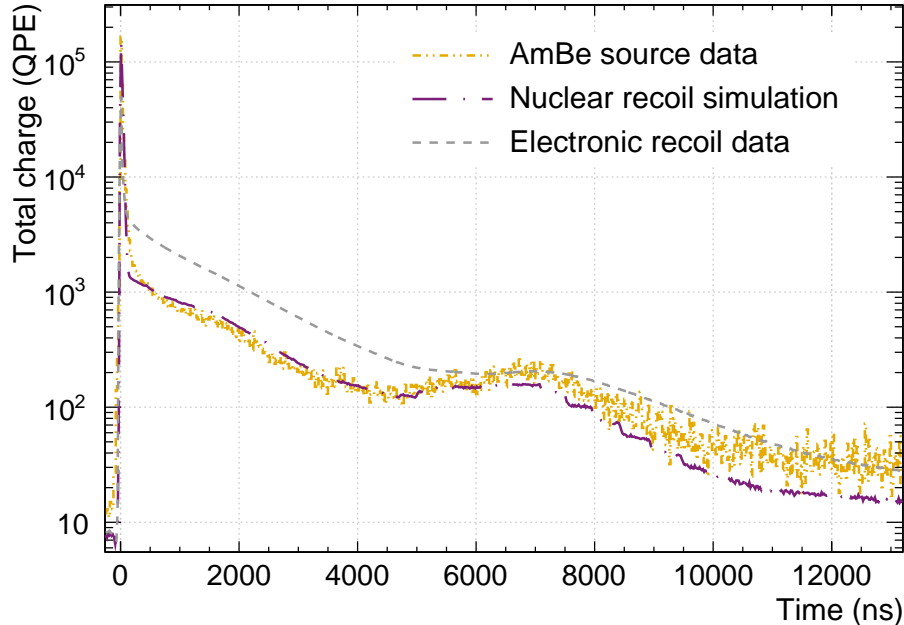
Figure 14: Pulse shapes of the AmBe calibration data, a nuclear recoil simulation and electronic recoil data using the are shown. Events with energies between 15 keV$_{ee}$ and 60 keV$_{ee}$ and $F_{prompt} > 0.6$ for AmBe data are selected. The simulated (4684 events) and electronic recoil pulse shape (600491 events) are scaled down to match the integral of the AmBe-pulse shape (1622 events).

Another way to produce a nuclear recoil pulse shape is via a Monte Carlo simulation (Monte Carlo or MC) of $^{40}$Ar nuclei ($m = 37$ GeV) in the liquid argon. Like WIMPs, the nuclei scatter in the argon in nuclear recoils. The singlet-to-triplet ratios of argon dimers produced by the nuclear recoils are set to the values measured by the SCENE collaboration [23]. Figure 14 shows the pulse shape of simulated recoils uniformly distributed throughout the argon with a flat momentum distribution from 20 to 200 keV. This is compared to the AmBe-calibration data and an electronic recoil pulse shape. Because the AmBe calibration data is still dominated by $^{39}$Ar events, the nuclear recoil events are selected using a cut on the prompt fraction of charge, $F_{prompt}$. This parameter is also used for pulse shape discrimination and is discussed in detail in section 5.1.

As expected, the singlet peak is higher for the nuclear recoil signal. The triplet component in the nuclear recoil event traces is suppressed compared to electronic recoils such that two afterpulsing region at approximately 500 ns and 2000 ns can be seen. As the afterpulsing in electronic recoil events is dominated by afterpulsing of the narrow and early singlet peak, the afterpulsing peak in the nuclear recoil pulse shape at 6000 ns is narrower and centered around an earlier time relative to the afterpulsing in the electronic recoil pulse shape. The AmBe and Monte Carlo pulse shape do not match at several times in the pulse shapes. Firstly, the AmBe singlet peak is broader than the singlet peak of electronic recoil data and simulated nuclear recoils. This might be due to events where neutrons scatter multiple times in the detector. As noted above, the position of the afterpulsing region around 6500 ns is shifted

approximately 500 ns. This can also be observed in figure 14 and is expected because the simulation relies on the calibration to generate afterpulses. Also, the tail of the pulse shape is lower in simulation than for the AmBe data. This might be explainable by the missing TPB fluorescence simulation in Monte Carlo.

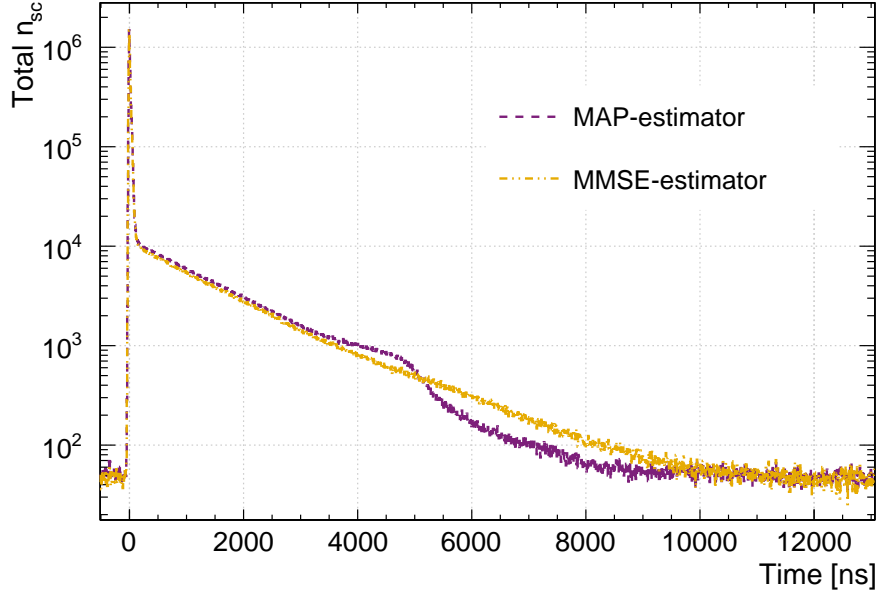### 4.2.2 Afterpulsing-corrected pulse shapes



Figure 15: $n_{\mathrm{nsc}}$ - pulse shapes of simulated nuclear recoils.

For electronic recoil data a time-dependent bias was found under the MAP-PE counting scheme. This bias is also present in the nuclear recoil simulation as shown figure 15. Here, the pulse shape under the MAP and MMSE estimator are compared. The threshold effect disappears as $n_{\mathrm{nsc}}$ is estimated over the mean of the posterior, which confirms that the bias is caused by the default estimator.

## 4.3 Mathematical pulse shape model

As shown with the fit in figure 9, the pulse shape can be modelled by a mathematical model. In this section, this function is extended to describe the full pulse shape including the prompt peak of nuclear and electronic recoil events. This model will be used later to build timing PDFs and evaluate a likelihood-based PSD parameter.

The only difference in the electronic and nuclear recoil PDFs should be the underlying singlet-to-triplet ratio. Therefore, it is convenient to build PDFs for the singlet and triplet component separately and to mix them with distinct ratios to obtain the electronic and nuclear recoil PDF. Here, it is assumed

that the shape of these PDF does not depend on e.g. the event energy or position, such that the PDFs can be used to describe all argon scintillation events. Because afterpulsing and TPB fluorescence scale with the amount of argon scintillation light, the time responses of these components can be included by convoluting their response with singlet and triplet exponentials. The models used here are the same that are used for the pulse shape fit described in appendix C. The remaining component that does not scale with the energy of an event is dark noise and should therefore be added separately.
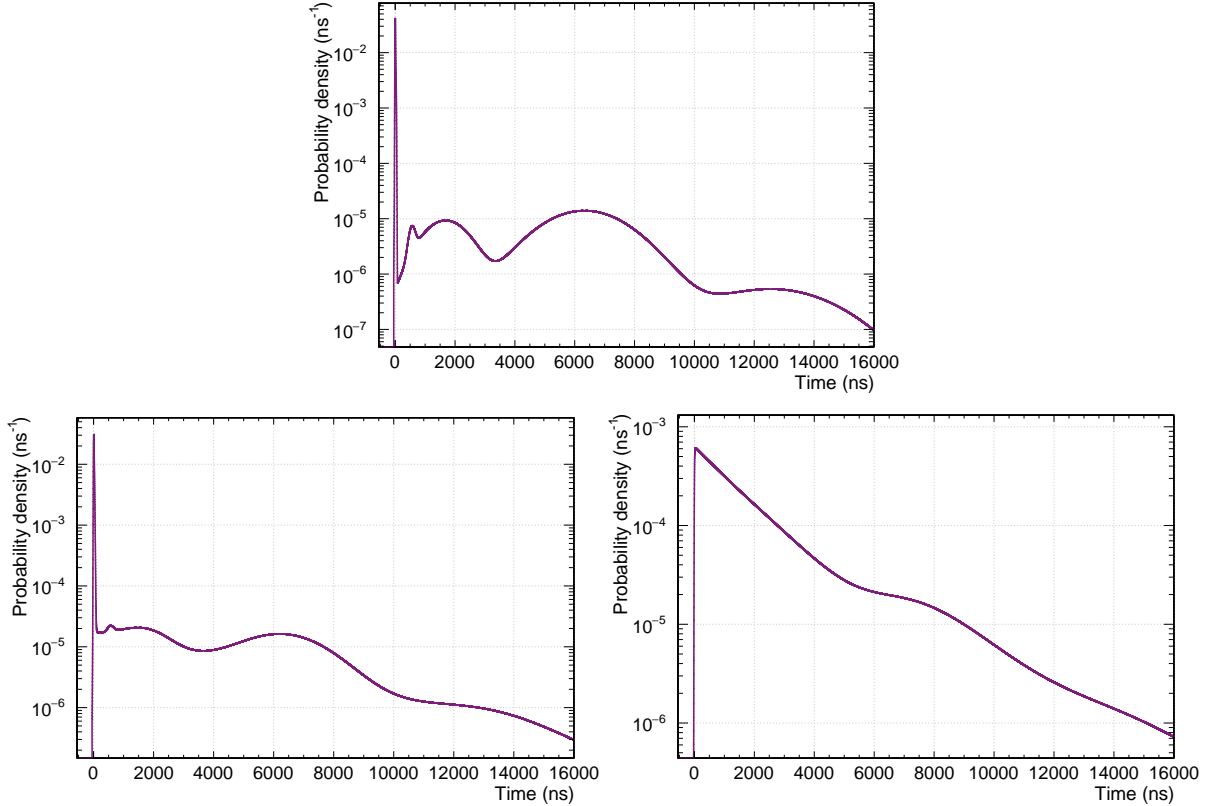


Figure 16: The top figure shows the average PMT response to a delta-peak. The peak of the response function is built from an exponential for the rise of the peak, a Gaussian centered around zero and a delayed Gaussian for double pulsing. The parameters of these functions are chosen such that the final PDF matches the peak of the pulse shape of electronic recoils in data. The afterpulsing response is modelled by three Gaussians whose parameters are set to the values obtained by the fit shown in figure 9. Dark noise is not included here. Also shown are the singlet (bottom left) and triplet (bottom right) PDFs, obtained from convoluting the PMT response with the argon and TPB responses. Here, singlet and triplet lifetimes of 6 ns and 1390 ns are assumed.

To obtain an electronic and nuclear recoil PDF, the model singlet and triplet component are mixed with the singlet-to-triplet ratios measured by the SCENE collaboration for nuclear recoils and measured by the CLEAN collaboration for electronic recoils for the estimated event energy. Both are shown as a function of energy in figure 18. Also, a flat dark noise level is added such that the expected dark charge $Q$ is equal to the measured expected dark charge across the PMT array. This means that the dark noise

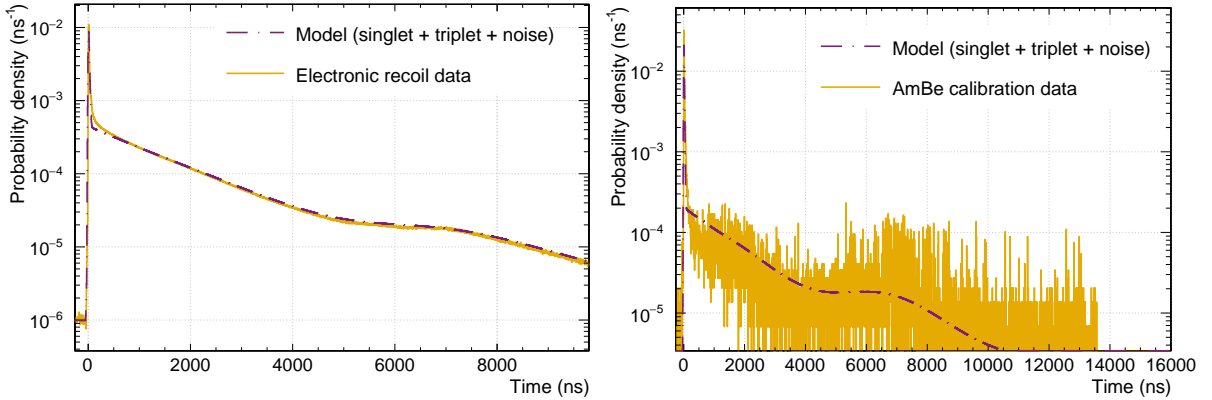fraction is smaller for high energy events than for low energy events.



Figure 17: The combined model scintillation PDFs for 15.36 keV$_{ee}$ electronic recoils (left) and nuclear recoils (right) are shown. The PDFs are compared to pulse shapes built from electronic recoils and AmBe data between 100 QPE (13.4 keV$_{ee}$) and 120 QPE (16.0 keV$_{ee}$).

An example for a pair of model-PDFs is shown in figure 17. This is obtained by mixing the singlet and triplet model PDFs (figure 16) with the measured singlet fractions at 15.36 keV$_{ee}$ (0.29 for electronic recoils, 0.69 for nuclear recoils). The dark noise level is estimated from the early window of the pulse shape. To verify the model, this is compared to pulse shapes from data. The electronic recoil PDF agrees very well with the pulse shape. This implies that both the models used for the singlet and triplet time structure as well as the singlet-to-triplet ratio measured by the CLEAN collaboration describe the data well. For nuclear recoils, the triplet component in data appears to suppressed when compared to the model. This can be explained by the $F_{prompt}$-cut that are used, which biases the event selection towards events with low late-light-intensity. The low statistics of the nuclear recoil data in the narrow energy range used here prohibits to test the agreement at later times.

# 5 Pulse shape discrimination

As discussed in section 1.3, even a well understood background with a background model significantly affects the sensitivity of a direct detection experiment. Therefore, in order to set a competitive limit on the WIMP-nuclear recoil cross section, DEAP-3600 has to discriminate its background of more than $10^8$ $^{39}$Ar events per year and keV$_{ee}$ (see figure 8) in its energy region of interest from nuclear recoils. This is possible by excluding events from the WIMP-search that are likely to emerge from the electronic recoil PDF. For this, parameters have to be found that capture the similarity of an event trace to the PDFs shown in the prior section. In addition to background suppression, PSD also allows for isolation of different detector backgrounds for calibration purposes and detector studies.
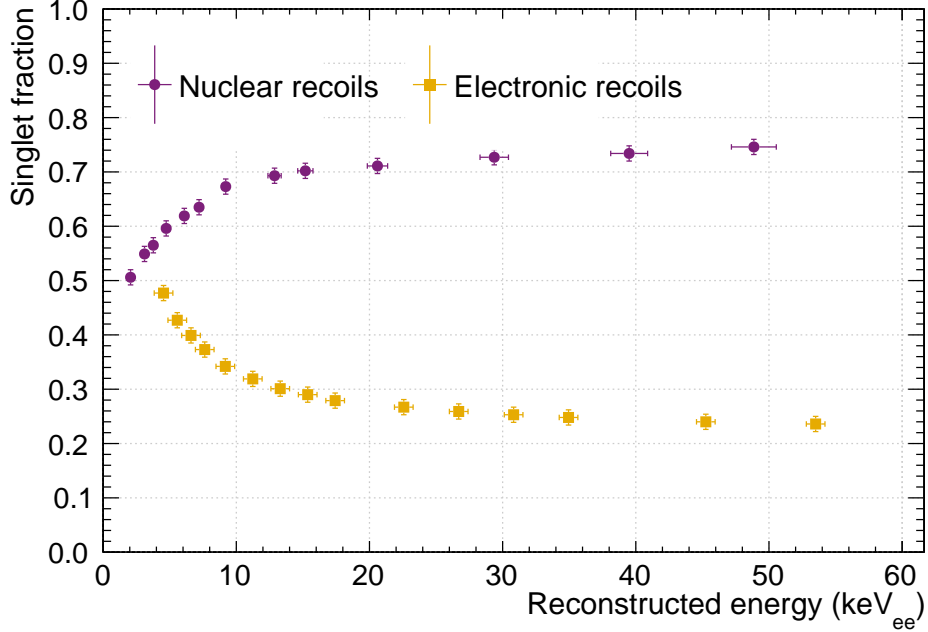
Figure 18: Singlet fractions for electronic and nuclear recoils measured by the CLEAN [23] and SCENE [24] collaboration, respectively. The nuclear recoil energies are converted to $keV_{ee}$ using the quenching factor measured by SCENE.

PSD is ultimately enabled by the different singlet-to-triplet ratios for electronic and nuclear recoils which are found to be energy dependent. The singlet fraction for both interaction types are shown in figure 18. Below 5 $keV_{ee}$, the singlet and triplet fractions of both interactions are approximately equal and diverge slowly at higher energies. Therefore, PSD is only viable above an energy threshold and only becomes more powerful at higher energies. With an anticipated energy threshold of 18 $keV_{ee}$, in DEAP, the limiting factor for PSD at low energies is the low statistics of photons in the events. This is because for an electronic recoil at low energies it is more likely that a large fraction of triplet excimers decay at a time scale that is typical for singlet excimers and the event mimics a nuclear recoil this way. PSD therefore becomes significantly more powerful at higher energies, despite the singlet-to-triplet ratio staying constant here.

The energy threshold in DEAP-3600 for the WIMP-search is directly set by the energy at which the $10^8$ $^{39}$Ar per $keV_{ee}$ and year can be reduced to our design goal of 0.2 events in the WIMP search region. This lower bound of the WIMP search box is of particular importance to the sensitivity of the experiment because of the exponential decrease of the WIMP nuclear recoil spectrum. Using a PSD parameter that achieves strongest separation of electronic and nuclear recoils can therefore notably increase this sensitivity. In the following section different PSD parameters are introduced and evaluated with regard to their viability for the DEAP-3600 dark matter search analysis.

## 5.1 Prompt-window-based discrimination

A simple discrimination parameter $F_{\text{prompt}}$ is defined as the fraction of charge in the prompt time window $[t_{\text{start}}, t_{\text{prompt}}]$ of an event. Because the prompt peak is dominated by singlet photons, this discriminator can be interpreted as a simple estimate for the singlet fraction in an event and is therefore on average higher for nuclear recoils than for electronic recoils.

$$F_{\text{prompt}} = \sum_i n_i [t_{\text{start}} < t_i < t_{\text{prompt}}]/n_{\text{total}} \qquad (17)$$

Here, $n_i$ refers to the estimated number of photons in the subpulse at time $t_i$. This discriminator introduces two free parameters: the start of the integration windows $t_{\text{start}}$, the end of the prompt integral $t_{\text{prompt}}$ and the end of the total integration window $t_{\text{late}}$. These parameters have been found to be optimal at $t_{\text{start}} = -28$ ns and $t_{\text{prompt}} = 60$ ns [42]. For $n_{\text{total}}$ it is summed over photons in [-28 ns, 10 us].

Prompt-window-based discriminators are well established for PSD in liquid argon scintillation and are used by dark matter experiments, most notably DEAP and DarkSide in their most recent publications [11, 43]. Advantages of prompt-window-based discrimination include that they are computationally inexpensive. Also, due to their simplicity, analytical and physically-motivated models can be developed to describe their distributions [44]. For the rest of this work $F_{\text{prompt}}$ refers to the parameter using charge, whereas $F_{\text{prompt}}^{\text{sc}}$ refers to the prompt-window-based discriminator using $n_{\text{nsc}}$.

## 5.2 Likelihood-based discrimination

A disadvantage of $F_{\text{prompt}}$ is that it bins the highly resolved timing information of an event into prompt and late light. A PSD-parameter that makes use of the full information contained in the event pulse shape should in theory achieve superior discrimination and therefore improve the sensitivity of the experiment. This can be implemented by weighting pulses in a particle identification parameter $S$ with a function $w(t_i)$ that depends on the position of pulses in time, as described in [45] by E. Gatti and F. de Martini:

$$S_{\text{Gatti}} = \sum_i w(t_i) n_i. \qquad (18)$$

Here, it was shown that the relative variance of the separation between $S_{\text{Gatti}}$ produced by electronic and nuclear recoils is minimized, if

$$w^{S_{\text{Gatti}}}(t_i) = \frac{p(t)_{\text{nr}} - p(t)_{\text{er}}}{p(t)_{\text{nr}} + p(t)_{\text{er}}}, \qquad (19)$$

$p(t)_{\text{er}}$ and $p(t)_{\text{nr}}$ are the PDFs of electronic and nuclear recoils in time at the estimated event energy. Intuitively, its modulus is a measure for how much information a photon at time $t$ contains with regard to the event being an electronic or nuclear recoil. For example, if both PDFs are equal at some time, the weight function $w(t)$ becomes zero and photons arriving at this time would not affect $S_{\text{Gatti}}$. The

sign of $w(t)$ indicates whether photons arriving at $t$ are more indicative of the event being an electronic (negative sign) or nuclear recoil (positive sign). For the rest of this work, $w(t)$ will be referred to as the photon weight, or simply weight.

Another PSD-parameter that takes into account the precise PMT event-trace is the likelihood ratio between an event being an electronic and nuclear recoil. According to the Neyman-Pearson lemma, the likelihood ratio $\Lambda$, i.e. the ratios of likelihoods of an observation under two different hypothesis $\theta_0, \theta_1$, is the most powerful test of $\theta_0$ against $\theta_1$ at a given significance level [46]. Indeed, it was shown in [47] that in a simulation of electronic and nuclear recoils in the CLEAN-detector, a likelihood-based PSD-discriminator can perform better than a prompt-window-based discriminator. Here, the likelihood ratio between the electronic and nuclear recoil-hypothesis was defined by

$$\Lambda(\{t_1..t_n\}) = \frac{\mathcal{L}(\theta_{\mathrm{nr}}|\{t_1..t_n\})}{\mathcal{L}(\theta_{\mathrm{er}}|\{t_1..t_n\})}, \tag{20}$$

where $\theta_{\mathrm{nr}}$ and $\theta_{\mathrm{er}}$ denote the hypothesis that the event is produced by a nuclear or electronic recoil, respectively and $\{t_1..t_n\}$ are the photon arrival times. If the photons are drawn independently from the PDFs, as they are for dark noise and argon scintillation, the total event likelihood can be written as the product of the photon arrival likelihoods:

$$\mathcal{L}(\theta|\{t_1..t_n\}) = \mathcal{L}(t_1|\theta)..\mathcal{L}(t_n|\theta). \tag{21}$$

For computational reasons it is advantageous to use the log-likelihood ratio. With $\mathcal{L}(\theta_{\mathrm{nr}}|t_i) = p(t)_{\mathrm{nr}}$ and $\mathcal{L}(\theta_{\mathrm{er}}|t_i) = p(t)_{\mathrm{er}}$ above, $\log\Lambda$ can be rewritten as a function of the log ratio of the two PDFs $w^{L_{\mathrm{recoil}}}(t_i) = \log\frac{p(t)_{\mathrm{nr}}}{p(t)_{\mathrm{er}}}$. Also, whereas for integer estimates for the number of photons, like $n_{\mathrm{sc}}$, $\Lambda$ can be evaluated directly, its definition can also be extended for continuous estimates like $Q$ by weighting each pulse with its photon-estimate. Note that under this extension, $\mathcal{L}$ is not strictly a likelihood, as the likelihood to see a non-integer number of photons is zero. With this, we get

$$\log\Lambda\left(\{t_1..t_n\},\{n_1..n_n\}\right) = \sum_i n_i w^{L_{\mathrm{recoil}}}(t_i). \tag{22}$$

From equation 22 it can be seen that $w^{L_{\mathrm{recoil}}}(t)$ takes the place of a weighting function, as in the definition of the Gatti parameter. It can be seen that both $w^{S_{\mathrm{Gatti}}}(t)$ and $w^{L_{\mathrm{recoil}}}(t)$ can be written in terms of the ratio of both PDFs $x = \frac{p(t)_{\mathrm{nr}}}{p(t)_{\mathrm{er}}}$. Expanding around $x = 1$, where both PDFs are equal yields

$$\sum_i w^{L_{\mathrm{recoil}}}(t_i) = \log x = (x-1) - \frac{1}{2}(x-1)^2 + \frac{1}{4}(x-1)^3 + \mathcal{O}(x-1)^4 \tag{23}$$

and

$$\sum_i w^{S_{\mathrm{Gatti}}}(t_i) = \frac{x-1}{x+1} \propto (x-1) - \frac{1}{2}(x-1)^2 + \frac{1}{3}(x-1)^3 + \mathcal{O}(x-1)^4. \tag{24}$$

Therefore, the weights of photons under $L_{\text{recoil}}$ and $S_{\text{Gatti}}$ coincide up to order $\mathcal{O}(x-1)^3$. Indeed, it is shown in appendix E that the weighting functions of $L_{\text{recoil}}$ and $S_{\text{Gatti}}$ coincide very closely. Therefore only $L_{\text{recoil}}$ is discussed in the main part of this work.

It has several advantages to not use $\Lambda$ directly as a PSD parameter, but to use the following rescaling:

$$L_{\text{recoil}} = \frac{1}{2}\left(1 + \frac{\log \Lambda\left(\{t_1..t_n\}, \{n_1..n_n\}\right)}{n_{\text{total}}}\right) \tag{25}$$

$$= \frac{1}{2}\left(1 + \frac{\sum_i n_i w(t_i)^{L_{\text{recoil}}}}{n_{\text{total}}}\right). \tag{26}$$

Here, normalising by the total number of photons ensures that scaling an event $n_i \to a n_i$ does only affect $L_{\text{recoil}}$ through a potential dependence of the PDFs on the event energy. Because the singlet-to-triplet ratios produced by electronic recoils stay flat above 20 keV$_{\text{ee}}$, so should their PDFs which should cause $L_{\text{recoil}}$ to be distributed within constant bands for both interaction types. Another advantage of the definition in equation 26 is that here, $F_{\text{prompt}}$ can be expressed in terms of $L_{\text{recoil}}$ if weighting function $w^{F_{\text{prompt}}}(t)$ is assumed

$$w^{F_{\text{prompt}}}(t) = \begin{cases} 1, & \text{if } t_{\text{start}} < t_i < t_{\text{prompt}} \\ -1, & \text{if } t_{\text{prompt}} < t_i < t_{\text{late}} \\ 0, & \text{otherwise,} \end{cases} \tag{27}$$

because then

$$L_{\text{recoil}} = \frac{1}{2}(1 + \frac{\sum_i n_i w^{F_{\text{prompt}}}(t)}{n_{\text{total}}}) \tag{28}$$

$$= \frac{1}{2}\frac{n_{\text{total}} + \sum_i n_i w^{F_{\text{prompt}}}(t_i)}{n_{\text{total}}} \tag{29}$$

$$= \frac{1}{2}\frac{\sum_i n_i[t_{\text{start}} < t_i < t_{\text{late}}] + \sum_i n_i[t_{\text{start}} < t_i < t_{\text{prompt}}] - \sum_i n_i[t_{\text{prompt}} < t_i < t_{\text{late}}]}{n_{\text{total}}} \tag{30}$$

$$= \frac{1}{2}\frac{2\sum_i n_i[t_{\text{start}} < t_i < t_{\text{prompt}}]}{n_{\text{total}}} \tag{31}$$

$$= F_{\text{prompt}}. \tag{32}$$

Therefore, the weights that are assigned to photons under a prompt-window-based parameters can be directly compared to the weights used by $L_{\text{recoil}}$.

While $L_{\text{recoil}}$ for a general $w(t)$ can take values between $+\infty$ and $-\infty$ it is later found that practically all liquid argon scintillation events under $w^{L_{\text{recoil}}}(t)$ take values in $[-n_{\text{total}}, n_{\text{total}}]$. Therefore, an additional advantage of the rescaling above is that it projects $L_{\text{recoil}}$ from $[-n_{\text{total}}, n_{\text{total}}]$ into [0,1]. This allows to fit the $L_{\text{recoil}}$-distributions with a gamma-function, which is only defined for positive values, as it will

be done later in this work. For the rest of this work $L_{\mathrm{recoil}}$ is referring to the parameter using charge, whereas $L_{\mathrm{recoil}}^{\mathrm{sc}}$ refers to the likelihood-based discriminator using $n_{\mathrm{nsc}}$.

## 5.3   Evaluation of the photon weight

The construction of a continuous $w(t)$ requires a pair of electronic and nuclear recoil PDFs. These PDFs can be built from a complete detector Monte Carlo, from data and from an effective model. Because PDFs will show some method-dependent features, $w(t)$ should only be formed by PDFs that were built by the same method. As it will be discussed in section 5.4.2, extraction of a clean set of WIMP-like events from the AmBe calibration data has not been achieved to-date. Therefore only log-ratios built from Monte Carlo and a simple model are shown in the section below and used in $L_{\mathrm{recoil}}$.

Also, as it was shown above, the different photon estimators ($Q$, $n_{\mathrm{nsc}}$) differ in their pulse shapes. Therefore, separate PDFs have to be built depending on the photon estimator used.

### 5.3.1   The photon weight under Model PDFs

Because of energy dependency of the singlet and triplet fractions of electronic recoils, the PDFs used should depend on the estimated event energy. Therefore, both PDFs are built by mixing the singlet and triplet component with weights that are looked up from a table of the SCENE measurement for nuclear recoils and CLEAN measurement for electronic recoils as it was shown in section 4.3.
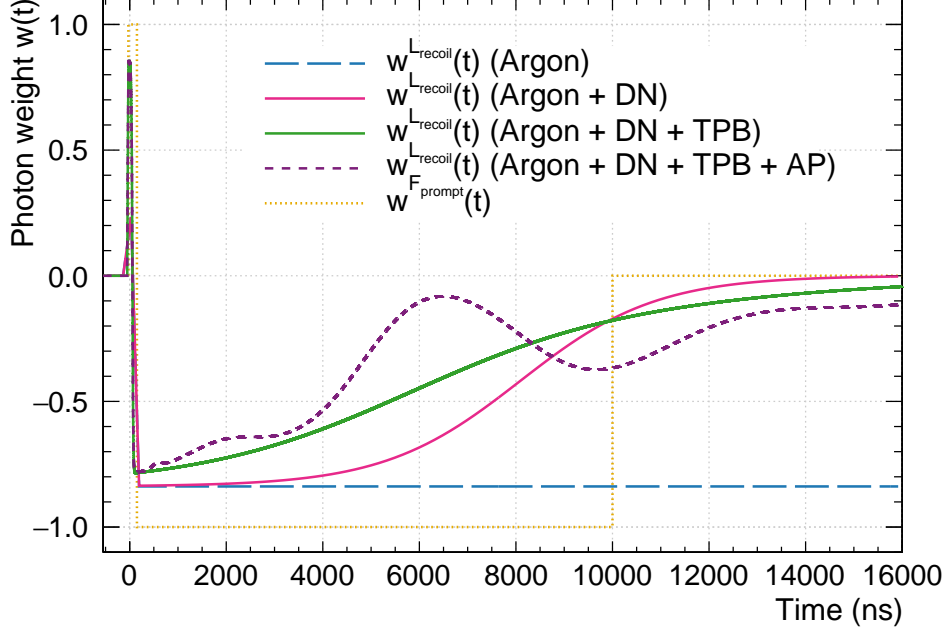
Figure 19: Photon weight-functions for models taking into account different components of the detector response at 15.36 keV$_{\text{ee}}$ are shown. This includes argon scintillation (Argon), dark noise (DN), TPB fluorescence (TPB) and afterpulsing (AP). This is compared to the log-likelihood that is assumed by $F_{\text{prompt}}$. The weight function can be interpreted as follows: pulses time where $w(t) > 0$ or $w(t) < 0$ are more likely to be detected for nuclear recoil or electronic recoil events, respectively. Pulses that are detected at a time where $w(t) = 0$ are equally likely to be seen in nuclear and electronic recoils.

The log-ratio computed using the resulting PDFs is shown in figure 19. Here, different models for the detector response are assumed, such that the impact of the different components can be seen. In every case, the log-ratio is sharply peaked at $t = 0$, where most of the singlet light is detected. For a timing model only consisting of exponentials for the singlet and triplet component, the likelihood function drops sharply after the singlet peak and stays constant afterwards. This can be explained by the large differences in the respective lifetimes: at later times, the singlet component becomes negligible and the log-ratio can be approximated by the log-ratio of triplet fractions for electronic and nuclear recoils. It should be noted that this shape is similar to the step-function that is used as weight for $F_{\text{prompt}}$. Therefore, in an detector with a delta-like response function and no noise, a prompt-window-based discriminator and a likelihood-based discriminator should almost identical results, given that they use pulses in the time windows.

For a model that additionally takes TPB fluorescence and dark noise into account, the log-likelihood ratio converges towards zero at later times. This is the expected behaviour, as the signal-to-noise ratio becomes worse here. Also, by including TPB fluorescence, late light loses some of its information content. Including afterpulsing in the model adds bumps to the likelihood-ratio at the times of high afterpulsing probability (compare with PMT response in figure 16). This makes sense, because both singlet and triplet light cause afterpulsing. This effect is so large that for a brief time around 6500 ns pulses do not carry any information with regard to the nature of the event. Afterwards, the photon weight drops

again as the afterpulsing of the triplet component is delayed relative to the afterpulsing of the singlet component, such that the signal-to-noise ratio becomes better than without afterpulsing.
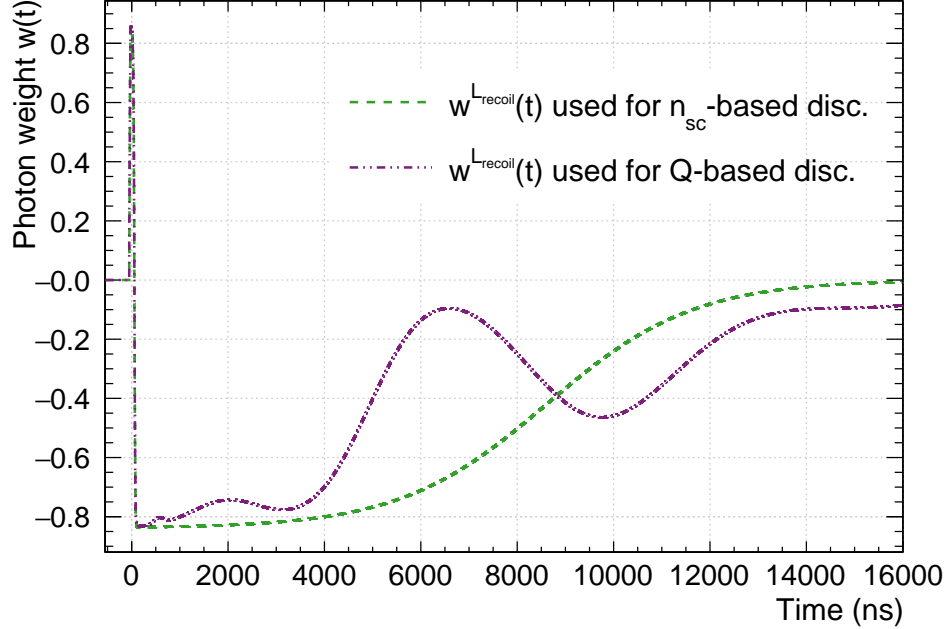


Figure 20: Photon weight-functions that are used for the PSD parameters evaluated in the following section at 15.36 keV$_{ee}$ are shown. For charge ($Q$)-based discrimination the model PDFs include argon scintillation, dark noise and afterpulsing. For the $n_{nsc}$ photon estimators, only argon scintillation and dark noise are considered.

The $w^{L_{recoil}}(t)$ that will be used for PSD going forward for charge and $n_{nsc}$-based discrimination is shown in figure 20. Because the PSD analysis will also be applied Monte Carlo simulated data, where TPB fluorescence is not implemented, this component is not included in the PDFs. This can also be motivated because the time structure of TPB fluorescence has large uncertainties. For discrimination using the photon count $n_{nsc}$, PDFs which only include argon scintillation and dark noise are used.

### 5.3.2 The photon weight under Monte-Carlo PDFs

PDFs from simulation have the advantage that all physical processes that influence the distribution of pulses in time can be modelled with arbitrary accuracy, whereas in the model, simplifications are made. Also, the uncertainty of parameters that are used in the simulation can be propagated directly to changes in the pulse shapes by changing the input-parameters of the simulation. This is not always possible for the model PDF, in particular for the shape of the peak, which is modelled using a purely empirical function.
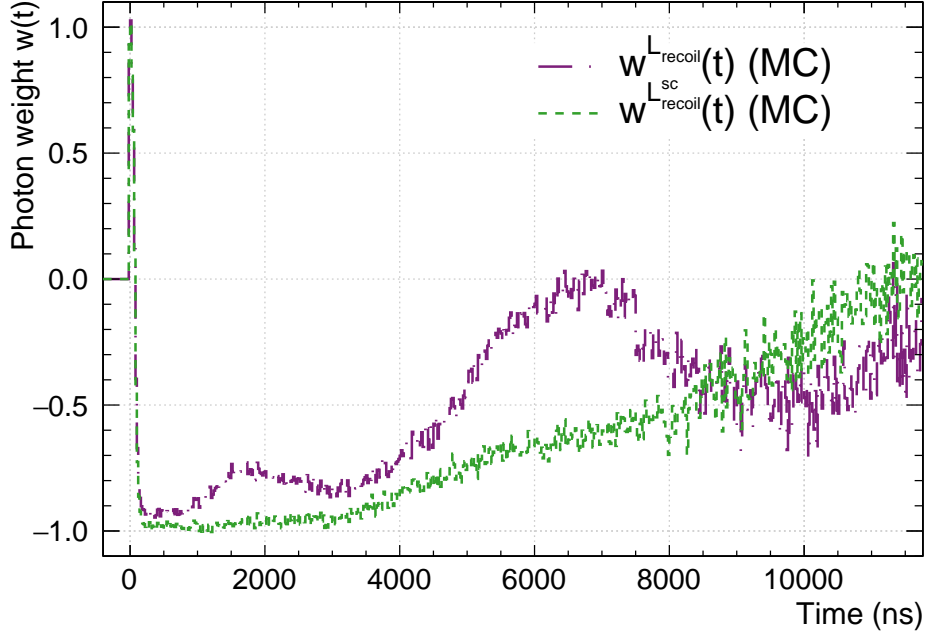
Figure 21: $w(t)$ built by using pulse shapes of approximately 50,000 simulated electronic and nuclear recoils events.

A sample of Monte Carlo PDFs for electronic and nuclear recoils and the resulting photon weight $w(t)$ are shown in figure 21. This is compared to the result of the full model from the previous section. Overall, while over 100,000 events are simulated over the energy region used, statistical fluctuations . While simulation of a higher number events is possible, it is very CPU-intensive and changing the PDFs after a potential change in the detector or an improvement of the simulation software would require a complete re-run of the simulation. Therefore, the likelihood-based discriminators discussed in this work are evaluated using model PDFs.

## 5.4   PSD distributions

The $L_{\mathrm{recoil}}$-variations introduced above are implemented, where model PDFs are used to form the photon weight functions. With the prompt-window-based and likelihood-based discriminators using the charge and $n_{\mathrm{nsc}}$ photon estimate, there are a total of four PSD parameters. Because the distributions of all prompt-window and likelihood-based PSD parameters share the same characteristics, only the distributions of the discriminators using charge are shown below. For the distributions of the parameters using $n_{\mathrm{nsc}}$, see appendix F. For notations and brief descriptions of the PSD parameters and photon estimators used, see the glossary.

### 5.4.1 Electronic recoil background

The electronic recoil distribution of the PSD parameters can be obtained directly in very large statistics ($10^7$ events per day between after data cuts between 50 and 400 PE) from data. The dataset used in the following section are 5 days of data taken 250 days after completion of the LAr fill.
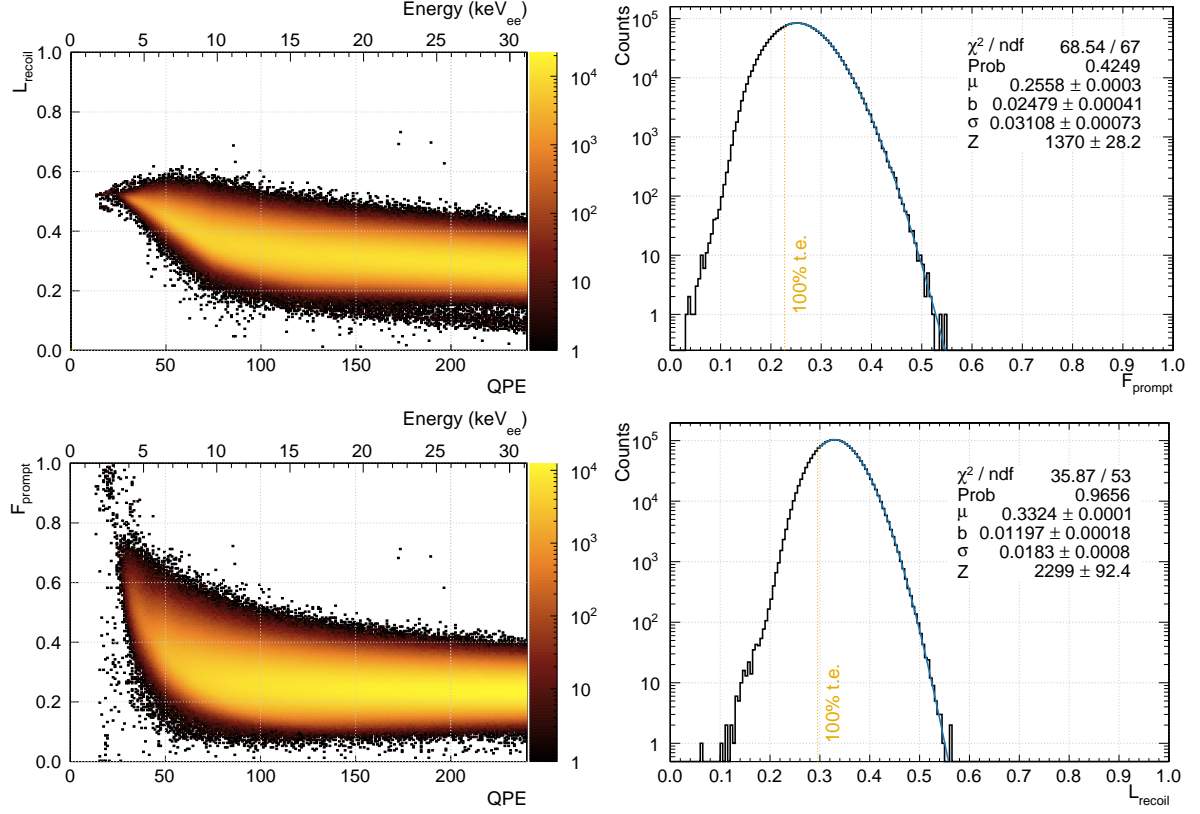


Figure 22: The distributions of data in energy and $F_{\mathrm{prompt}}$ (top left) and $L_{\mathrm{recoil}}$ (bottom left) and projections of the PSD-distributions between 110 and 115 QPE (approx. 15 keV$_{\mathrm{ee}}$) are shown.

Figure 22 shows the distribution of the dataset in $F_{\mathrm{prompt}}$ and $L_{\mathrm{recoil}}$. As mentioned above, the number of events is dominated by $^{39}$Ar electronic recoils which make up a bands in both PSD parameters. Also visible are 4 isolated events with high $F_{\mathrm{prompt}}$ or $L_{\mathrm{recoil}}$-values. The origin of these events is still not fully understood, however they are unlikely to emerge from electronic recoils because of their large separation from the electronic recoil band. The mean $F_{\mathrm{prompt}}$-values at 30 keV$_{\mathrm{ee}}$ are comparable to the singlet fractions shown in figure 18 where a deviation is expected because of triplet light in the prompt window and afterpulsing. The $F_{\mathrm{prompt}}$-band broadens at low energies due to lower statistics of pulses and a worse signal-to noise ratio in these events and bends upwards because of the higher singlet fraction at low energies.

The $L_{\mathrm{recoil}}$ distribution does not broaden as strongly towards lower energies. This can be explained because $L_{\mathrm{recoil}}$ accounts for the signal-to-noise ratio by giving late pulses in the PMT trace less weight.

The singlet fractions of electronic and nuclear recoils converge at low energies. Therefore, all photon weights vanish here and the $L_{\mathrm{recoil}}$-mean at low energies converges towards 0.5.

It should be noted that the distribution is cut off at low $F_{\mathrm{prompt}}$ and low energies due to the trigger efficiency: an event is only recorded when an (uncalibrated) threshold charge equivalent to approximately 20 QPE is exceeded value in a 177 ns time window. Because the peak intensity of an event is typically reached in the prompt-window, this threshold charge is strongly correlated to the charge in the prompt window and $F_{\mathrm{prompt}}$ of the event. Because the prompt window used by the trigger and $F_{\mathrm{prompt}}$ differ and because $F_{\mathrm{prompt}}$ uses the SPE-corrected charge sum, this trigger effect is smeared out in $F_{\mathrm{prompt}}$ and $Q$. As evident from the weight functions shown in the prior section, $L_{\mathrm{recoil}}$ will also be higher for events with a large prompt-charge fraction. Because electronic recoils typically have a lower peak-intensity they are more affected by this effect than nuclear recoils at the same event energy such that it is ensured that the detector is triggered for 100% of events in the WIMP search region.

An effective distribution that describes the 1D-projections of both distributions well over small energy ranges is a gamma distribution convoluted with a Gaussian. The gamma distribution is defined with the PDF $f(x|\mu,b) = \frac{1}{b\mu\Gamma(b^{-1})} \left(\frac{x}{b\mu}\right)^{(1/b-1)} \exp(-\frac{x}{b\mu})$, where $\mu$ is the mean of the distribution and $b$ is a shape parameter. With the width of the Gaussian $\sigma$ and a normalization constant $Z$ the model has four free parameters.

The right side of figure 22 shows the fit of the electronic recoil distributions in $F_{\mathrm{prompt}}$ and $L_{\mathrm{recoil}}$. The fit interval is selected such that 100% trigger efficiency is reached at the lower fit limit. Because the trigger efficiency curve in $L_{\mathrm{recoil}}$ has not been calculated yet, it is assumed that the 100 % trigger efficiency is reached at the same quantile in $F_{\mathrm{prompt}}$ and $L_{\mathrm{recoil}}$ PSD parameters and the lower fit range is set accordingly. Otherwise, this model describes the distributions well with a $\chi^2/\mathrm{ndf} = 68.54/67$ for the $F_{\mathrm{prompt}}$ and $35.87/53$ for the $L_{\mathrm{recoil}}$ distribution.

### 5.4.2 Signal

In order to estimate the position of the nuclear recoil band, the neutron calibration data can be used. Figure 23 shows the distribution of the calibration data in $F_{\mathrm{prompt}}$ and energy. The event rate is still dominated by $^{39}$Ar electronic recoils, however in addition to the dataset shown above, a second band at higher $F_{\mathrm{prompt}}$-values that corresponds to nuclear recoil events is visible. As discussed above, these are not the only type of events that are produced by the neutron source. For example, the neutron source also emits 4.4 MeV-$\gamma$ photons, which are also detected. While they scatter in the argon via electronic recoils, they might produce event topologies very different from $^{39}$Ar events because the particle source is located outside of the detector. For example they might scatter with an electron in the acryl which produces fast Cherenkov light before entering. The resulting event type could be hard to separate from a nuclear recoil in the liquid. Another event that differs but might be hard to distinguish from the expected WIMP interaction are neutrons scattering multiple times in the argon.
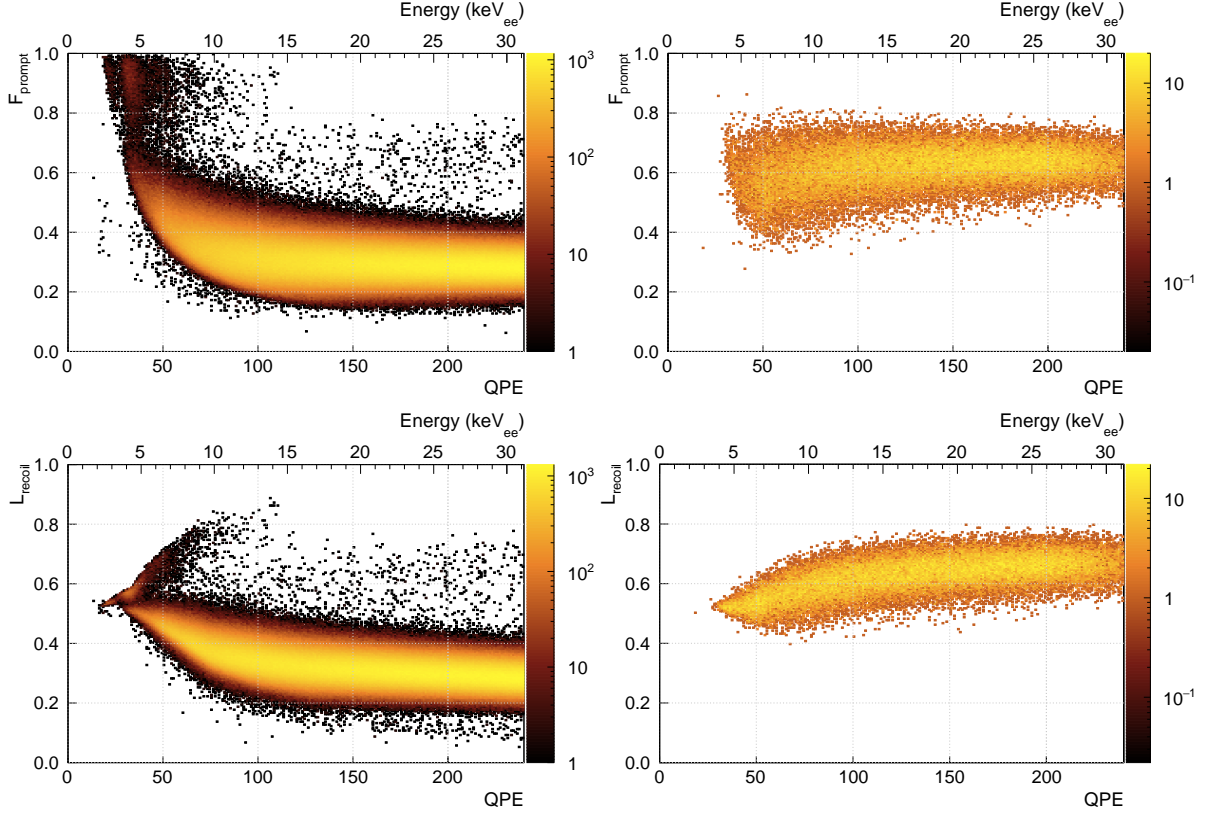
Figure 23: The distribution of AmBe calibration source data (left) and simulated Ar-40 nuclear recoils (right) in $F_{\mathrm{prompt}}$ (top) and $L_{\mathrm{recoil}}$ (bottom) is shown. The AmBe runs used here have a duration of 12 hours.

Projections of the AmBe calibration data in $F_{\mathrm{prompt}}$ are shown and compared to a simulation of the source components in figure 24. Above 140 QPE (18 keV$_{\mathrm{ee}}$), the distribution in $F_{\mathrm{prompt}}$ can be represented by simulated neutrons and gammas. Of the simulated neutrons, a subpopulation at higher $F_{\mathrm{prompt}}$ overlaps with a simulation of single scatter nuclear recoils. Therefore, according to the simulation, neutron scatters in the argon can be selected using an $F_{\mathrm{prompt}} > 0.6$-cut above 140 QPE. This population is only partially representative of WIMP events as significant fraction of the neutrons scatter multiple times in the argon.

At lower energies, the agreement between the AmBe-data and simulated nuclear recoils and gammas becomes worse. A hypothetical population of Cherenkov events could potentially make up for the difference between data and simulation, as shown in in the top two plots of figure 24. This agreement at the current state of the simulation can only be achieved by applying a different cut set on the Cherenkov population than on the other populations. This underlines how difficult reconstruction and extraction of WIMP-like events from the AmBe-calibration data is. Therefore, to estimate the position of the nuclear recoil band at low energies, simulated Ar$^{40}$ nuclear recoils are used in the following section.
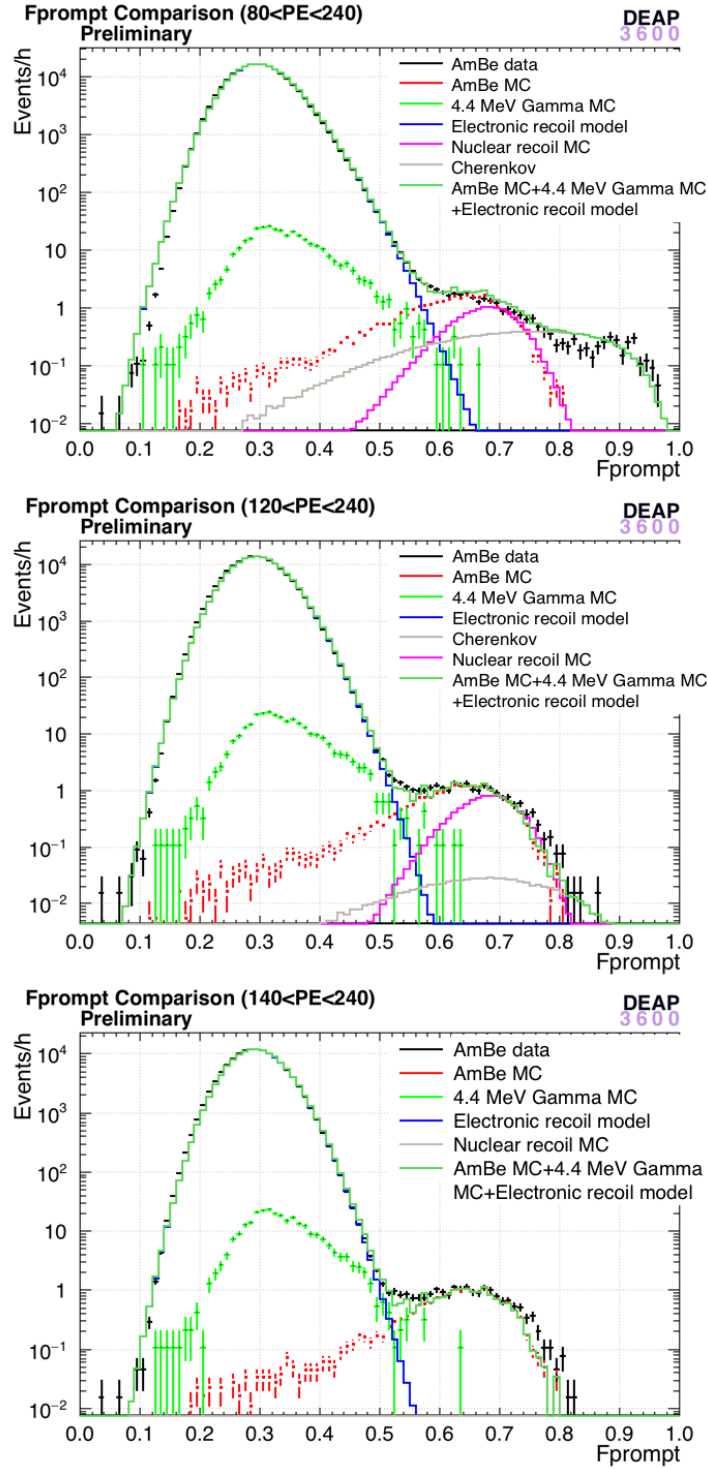
Figure 24: The distribution of AmBe data and simulation is in $F_{\text{prompt}}$ at different energies is shown, top: 80 QPE $< Q <$ 240 QPE, middle: 120 QPE $< Q <$ 240 QPE, bottom: 140 QPE $< Q <$ 240 QPE. The simulated data is split up into events caused by neutrons, gammas and Cherenkov radiation. The different components are scaled relative to each other by hand to make simulation and data match. Taken from [48].

|  | best case | base case | worst case |
|---|---|---|---|
| Singlet fraction rel. to SCENE | + 0.01 | 0 | - 0.01 |
| Quenching factor rel. to SCENE | + 0.01 | 0 | - 0.01 |
| Afterpulsing rate rel. to Calibration | × 90% | × 100 % | × 110% |
| Dark noise rate per PMT (Hz) | 400 | 500 | 600 |

Table 2: The input parameters used for the nuclear recoil simulation. The uncertainties of the SCENE-parameters are the published systematical uncertainties. The uncertainties on the afterpulsing rate are estimated from the analysis presented in appendix D. The dark rate and its uncertainty are estimated using the pre-trigger window of pulse shapes (as in the fit described in appendix C).

To estimate the uncertainties on the position of the nuclear recoil band, the simulation is run two additional times, using a optimistic scenario and pessimistic scenario. In the optimistic and pessimistic scenario, the input-parameters listed in table 2 are set within their uncertainty such that PSD is expected to improve and deteriorate, respectively.

### 5.4.3 Discrimination power

To make an informed decision which PSD parameter to use for dark matter search in DEAP-3600, their ability to separate electronic recoils from the nuclear recoil band has to be quantified. A very simple performance parameter can be defined as

$$\delta = \frac{|\mu_{\mathrm{er}} - \mu_{\mathrm{nr}}|}{\sqrt{\sigma_{\mathrm{er}}^2 + \sigma_{\mathrm{nr}}^2}}. \tag{33}$$

Here, $\mu_{\mathrm{er}}, \sigma_{\mathrm{er}}$ and $\mu_{\mathrm{nr}}, \sigma_{\mathrm{nr}}$ are mean and standard deviation in the electronic and nuclear recoil band, respectively. This parameter therefore measures the separation of the two bands normalized by their width.

|  | $\mu_{\mathrm{nr}}$ - $\mu_{\mathrm{er}}$ | $\sqrt{\sigma_{\mathrm{nr}}^2 + \sigma_{\mathrm{er}}^2}$ | $\delta$ |
|---|---|---|---|
| $F_{\mathrm{prompt}}$ | 0.366 | 0.079 | 4.64 ± 0.09 |
| $L_{\mathrm{recoil}}$ | 0.294 | 0.062 | 4.72 ± 0.09 |

Table 3: $\delta$ for $F_{\mathrm{prompt}}$ and $L_{\mathrm{recoil}}$ between 110 and 120 QPE. The uncertainties are calculated via the standard error of the mean and variance.

Table 3 shows $\delta$ for the PSD parameters discussed in the prior section. The means of the electronic and nuclear recoil distributions are closer together for the likelihood-based parameters than for the prompt-window-based parameters. This can be explained by considering the shape of $w(t)$ for both type of discriminators: because $w(t)$ for $F_{\mathrm{prompt}}$ is larger or equal $w(t)$ for $L_{\mathrm{recoil}}$ for all times except $t > 10\mu\mathrm{s}$, where only very few pulses are measured, $L_{\mathrm{recoil}}$ overall uses less pulses to separate electronic and nuclear

recoils. This is however offset by a lower width of corresponding distributions. This is also consistent with the statement above because many of the pulses that are discounted by $L_{\mathrm{recoil}}$ are noise or after-pulses, which broaden the PSD-distributions. As a result $\delta$ is slightly lower for the likelihood-based parameter than for the prompt-window-based parameter.

While a big advantage of $\delta$ is that it does not assume the distributions to follow any model, it does not necessarily measure the PSD-performance of the corresponding parameters. For example, tails in the PSD-distributions that point away from the other population would increase the standard deviation and therefore lower $\delta$. As discussed in 1, backgrounds, even when predicted by a model, significantly impair the sensitivity of the experiment. Therefore, in order to maximize its WIMP-sensitivity, DEAP-3600 has to achieve a background-free WIMP region of interest. This implies that the expected number of electronic recoil events that 'leak' into the nuclear recoil band over the lifetime of the detector is a better measure of the PSD performance than $\delta$. To estimate this number, we first quantify the position of the WIMP search region in the given discrimination parameter. In all parameters considered here, background events have a lower parameter value than signal events. We thus have to define a lower bound of the signal region, called the signal threshold (ST). The position of the ST is defined based on the quantile of signal events that falls above the ST. For a nuclear recoil acceptance (n.r.a.) of 90 %, the ST is set at the parameter value above which 90 % of the nuclear recoil events lie. Knowing the shape of the discrimination parameter distribution for background events, we can now calculate the probability that a background event will occur above the ST, which is equal to the quantile of the electronic recoil distribution at this point. This probability will be referred to as the leakage probability $P_{\mathrm{leak}}$ in the following section. In particular, the parameter value and nuclear recoil acceptance at a leakage probability of $10^{-9}$ are evaluated. This number is chosen because with the high electronic recoil background rate of approximately $10^7$ events per year per PE-bin this corresponds to an expected leakage past this point in the order of $10^{-2}$ per year. Because PSD improves exponentially towards higher energies, this is an acceptable leakage probability at the lowest energy bin used for the dark matter analysis, such that the leakage over the full WIMP search region stays in the order of $10^{-1}$, as it will be shown below.
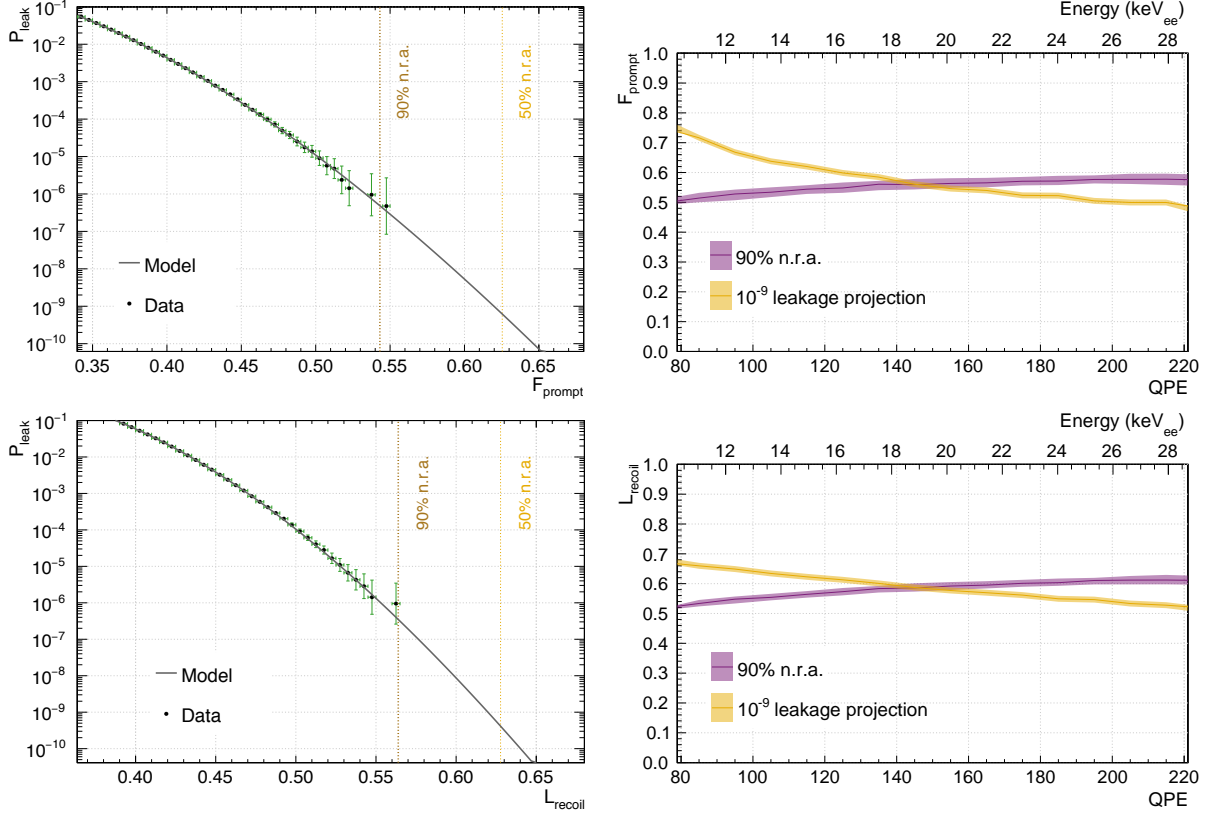
Figure 25: Left: The leakage probability in 110 to 120 QPE as a function of the discrimination parameter value. Right: The $10^{-9}$-leakage projection estimated from the electronic recoil distribution model. This is compared to the 90 % nuclear recoil acceptance line obtained from Monte Carlo.

The leakage probability as a function of $F_{\mathrm{prompt}}$ and $L_{\mathrm{recoil}}$ between 110 and 120 QPE is shown in figure 25 (left). The leakage estimates from data is the fraction of events that exceed the corresponding value of the parameter and the uncertainties shown are the Wilson score interval [49], which is an approximation for the uncertainties on estimates of binomial probabilities. Because the dataset used contains $5 \cdot 10^7$ events, the lowest leakage probability that can be estimated directly from data is $(5 \cdot 10^7)^{-1} = 2 \cdot 10^{-8}$. To obtain lower leakage probabilities, the model that was fit to the electronic recoil background in figure 22 is extrapolated into the lower leakage probability-region. The estimated $P_{\mathrm{leak}}$ in model and data agree within the Wilson score intervals. Using the model-estimate the leakage probabilities at the 90 % quantile of the nuclear recoil acceptance (n.r.a.), as well as the $F_{\mathrm{prompt}}$ and $L_{\mathrm{recoil}}$-values and $10^{-9}$ leakage probabilities can be calculated. The positions of the parameter values at which $10^{-9}$ projected leakage probability is reached is shown as a function of energy on right of figure 25. These estimates are obtained over energy bins of 10 QPE (80 to 90 QPE, 90 to 100 QPE..). The uncertainties on the leakage position are obtained using the uncertainties of the fit parameters and are calculated using a Monte Carlo simulation, where upon each iterations fit parameters are randomly drawn from Gaussian distributions with mean and width determined by the fit. The uncertainty shown is the standard deviation of the distribution obtained this way. To put the achieved leakage into perspective relative to the nuclear recoil distribution, the 90 % n.r.a. line is also shown. Here, the uncertainties are calculated by

43

varying the parameters on afterpulsing, dark rate, singlet fraction and quenching factor that enter the Monte Carlo as shown in table 2. The separation between the nuclear recoil and leakage band increases monotonically as a function of energy. This is expected because for electronic recoil events with a high number of PE it is less likely that a large fraction of triplet excimers decay within a few nanoseconds and the event mimics a nuclear recoil that way. Also, the singlet fractions produced by electronic and nuclear recoils diverge as a function of energy. An energy threshold can be defined as the QPE-value at which the leakage and nuclear recoil acceptance bands cross. This value is found to be 19.4 keV$_{ee}$ for $F_{prompt}$ and 19.2 keV$_{ee}$ for $L_{recoil}$. Note that the lowest energy used in our WIMP search analysis will be significantly below these values, only that less nuclear recoil acceptance is reached there. In our 'first results' publication the WIMP search region started at $\sim 11$keV$_{ee}$ [43].
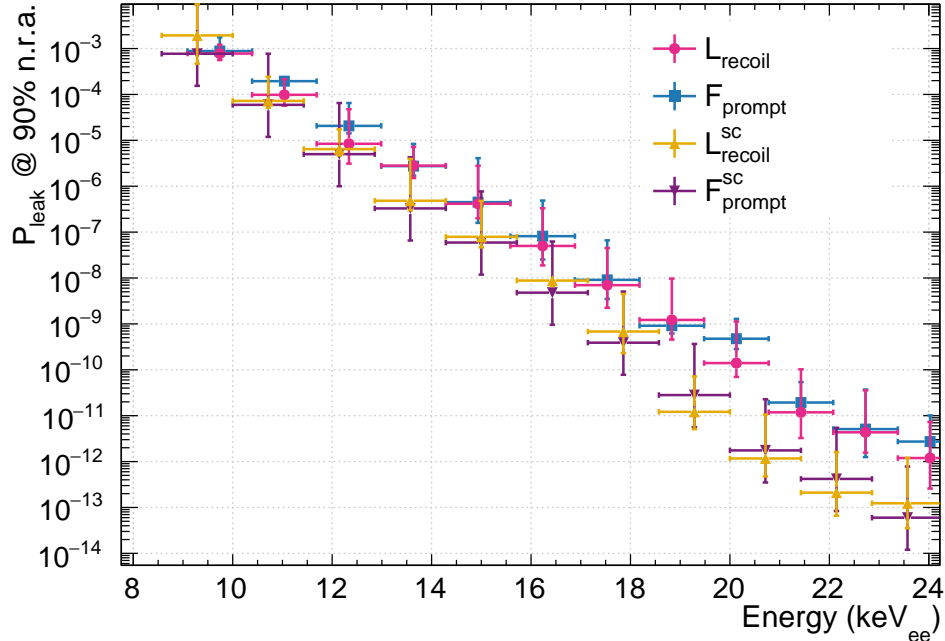
# 6 Discussion



Figure 26: Leakage probabilities for the $F_{prompt}$, $L_{recoil}$, $F^{sc}_{prompt}$, $L^{sc}_{recoil}$ discriminators at 90 % n.r.a. as a function of keV$_{ee}$. These are obtained by fits and extrapolations. The horizontal errors show the energy range used for the corresponding fit. The vertical errors are obtained from a Monte Carlo, where upon each iteration the leakage probability is evaluated with model parameters are drawn from a Gaussian distributions with mean and width resulting from the PSD-fits. The upper and lower error bars are then the corresponding semideviations, i.e. standard deviations only considering values that are greater or smaller than the expected value.

The leakage probability at 90 % n.r.a. is also evaluated as a function of energy. This allows for direct comparison of the performance of $F_{prompt}$ and $L_{recoil}$ and is shown in figure 26. For all parameters, the

PSD performance improves exponentially by an order of magnitude per 15 keV$_{\text{ee}}$.

| | $\delta$ | $P_{\text{leak}}$ at 90 % n.r.a. | Energy threshold in keV$_{\text{ee}}$ |
|---|---|---|---|
| $F_{\text{prompt}}$ | $4.64 \pm 0.09$ | $4.5 \cdot 10^{-7}(+2.6 \cdot 10^{-7}/-4.2 \cdot 10^{-8})$ | $19.4 \pm 1.7$ |
| $L_{\text{recoil}}$ | $4.72 \pm 0.09$ | $3.4 \cdot 10^{-7}(+3.4 \cdot 10^{-7}/-8.2 \cdot 10^{-8})$ | $19.2 \pm 1.9$ |
| $F_{\text{prompt}}^{\text{sc}}$ | $5.53 \pm 0.11$ | $4.8 \cdot 10^{-8}(+8.8 \cdot 10^{-8}/-5.4 \cdot 10^{-9})$ | $17.5 \pm 2.0$ |
| $L_{\text{recoil}}^{\text{sc}}$ | $5.47 \pm 0.11$ | $6.5 \cdot 10^{-8}(+1.0 \cdot 10^{-7}/-6.7 \cdot 10^{-9})$ | $18.0 \pm 1.7$ |

Table 4: Separation ($\delta$), leakage and energy threshold for various discriminators. $P_{\text{leak}}$ and $\delta$ are evaluated between $(14.3 \pm 0.4)$ keV$_{\text{ee}}$ (110 QPE or 100 NSC) and $(15.6 \pm 0.4)$ keV$_{\text{ee}}$ (120 QPE or 109 NSC). The energy thresholds are obtained by fitting exponentials to the leakage probabilities shown in figure 26. The energy threshold is then the energy at which the fit function crosses the $10^{-9}$ leakage-probability line. The errors are the standard deviations of the energy threshold distributions obtained by varying the fit parameters within their uncertainties. Uncertainties from the light yield are not considered here.

The performance of all PSD parameters that were investigated in this work is summarized in table 4. The discriminators using $n_{\text{nsc}}$ perform significantly better than the corresponding version using charge. This implies that indeed the reduction of afterpulsing and SPE-noise strongly benefits PSD. Within the discriminators using the same photon-estimate, the likelihood-based discriminators and prompt-window-based discriminators demonstrate very comparable PSD performance. This is expected because as shown in figure 19, the photon weights used by both discriminator types are very similar in the first 5 µs, where 90 % of the pulses are detected.

The $L_{\text{recoil}}$ appears to perform slightly better than $F_{\text{prompt}}$. This indicates that the discounting of pulses that are measured at times where afterpulsing and other noise components are dominant improves PSD. When comparing $L_{\text{recoil}}^{\text{sc}}$ and $F_{\text{prompt}}^{\text{sc}}$, the opposite trend is observed: here the prompt-window-based discriminator performs slightly better than the likelihood-based version. This is surprising because according to the Neyman-Pearson Lemma, the likelihood ratio should be the better discriminator. One reason for the superior performance of the prompt-window-based discriminators could be that for evaluation of the likelihood, an approximation is used in $L_{\text{recoil}}$, where the pulses are assumed to be independent. While this assumption holds for argon scintillation and dark noise, it does not for afterpulsing, where pulses are directly caused by other pulses. Because $L_{\text{recoil}}^{\text{sc}}$ and $F_{\text{prompt}}^{\text{sc}}$ use the afterpulsing-corrected photon count $n_{\text{nsc}}$, this approximation should be valid for these parameters and can not explain this difference. Another possible explanation could be the comparison of distributions in data and Monte Carlo that was done to obtain the PSD performance measures. Because the likelihood-based parameters rely on the exact timing information, they could be more affected by mismatches between Monte Carlo and data. For example, because all afterpulsing falls into the late window, $F_{\text{prompt}}$ is only sensitive to the afterpulsing rate, whereas $L_{\text{recoil}}$ is sensitive to the precise timing distribution of afterpulsing.

One component that has been found to differ in data and Monte Carlo and strongly affects the average pulse shape is given by delayed TPB light reemission. In figure 19 it was shown that delayed TPB

fluorescence has an impact on the photon weights, such that the information carried by photons emitted between 200 and 4000 ns decreases. Generally, delayed light TPB will be harmful to PSD because re-emitted delayed photons effectively lose their timing information.

In DEAP, the delayed TPB light emission is hard to extract from the electronic recoil data because here, the late light is dominated by the triplet component. By comparison of pulse shape-fits described in appendix C using models with and without delayed TPB fluorescence it can be concluded that this component is likely also seen in DEAP. Here, it was found that with the $\chi^2$ of fits including the TPB model measured by Segreto et al [38] is significantly lower than the $\chi^2$ of fits without this component. Note that the TPB fluorescence parameters are fixed to their published values such that no additional parameters are added. At the same time, no TPB fluorescence model is currently implemented in Monte Carlo. The Segreto paper uses a combination of different exponentials to represent the TPB fluorescence pulse shape. Another measurement has become available in late 2017 and is compared to the effective model that is used by Segreto in figure 27. Here, a more complicated model is used that assumed that the delayed fluorescence is produced by the decay of triplet states. Because these triplet states have a non-luminous deexcitation channel, the time structure of their decay rate does not follow an exponential. While the two measurements agree in the order of magnitudes of the measured intensities, the lifetime measured by the Princeton group appears to be significantly lower. Differences in the two measurements include the thickness of the TPB layer which is 1000 µg cm$^{-2}$ in the E. Segreto and 265 µg cm$^{-2}$ in the C. Stanford measurement. The estimated thickness of the TPB layer in DEAP is: 300 µg cm$^{-2}$) [30].
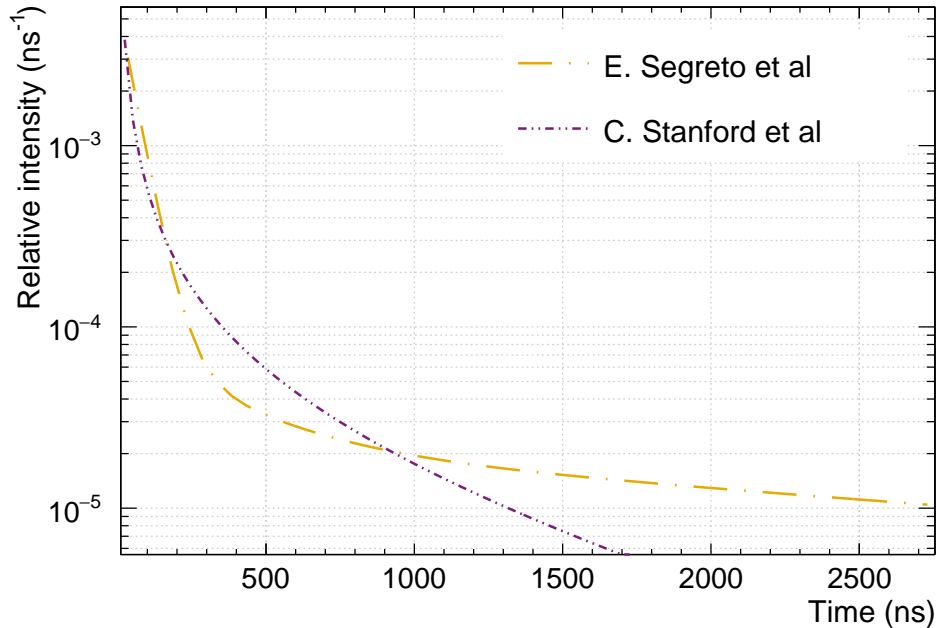


Figure 27: TPB fluorescence trace measured by E. Segreto et al [38] and C. Stanford et al [39]. Both measurements of the TPB response to argon UV photons are obtained by reducing the argon scintillation time structure to a delta-like peak by contaminating the argon with nitrogen.

46

While it would be good to understand the discrepancies of the two measurements in the future, the Princeton measurement is scheduled to be implemented in the DEAP detector Monte Carlo. This is a necessity to get a better estimate on the position of the nuclear recoil band regardless of which PSD parameter is chosen for a future dark matter analysis. The fraction of delayed photons will cause a shift an $F_{\mathrm{prompt}}$ whereas $L_{\mathrm{recoil}}$ will be sensitive to the precise structure of the TPB fluorescence pulse shape. It will be interesting to repeat the PSD analysis under the new Monte Carlo to see whether TPB fluorescence plays a role in the underperformance of $L_{\mathrm{recoil}}^{\mathrm{sc}}$.

It should also be mentioned here that while using Monte Carlo (MC) to obtain the signal position in $F_{\mathrm{prompt}}$ can be justified with the good agreement of the $F_{\mathrm{prompt}}$ distributions for AmBe-calibration and Monte Carlo, the same comparison between data and MC has not been done yet for $L_{\mathrm{recoil}}$. It could be the case that the agreement is worse here than for $F_{\mathrm{prompt}}$ for the reasons named above. Therefore, comparing the $L_{\mathrm{recoil}}$ distributions in Monte Carlo and data might be misleading. This hypothesis can be tested by using a electronic recoil Monte Carlo instead of the $^{39}$Ar-background data. If the underperformance of $L_{\mathrm{recoil}}^{\mathrm{sc}}$ is indeed due to mismatches in data and MC, the parameter should perform better when its simulated nuclear recoil distribution is compared against the simulated electronic recoil distribution. For the electronic recoil simulation, electrons with flat momentum distribution between 5 keV and 50 keV are simulated homogeneously distributed in the liquid. It is found that when comparing MC with MC, the $\delta$-separation parameter for $F_{\mathrm{prompt}}^{\mathrm{sc}}$ and $L_{\mathrm{recoil}}^{\mathrm{sc}}$ coincide, whereas $\delta$ is lower for $L_{\mathrm{recoil}}^{\mathrm{sc}}$ when comparing data to MC as shown in table 4. This means that indeed mismatches between data and Monte Carlo play a role in the poor performance of $L_{\mathrm{recoil}}^{\mathrm{sc}}$. $\delta$ is used as the PSD performance measure here because it does not require the high statistics in the electronic recoil band that are required for the model fit. This is convenient when using simulated electronic recoils as the simulation is highly CPU-intensive. Despite the weaknesses of $\delta$, it is a very good predictor of the other PSD performance measures as shown in table 4.

As shown in appendix C, the argon triplet lifetime changes over time. This means that in principle, the PDFs used to build the photon weight functions would have to be adjusted after certain periods of times or otherwise the PSD performance achieved by the likelihood-based discriminators might deteriorate as the PDFs start diverging from the pulse shapes. In order to estimate how sensitive $L_{\mathrm{recoil}}$ is to mismatches between the PDFs and the pulseshapes, the PSD performance of $L_{\mathrm{recoil}}$ is evaluated using PDFs which differ from data. Here, an increase and decrease of the triplet lifetime of 50 ns is used, which is double the change that was found in appendix C over one year. The resulting change in $\delta$ is found to be $< 0.01$, which suggests that the PDFs are robust against the detector changes that are expected in DEAP-3600.

Finally, the procedure used to evaluate the leakage probabilities has a few weaknesses. For example, an effective model is used to fit the PSD-distributions. While the agreement between model and data is excellent, in principle there is no physical reason why the model should be representative of the 'real leakage' when extrapolated over the several order of magnitude. For $F_{\mathrm{prompt}}$, it has been shown in [44]

that the distribution can be described by physically motivated model. This is done by calculating the probability that a pulse is a prompt pulse taking into account among others the singlet fractions, argon scintillation time structure, dark noise, SPE-charge distribution and afterpulsing probabilities. A full physics model for the distribution of the prompt-window-based parameters in DEAP-3600 is under development. With regard to a physical model of the $L_{\mathrm{recoil}}$-distribution, knowing the probability that a pulse is a prompt or late pulse is not sufficient to describe the distribution of $L_{\mathrm{recoil}}$ as $L_{\mathrm{recoil}}$ takes into account the exact timing information of each pulse. Therefore, the physical model distribution of likelihood-based discriminators is much more complicated and can also not be evaluated analytically. Distributions would in this case have to built from Monte Carlo which is an additional disadvantage of likelihood-based discrimination against prompt-window-based discrimination.

# 7  Conclusion and Outlook

DEAP-3600 is a single-phase liquid argon dark matter detector. The largest background, with more than $10^9$ events in the preliminary energy region of interest of 15 to 30 keV$_{\mathrm{ee}}$ for the planned exposure, is the beta decay of $^{39}$Ar. Pulse shape discrimination is used to discriminate this electron-recoil type background from the nuclear recoil events we expect WIMP recoils to induce. PSD in LAr is based on two effects: Scintillation light is emitted from a singlet and a triplet excimer with a 2 order of magnitude lifetime difference, and the fraction of each excimer that is excited depends on the type of interaction. PSD thus boils down to estimating the fraction of singlet and triplet excimers as accurately as possible for each event. At the low energies where WIMP scattering events are expected to occur, less than 300 photons are detected per event. The statistical variations in photon arrival time for such a small number of photons make PSD challenging.

The goal of this work was to implement and compare the performance of different PSD parameters.

Pulse shape discrimination is predicated on an understanding of the time structure of a typical event. Therefore, the average pulse shape for $^{39}$Ar beta-decays was studied in detail. Since Ar-39 beta decay is the main background in DEAP-3600, a large number of sample events was available for analysis. It showed that the detector response function, dominated by PMT afterpulsing, dark noise, and delayed light emission of the wavelength shifter TPB, has a significant impact on the measured pulse shapes.

DEAP currently uses a simple "prompt photon" based PSD method. This method does not make use of the full information collected for each event, and does not attempt to account for the known detector response function. Including more of the available information about the detector response starts at the photon counting level. The standard estimator uses photons counted by the charge method: The charge of each PMT pulse is divided by the mean single-photoelectron charge to estimate the number of photo electrons and thus the number of photons that arrived at the time of each pulse. A second

existing estimator attempts to remove the known parts of the detector response function. It determines the most likely number of photons in a PMT pulse, based on the known arrival time of the pulse, the LAr scintillation PDF, and the afterpulsing PDF, which is known from PMT calibration. I found that this estimator creates a biased pulse shape. The source of this bias was investigated and the estimator was modified to eliminate the bias. The different photon counting methods yield two prompt-based discriminators: $F_{\text{prompt}}$, the most naive estimator, and $F_{\text{prompt}}^{\text{sc}}$, which uses a photon count that includes information about the detector response and LAr scintillation physics.

In addition to or conjunction with basing the PSD discriminator on a better estimate for the photon count, additional information can be included in the PSD method itself. A likelihood-based discriminator based on [47] was developed, which makes use of the full photon timing information available in an event. Unlike prompt-based discriminators, likelihood discriminators require pulse shape PDFs for signal and background. These are used to determine how likely it is that the photon timing distribution of a given event matches the signal or background distribution. Different ways to produce such PDFs, including basing them on measured data, on Monte Carlo detector simulation, and on mathematical models, are explored and discussed. I found that background and signal PDFs based on a mathematical description informed by measured pulse shapes works best. The two different photon counting methods again yield two likelihood-based discriminators: $L_{\text{recoil}}$ and $L_{\text{recoil}}^{\text{sc}}$.

The new likelihood discriminator assigns a weight to each detected photon based on the photon arrival time. I showed how these weights are calculated based on the signal and background PDFs. In order to compare this method to the existing prompt-based method, equivalent weights for the prompt-based estimator were derived. In order to further compare the PSD power of the simple charge-based photon counting method to the more advanced probabilistic photon estimation method, the definition of the weights was extended for non-integer estimates of the photon count.

The likelihood weights are a measure for how much information is contained in a photon arriving at a given time. The influence of the detector response and the photon counting method is illustrated based on these weights. This is a novel way to determine the influence of detector response on the PSD power and to compare PSD methods.

The performance of each PSD estimator was evaluated by comparing the event energy (that is the number of detected photons) at which the probability to find a background event in the signal region is $10^{-9}$ or smaller. The signal region is defined such that the signal-acceptance is 90 %. The position of the signal region and its uncertainties are evaluated here using detector Monte Carlo simulation. A second, equivalent measure, used here is the leakage probability at 15 keV$_{\text{ee}}$.

The performance of PSD discriminators that use the likelihood-based photon count is significantly better than the same discriminator using the charge-based photon count. This shows that afterpulsing and

the uncertainty on how many photons are in a PMT pulse degrade PSD performance, and that this degradation can be mitigated by better analysis techniques.

The likelihood-based PSD method using charge performs only slightly better than the equivalent prompt-window based discriminator, whereas the likelihood based method using the Bayesian photon count performs slightly worse. This result does not stem from any weakness of the likelihood algorithm implemented here, but is a consequence of liquid argon scintillation physics. Study of the likelihood weights shows that the prompt-based discriminator's equivalent weights are already close to optimal. This can be understood by considering the large difference between the argon excimer lifetimes. At any given pule time, one of the two excimers strongly dominates the scintillation PDF, so that the photon information content as a function of time approximates a step-function, which is captured adequately by the prompt-based discriminator.

This result also shows that removing detector effects at the level of photon counting is better than including detector effects in the likelihood function. Any advantage of the likelihood-based over the prompt-based discriminator, for the same photon counting method, comes from its better handling of detector effects. Use of the Bayesian photon count in a prompt-based PSD method already mitigates detector effects sufficiently. The difference between prompt and likelihood-based PSD methods might be larger for scintillators where the scintillation response can not be so cleanly divided into two components, such as the BC-501 liquid scintillator [50].

I conclude by recommending $F_{\mathrm{prompt}}^{\mathrm{sc}}$ as the PSD-parameter to use for dark matter search in DEAP-3600, because this parameter conserves the useful analytical properties of a prompt-based discriminator while achieving an excellent PSD result. This is under the assumption that an energy calibration for the Bayesian photon is unproblematic, which has not been verified yet. Also, the simulation which DEAP relies on to estimate its signal distribution should be improved by implementing a TPB fluorescence model.

# Appendix

## A    Data selection

This work is focused on the electronic recoil liquid argon scintillation background in DEAP-3600, so data cuts are established which select these events. Other event types that are seen by the detector are introduced in section 3.4. Below, all cut variables and values that are applied to all data presented in this work can be found. These cuts are equivalent to the cuts that were used for the published dark matter analysis paper [43].

**Low-level cuts**    Events that show behaviour of the electronics or where the DAQ-software was run under a setup unsuitable to detect physics events are removed.

These includes the following cases:

- a digitzer has a bad baseline

- a digitizer was saturated

- event is close to pulse-test-event

- an unconnected channel measures a pulse

- the DAQ is too busy to read out digitizers

- trigger/digitizers are out of sync

- the charge integral of a pulse is truncated

**Event position**    Another population of events observed by DEAP-3600 are so-called surface events, i.e. events that arise from the decay of radioactive material on the surface of the acrylic cryostat. These events can produce a WIMP-like signal when a daughter nucleus of an alpha decay is pushed into the liquid argon, where it scatters in a nuclear recoil. Because this scatter occurs close to the detector surface, these events can be removed by cutting events with features that are typical for surface events. Two variables are used in this work to remove events that likely come from the edges of the detector: the fraction of charge and the fraction of estimated photons $n_{\mathrm{nsc}}$ seen by the PMT which saw most charge and $n_{\mathrm{nsc}}$ during the event, respectively. The cut values used are $> 20\%$ and $> 7\%$. These cuts also effectively remove Cherenkov events, where typically only very few PMTs see a short light flash.

**Pile-up cuts**    For each event, approximately 2.5 us of PMT traces before the trigger time are recorded. NHitsEarly is the number of pulses in the first 1.6 us in this pre-trigger window. This cut removes pile-up events and events that overlap with a long-lifetime component of a prior event. The cut value used is 3. Additionally, only events are considered which were triggered 20 µs after the last event was triggered or

more.

Also, sophisticated algorithms are implemented which spot and remove pile-up events by looking at their time structure.

# B    PE counting and afterpulsing removal

Afterpulsing complicates the event reconstruction in various ways. For example, it worsens the energy resolution by adding noise to the pulse shape. This also lowers the pulse shape discrimination power that can be achieved. Additionally, afterpulsing can distort the charge distribution across the PMT array and therefore complicates reconstruction of the event position. Through a model of the argon scintillation and the afterpulsing response an algorithm can be implemented which removes or underweights pulses that are likely afterpulses. This is realized by performing a Bayesian analysis for each pulse [51]:

$$p(n_{\text{sc}} + n_{\text{ap}} = n_{\text{pe}}|Q) = p(Q|n_{\text{pe}})/p(Q)p(n_{\text{sc}} + n_{\text{ap}} = n_{\text{pe}}). \tag{34}$$

Here, $n_{\text{sc}}$ is the number of photons that caused the pulse and $n_{\text{ap}}$ is an integer measure for the afterpulsing charge in units of the SPE-charge. Because the charge of afterpulsing and scintillation is indistinguishable, an informative prior $p(n_{\text{sc}} + n_{\text{ap}} = n_{\text{pe}})$ is constructed to evaluate the probability of either using the scintillation and afterpulsing physics in the experiment. The posterior $p(n_{\text{sc}} + n_{\text{ap}} = n_{\text{pe}}|Q)$ is then used to give an estimate of the number of photons and afterpulsing that caused the pulse. In addition to removing afterpulsing, this estimate could potentially reduce the noise that is introduced by the broad charge-distribution that is produced by a discrete number of photons.

The number of photons seen by a PMT during the full event can then be estimated as the sum over the estimated number of non-afterpulses in each pulse seen by this PMT. This value summed over all PMTs gives an estimate of the total photons in an event $n_{\text{sc}}^{\text{ev}}$.

## B.1    Evaluating the prior

Priors are generally used to incorporate prior knowledge into a parameter estimate. In this case, this is the prompt fraction of light (i.e. $F_{\text{prompt}}$ in equation 17) of the event and the total charge observed by the PMT looked at during the event $n_q^{\text{pmt}}$.

Pulses, especially when consisting of multiple subpulses, can span over a length of $> 100$ ns. This means that a pulse could contain an afterpulse which was caused by a subpulse of the same pulse. This interdependence is neglected in this analysis as the afterpulsing and scintillation probabilities within a pulse are treated independently, such that $p(n_{\text{sc}} + n_{\text{ap}} = n_{\text{pe}}) = p(n_{\text{sc}})p(n_{\text{ap}})$.

The theoretical argon scintillation probability distribution function (PDF) combines a flat dark noise

component with two pre-built scintillation PDFs representing the decay of singlet and triplet excimers. Including dark noise in the scintillation prior is useful because both mechanisms follow the same statistics (see below). This combined PDF is built for each event and PMT individually.
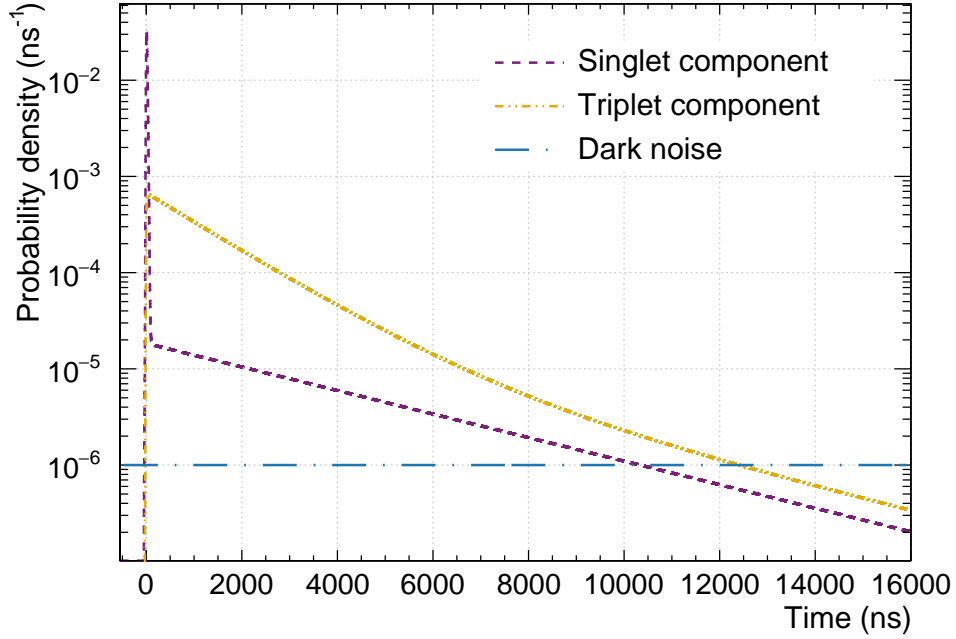


Figure 28: The singlet (purple), triplet (yellow), and dark noise (blue) PDFs over a 16 μs event window.

Figure 28 shows the PDF of the different components used for the non-afterpulsing PDF. A triplet lifetime value of 1390 ns is used to match the fit result from section C and a singlet lifetime of 6 ns is chosen empirically to match the average scintillation peak in data. Both scintillation exponentials are convoluted with a data-driven PMT-response function and the TPB-fluorescence response found in [38].

The fraction of singlet $R_S$ and triplet $R_T = 1 - R_S$ light is estimated by correcting the $F_{\mathrm{prompt}}$-value for the event by the average triplet and noise fractions within the prompt window. The full non-afterpulsing PDF is then

$$P(t) = R_S(1 - f_d)S(t) + R_T(1 - f_d)T(t) + f_d \tag{35}$$

where the singlet and triplet PDFs $S(t)$ and $T(t)$ are normalized to one. The fraction of noise $f_d$ is estimated as the ratio between the expected noise charge per event $\bar{Q}_{\mathrm{dark}}$ for this PMT divided by the charge $Q^{\mathrm{pmt}}$ seen by the PMT during the event looked at. That means:

$$f_d = \bar{Q}_{\mathrm{dark}}/Q^{\mathrm{pmt}}. \tag{36}$$

The pulses emerging from the non-afterpulsing PDF are uncorrelated, such that the probability to have $n_{\mathrm{sc}}$ non-afterpulses in a pulse given that the PMT saw $j$ non-afterpulses during the event is

Binom$(n_{\text{sc}}|j, \int_{t_1}^{t_2} P(t)dt)$. Here, $t_1$ and $t_2$ are the left and right edge of the pulse, respectively. The total number of non-afterpulses $j$ in an event itself is uncertain and is assumed to follow a Poisson distribution with mean $Q^{\text{pmt}}$. To get $p(n_{\text{sc}})$ it is then summed over all possible $j$:

$$p(n_{\text{sc}}) = \sum_{j=n_{\text{sc}}}^{\infty} \text{Pois}(j, Q^{\text{pmt}})\text{Binom}(n_{\text{sc}}|j, \int_{t_1}^{t_2} P(t)dt) \tag{37}$$

Here, in practice it is only summed up to $Q^{\text{pmt}} + 5\sqrt{Q^{\text{pmt}}}$.
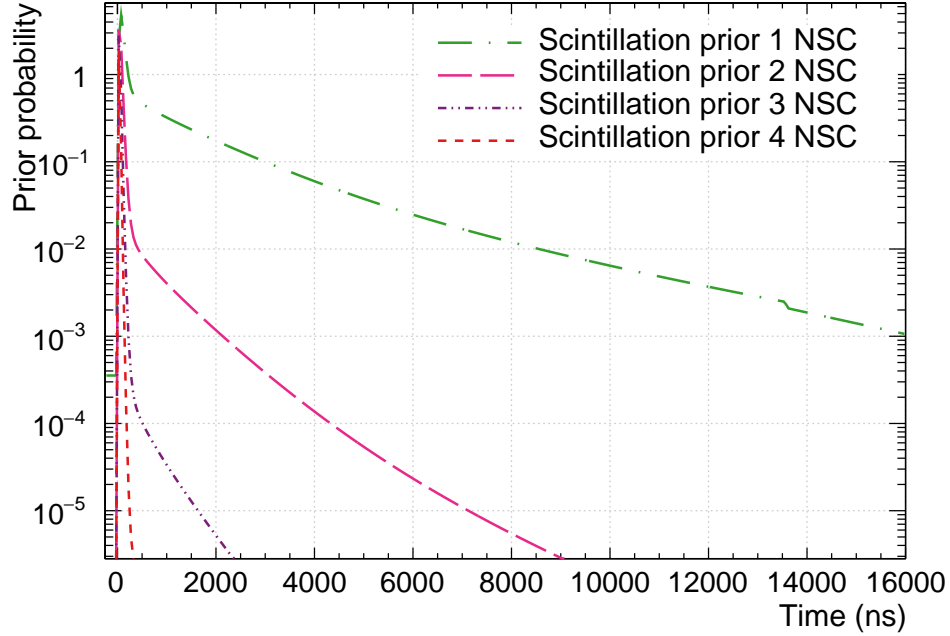


Figure 29: An example for a typical scintillation prior for one PMT. Parameters: $F_{\text{prompt}} = 0.62$, $Q^{\text{pmt}} = 5.75$ QPE, $\bar{Q}_{\text{dark}} = 0.6$

Figure 29 shows a typical scintillation prior for pulses of width 50 ns. The PDFs resemble the argon scintillation PDF, however are distorted differently over time. For example, while a multi-PE pulse is unlikely in the tail of the PMT waveform, it can become more likely than a single PE pulse in the prompt window for higher energy events.

The afterpulsing charge PDF does not have an discrete underlying generator like the photoelectron, for computational reasons however, a discrete charge representative has to be chosen. This choice is arbitrary and a convenient choice is the SPE-charge. Here it is very advantageous to choose the same units as for $n_{\text{sc}}$ as this drastically reduces the number of combinations of $n_{\text{sc}}, n_{\text{ap}}$ with $p(n_{\text{sc}} + n_{\text{ap}} = n_{\text{pe}})$, where $n_{\text{pe}}$ is a discrete charge measure representing the total pulse charge.

The afterpulsing PDF as a function of $n_{ap}$ is built by looping over all prior pulses that the PMT saw during the event and adding up their expected number of afterpulses. The probability to produce an

afterpulse $f(Q_i)F(\delta_{t_i}, n_{\mathrm{ap}})$ with a certain delay after an initial pulse and of charge equivalent to $n_{\mathrm{ap}}$ can be taken from the histogram shown in figure 6. The expected number of afterpulses observed scales linearly with the charge of the initial pulse $f(Q_i) = a + bQ_i$, where $a$ and $b$ were determined separately for each PMT using the calibration measurement (see [32]).

$$p(n_{\mathrm{ap}}) = 1 - \exp\left(\sum_{i=1}^{N_{\mathrm{prev}}} f(Q_i)F(\delta t_i, n_{\mathrm{ap}})\right) \tag{38}$$

Formula 38 shows the Poisson probability that $> 0$ afterpulses of $n_{\mathrm{ap}}$ charge equivalent are observed. Here, $N_{\mathrm{prev}}$ is the number of prior pulses. The possibility of the pulse being produced by two or more afterpulses caused by different prior pulses is ignored here.
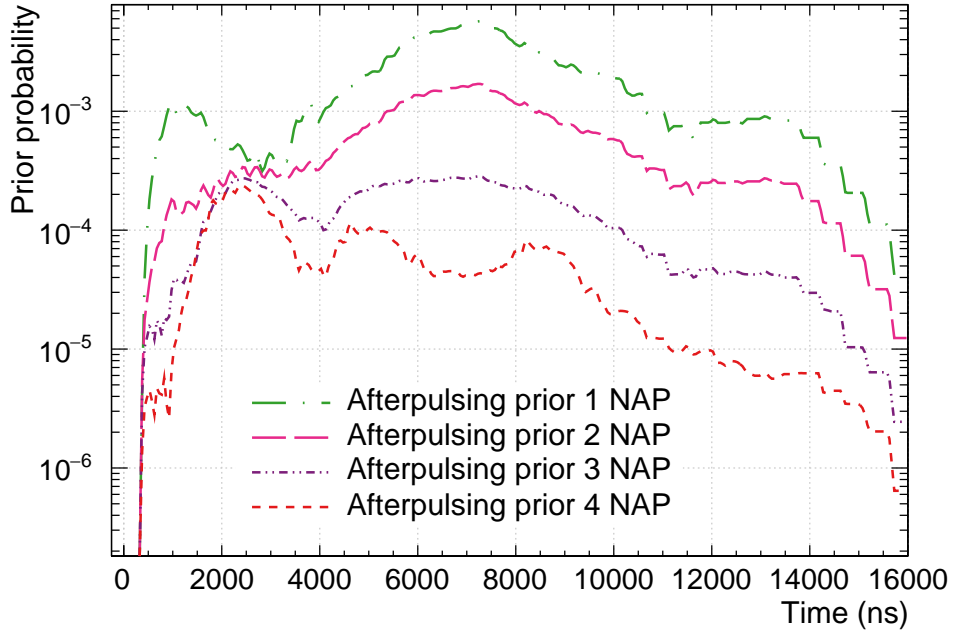


Figure 30: An example for a typical afterpulsing prior.

Figure 30 shows a typical afterpulsing prior for pulses of width 50 ns. Here, as for $n_{\mathrm{nsc}}$ in the scintillation prior, the prior tends to decrease with the amount of charge attributed to afterpulsing, however this effect is less pronounced here. This means that high-charge pulses, especially when late in the PMT trace, are likely afterpulses.

## B.2   Evaluating the likelihood

The charge response to a discrete number of PE $n_{\mathrm{pe}} = n_{\mathrm{sc}} + n_{\mathrm{ap}}$, $p(Q|n_{\mathrm{pe}})$, is modelled as part of the SPE calibration (see figure 5). To obtain the $n$-PE charge distribution the SPE charge distribution is convoluted with itself n times.
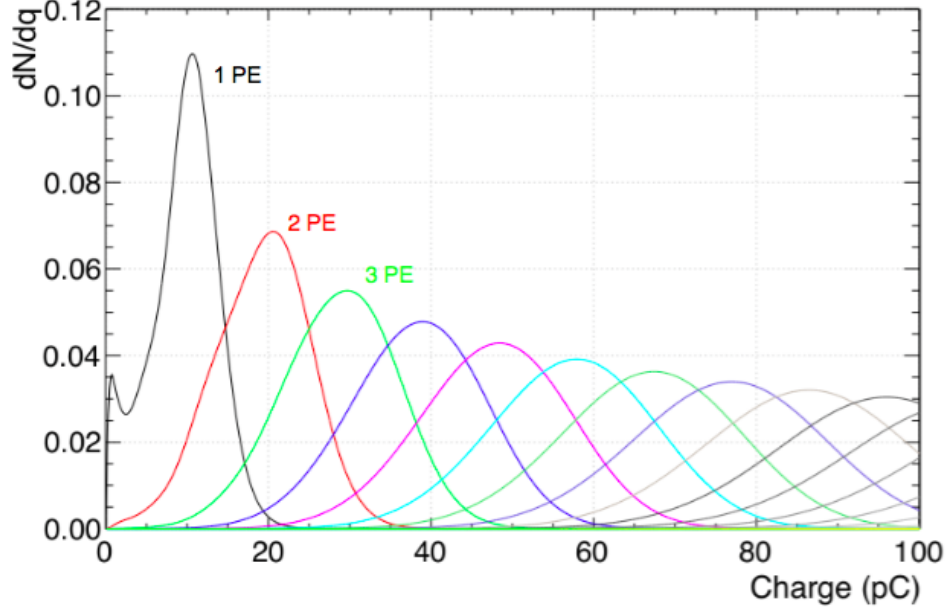
Figure 31: The single photoelectron charge distribution (black) convolved with itself n times taken from [52].

Figure 31 shows the charge model-distribution for different numbers of photons. Due to the central limit theorem the distribution of the sum of charges of $n$-PE approaches a Gaussian. Here, the mean and standard deviation should scale with $n$ and $\sqrt{n}$, respectively, such that

$$p(Q|n_{\mathrm{pe}}) \approx \frac{1}{\sqrt{2\pi}A\sqrt{n}} \exp{-\frac{(Q-(B+Cn))^2}{2(A\sqrt{n})^2}} \tag{39}$$

represents the distributions appropriately, where $A$, $B$, and $C$ are constants determined through fitting the fully convolved distributions for each PMT. In practice this approximation is used for $n > 40$.

The last missing piece to formula 34 is now the probability to see the charge observed $p(Q)$. This is found by marginalising $p(Q, n_{\mathrm{sc}}, n_{\mathrm{ap}}) = p(n_{\mathrm{sc}})p(n_{\mathrm{ap}})p(Q|n_{\mathrm{sc}}, n_{\mathrm{ap}})$ over $n_{\mathrm{sc}}$ and $n_{\mathrm{ap}}$. This by definition normalises the posterior to unity.
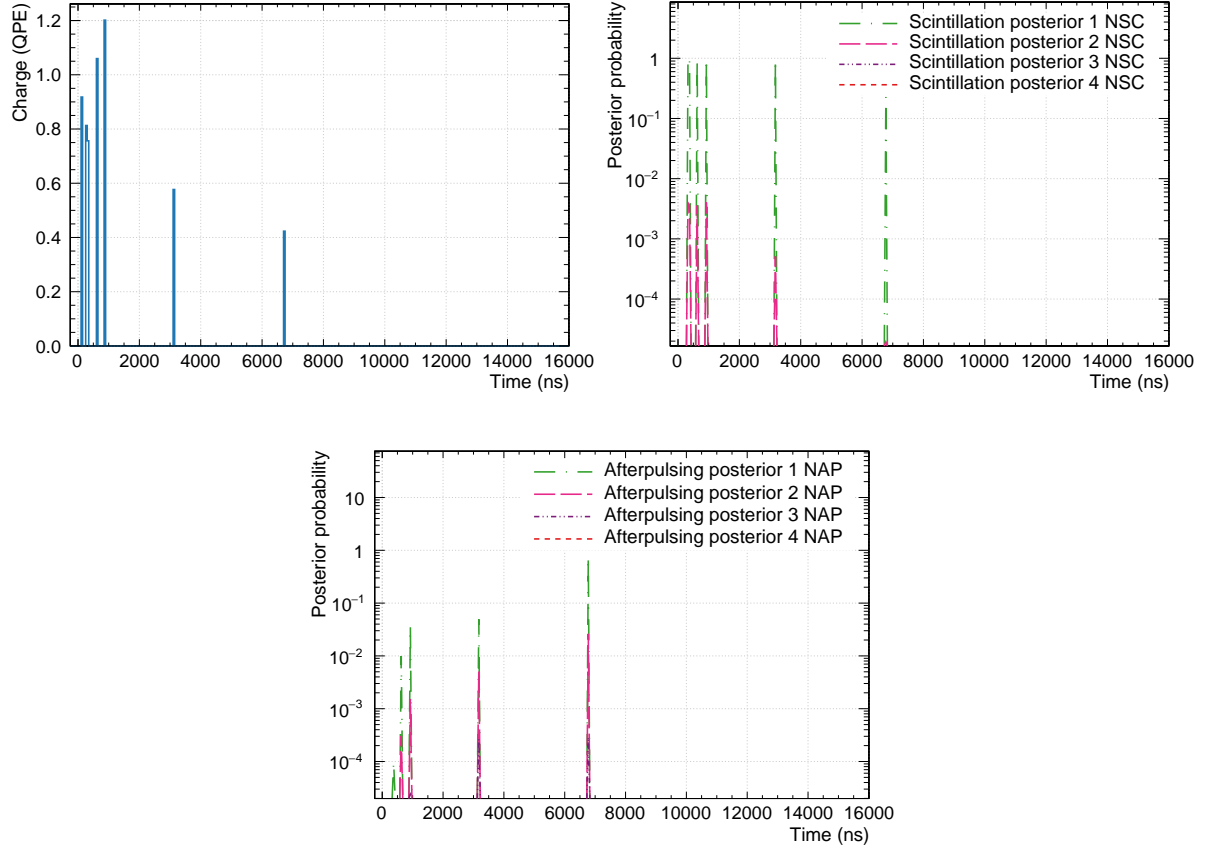
## B.3　The posterior



Figure 32: The scintillation and afterpulsing posterior for a given PMT trace and the priors that were shown in figure 29 and 30.

Figure 32 shows the resulting scintillation and afterpulsing posteriors corresponding to a PMT charge-trace. Here, the priors shown in figure 29 and 30 are used. Both posteriors vanish in the time windows where no pulses are seen as the likelihood to $> 0$ photons or afterpulses vanishes here. As expected, the scintillation posterior decreases for later pulses. This, and the time structure of afterpulsing make the afterpulsing posterior increase as either afterpulsing or scintillation have to account for pulses. For scintillation, multi-PE pulses are always suppressed by at least two orders of magnitude, for the pulse around 6500 ns by four order of magnitude. As already suggested by the prior, high NAP-pulses are much less suppressed for afterpulsing.

It is important to note that there are other sources of pulsing which are not explicitly included in the model used for PE counting. For example, this includes pile-up of the event looked at with low-energy events that can not be recognised by the pile-up removal processors. This contribution has a flat distribution in time and is included in the model by choosing an effective DN-rate which is extracted

in-situ. Here, but especially in the case of pile-up with Cherenkov light, pulses are not uncorrelated anymore as multi-PE flashes are seen by only a few PMTs in a very short time window. It has not yet been investigated how the PE counting algorithm handles such event topologies, which explicitly do not follow the physical model used by the priors.

## B.4 Parameter estimation and validation

Two very prominent estimators in Bayesian statistics are the maximum a posteriori (MAP) estimator and Minimum Mean Square Error (MMSE) estimator. Parameters in the MAP-framework are estimated as the most likely values given the data observed, i.e. the mode of the posterior. Common criticism of this estimator includes that the mode is generally not representative of the entire posterior. The MMSE estimate minimizes the mean squared difference between the parameter and estimator. It can be shown that this is that this equivalent to setting the estimate to its mean over the posterior. This by definition makes the MMSE estimator mean-unbiased under the condition that the model chosen describes the data [53]. A downside of the MMSE-method is that the evaluation of the posterior mean can be computationally very expensive, in particular for posteriors of multiple continuous variables.

In this section the MAP and MMSE estimator are applied and discussed in the context of the afterpulsing-removal-problem.

The MAP-estimates $\hat{n}_{\mathrm{pe}}$, $\hat{n}_{\mathrm{sc}}$ and $\hat{n}_{\mathrm{ap}}$ are chosen such that the posterior $p(\hat{n}_{\mathrm{sc}} + \hat{n}_{\mathrm{ap}} = \hat{n}_{\mathrm{pe}}|Q)$ is a maximized.

In the MMSE approach, the estimate is the parameter mean over the posterior. Here, the integration is not computationally costly as there are only two discrete random variables ($n_{\mathrm{sc}}$ and $n_{\mathrm{ap}}$):

$$\hat{n_{\mathrm{sc}}} = \sum_{n_{\mathrm{pe}}=0}^{n_{\mathrm{pe}}^{\mathrm{max}}} \sum_{\substack{n_{\mathrm{sc}},n_{\mathrm{sc}} \text{ with} \\ n_{\mathrm{sc}}+n_{\mathrm{ap}}=n_{\mathrm{pe}}}} n_{\mathrm{sc}} p(n_{\mathrm{sc}} + n_{\mathrm{ap}} = n_{\mathrm{pe}}|Q) \tag{40}$$

, where $n_{\mathrm{pe}}^{\mathrm{max}} = n_q + 5\sqrt{n_q}$. Note that $\hat{n}_{\mathrm{pe}}$, $\hat{n}_{\mathrm{sc}}$ and $\hat{n}_{\mathrm{ap}}$ do not necessarily take integer values in this case.
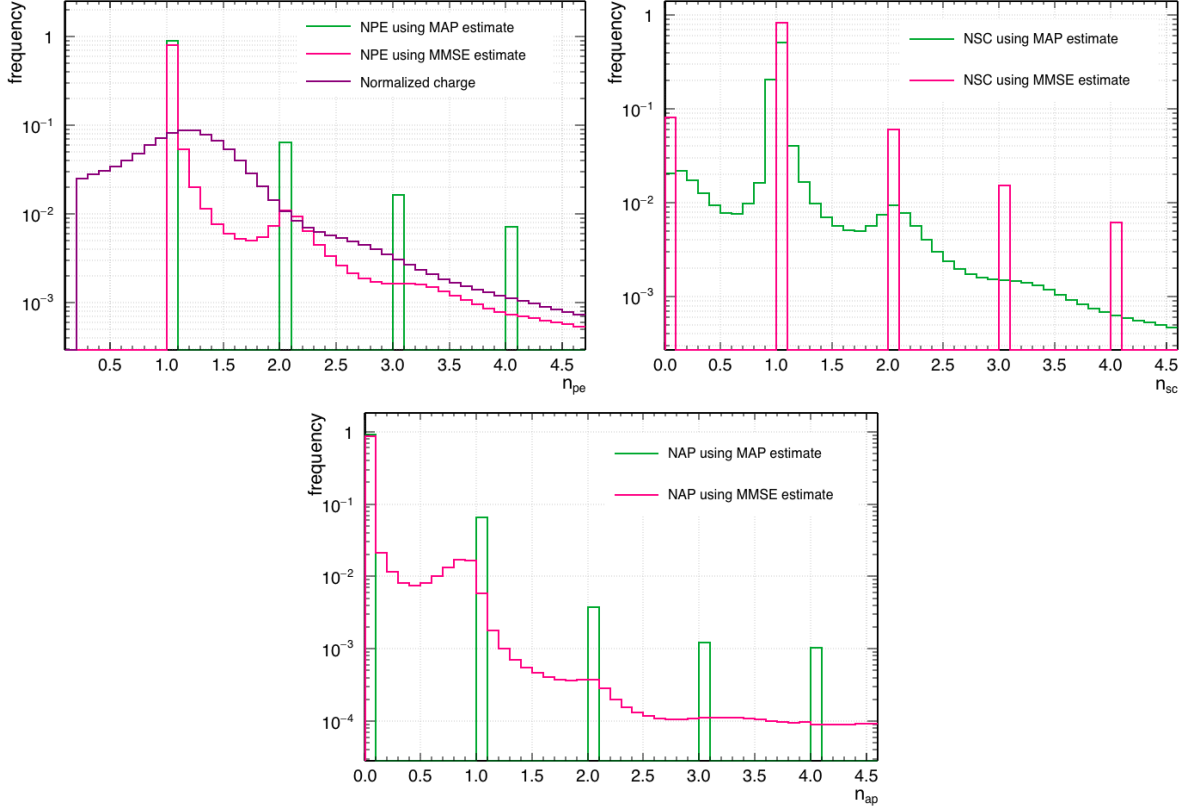
Figure 33: Distributions of the $n_{\mathrm{pe}}$, $n_{\mathrm{sc}}$ and $n_{\mathrm{ap}}$ estimates using the MAP and MMSE estimator. The $n_{\mathrm{pe}}$ distribution is also compared with the normalized charge distribution, which, like $n_{\mathrm{pe}}$, includes scintillation and afterpulsing.

The frequencies of $n_{\mathrm{pe}}$, $n_{\mathrm{pe}}$, $n_{\mathrm{pe}}$ using the two different estimators, as well as the normalized charge distribution is shown in figure 33. As the MAP estimates can only take integer values, their distributions are series of delta-peaks. The $n_{\mathrm{sc}}$ distribution is highly concentrated at the 1 $n_{\mathrm{sc}}$ with approximately 80 % of pulses taking this value. 8 % of pulses have a 0 $n_{\mathrm{sc}}$ which coincides notably well with the average afterpulsing rate across the PMT array. The MMSE estimate of $n_{\mathrm{sc}}$ can take non-integer values, however its distribution is still peaked at lower $n_{\mathrm{sc}}$ integer values. The $n_{\mathrm{ap}}$-distributions are fairly flat towards higher $n_{\mathrm{ap}}$. This is consistent with the calibration as indicated by the afterpulsing prior.

$$L_1 = |n_{\mathrm{sc}} - n_{\mathrm{photons}}| \tag{41}$$

$$L_2 = (n_{\mathrm{sc}} - n_{\mathrm{photons}})^2 \tag{42}$$

$$L_0 = \begin{cases} 0 & \text{if } n_{\mathrm{sc}} = n_{\mathrm{photons}} \\ 1 & \text{otherwise} \end{cases} \tag{43}$$

One good way to evaluate the accuracy of the $n_{\mathrm{nsc}}$ photons estimators, is to calculate their performance under different loss functions. Two sensible loss functions are for example the L1 and L2 deviations

of the estimated and real number of photons in a pulse (see equation 43). Because the real number of photons is not known in data, the loss functions can only be evaluated in Monte Carlo. In theory, if the posterior of the model describes the model well, the MMSE should minimize the $L_2$-Loss. A third loss function $L_0$ is implemented which simply indicates whether the estimate is right or wrong. This is the loss that in theory is minimized by the MAP estimator. This third loss function cannot be evaluated sensibly under the MMSE estimator as this estimator gives non-integer estimates for the integer number of photons.

|  | MAP-estimator | MMSE-estimator |
|---|---|---|
| average $L_1$ | 0.082 | 0.12 |
| average $L_2$ | 0.084 | 0.074 |
| average $L_0$ | 0.082 | - |

Table 5: Performance of the $n_{\mathrm{sc}}$-estimators under different loss functions

Table 5 shows the performance of the two estimators under the defined loss functions. The $L_1$-Loss is about 50 % higher for the MMSE estimator than it is for the MAP estimator. This is intuitive because giving an continuous estimate for a discrete parameter, the MMSE estimator will always be a little bit wrong. These small misses weigh less under the $L_2$-loss function, where the MMSE estimators performs better. The $L_0$ loss indicates that in Monte Carlo, the MAP estimate only differs from the real number of photons in a pulse in 8.2 % of pulses.

# C    Fitting the $^{39}$Ar background pulse shape

The estimation of the singlet and triplet fraction in an event is only enabled by the large difference in the corresponding excimer lifetimes. The singlet lifetime is hard to extract as the shape of the peak of the pulse shape is dominated by the detector response and is known to be $< 10$ ns. The triplet lifetime is known less precisely with literature values ranging from 1300 to 1600 ns. In this section, a fit function is described to extract the triplet lifetime seen by DEAP-3600.

Because the form of the pulse shape peak depends on a variety of optical and PMT-specific parameters that are difficult to model analytically, it is convenient to exclude it from the fit. By choosing the upper fit range as 500 ns, the singlet component with an expected lifetime of a few nanoseconds can be neglected in the fit. The contribution from the decay of triplet excimers is modelled by an exponential:

$$I_t(t) = \frac{I_t}{\tau} e^{t/\tau}. \tag{44}$$

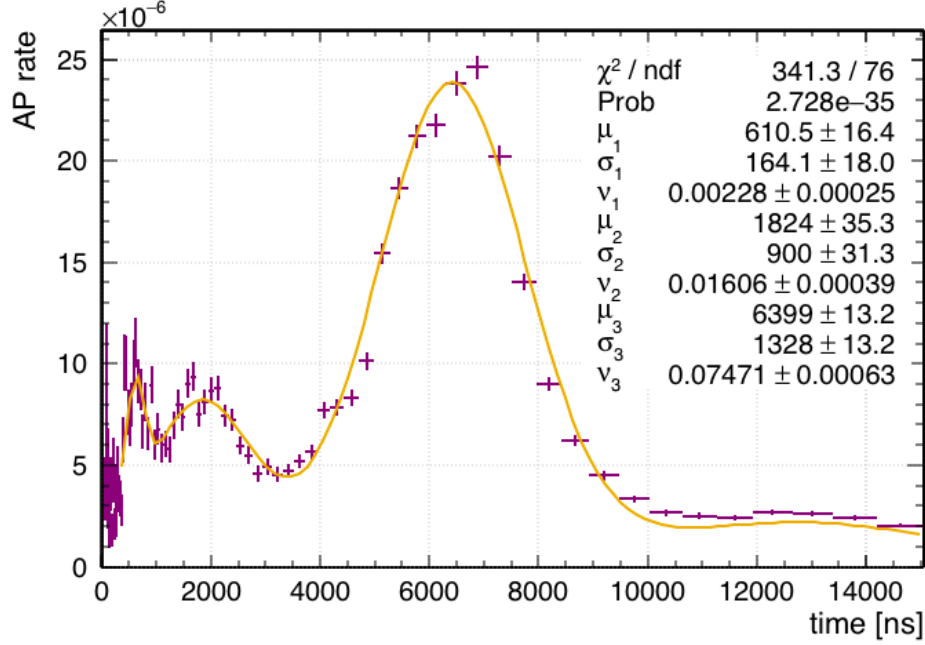Here, $\tau$ is the triplet lifetime and $I_t$ a free scale parameter.

Figure 34: Afterpulsing probability of a single PMT projected onto the time axis. The fit function is three Gaussians plus a constant. The mean and standard deviation of the Gaussians are used for the fit of the full pulse shape of the corresponding PMT.

In order to obtain a timing model for afterpulsing, the calibration-data briefly discussed in 3.2 is used. Figure 34 shows the measured charge-weighted probability to see an afterpulse after a delta-like excitation over time. The different peaks in the afterpulsing probability correspond to different residual molecules in the PMT tube as e.g. heavier molecules wills take longer to reach a dynode. This structure can be fit by a simple model consisting of three Gaussians plus a constant. There are clearly some non-Gaussian features in the timing information, with a fit-$\chi^2$/ndf of 341.3/76, however this simple model is chosen because of its convenient analytical properties. Additionally, the scintillation afterpulsing response will generally have less strongly defined features, as it is smeared out with the long triplet exponential.

To obtain the afterpulsing scintillation response the Gaussians are convoluted with the argon signal, which is modelled with a delta function for the singlet and the exponential in equation 44 for the triplet component:

$$I_{\mathrm{AP}} = I_s \nu_i \mathrm{Gaus}(t, \mu_i, \sigma_i) + 1/2 I_t / \tau \nu_i e^{(\mu_i - t)/\tau + 1/2 \sigma_i^2 / \tau^2} \mathrm{Erfc}(\frac{\mu_i - t + \sigma_i^2 / \tau}{\sqrt{2}\sigma_i}). \tag{45}$$

Here, $\mu_i$, $\sigma_i$ characterise time and shape and $\nu_i$ the charge-weighted probability of the $i$-th afterpulsing Gaussian. $I_s$ represents the scale of the singlet peak and is fixed to the integral over the peak minus the estimated amount of triplet light in that window. The latter is obtained by extrapolating a exponential function that is fit from 500 to 3000 ns to the prompt region. Because the residual gas in the PMTs consists of different molecules, there are a number of afterpulsing peaks centered at different times relative to the peak. The mean and width shown here are taken from the fit in figure 34. Afterpulsing of

afterpulsing is included in the fit by convoluting the afterpulsing response with itself.

Multiple findings suggest that the wavelength shifter used, TPB, has not only a very fast ($< 2$ ns) but also longer decay constants. Specific values were found in [38] where $\nu_{\mathrm{TPB}} = 8\%$ of TPB decays slowly with $\tau_{\mathrm{TPB}} = 3550$ ns. This component should also be included in the fit function as it is highly degenerate with the triplet component and therefore has a big impact on the fit result of the triplet lifetime. The exponential for the long-lived component $\nu_{\mathrm{TPB}}1/\tau_{\mathrm{TPB}}e^{-t/\tau_{\mathrm{TPB}}}$ convoluted with the argon signal gives

$$I_{\mathrm{TPB}} = \nu_{\mathrm{TPB}}(\mathrm{PromptPE}/\tau_{\mathrm{TPB}}e^{-t/\tau_{\mathrm{TPB}}} + \mathrm{LatePE}(e^{-t/\tau} - e^{-t/\tau_{\mathrm{TPB}}})/(\tau - \tau_{\mathrm{TPB}})) \tag{46}$$

The thermionic electron emission is time-independent and therefore simply adds a constant to the pulse shape. The constant is determined by averaging over the pre-trigger-region of the waveform for each PMT.
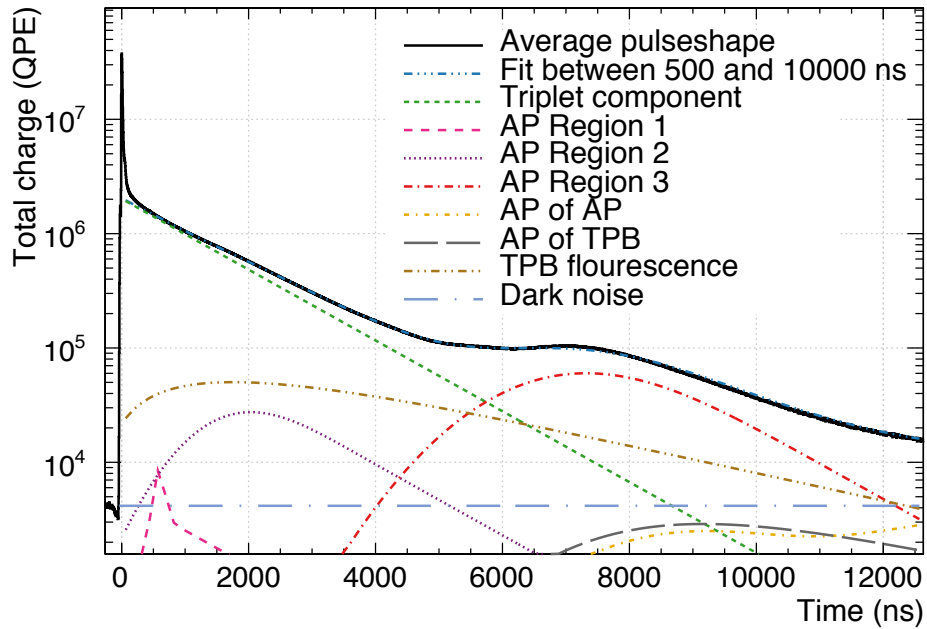


Figure 35: Fit of the pulse shape one week after the fill. The $\chi^2/\mathrm{ndf}$ is $1.6 \cdot 10^5/2.3 \cdot 10^3$. This could be due to imperfections in the afterpulsing and scintillation model which use several simplifications. The fit has 5 free parameters: the triplet lifetime, a scale parameter for the triplet component and the afterpulsing probability, position and width of the afterpulsing region 3.

The pulse shape-fit of a single PMT one week after the completion of the fill is shown in figure 35. In order to fit out the large afterpulsing peak around 6000 ns, 3 additional free fit parameters are required. To limit the number of free parameters that could compensate for a change in the triplet lifetime, the fit range is now set to [500 ns, 3000 ns], where the triplet component dominates. In this fit, all the afterpulsing parameters are fixed to the values obtained from Gaussian fits above.
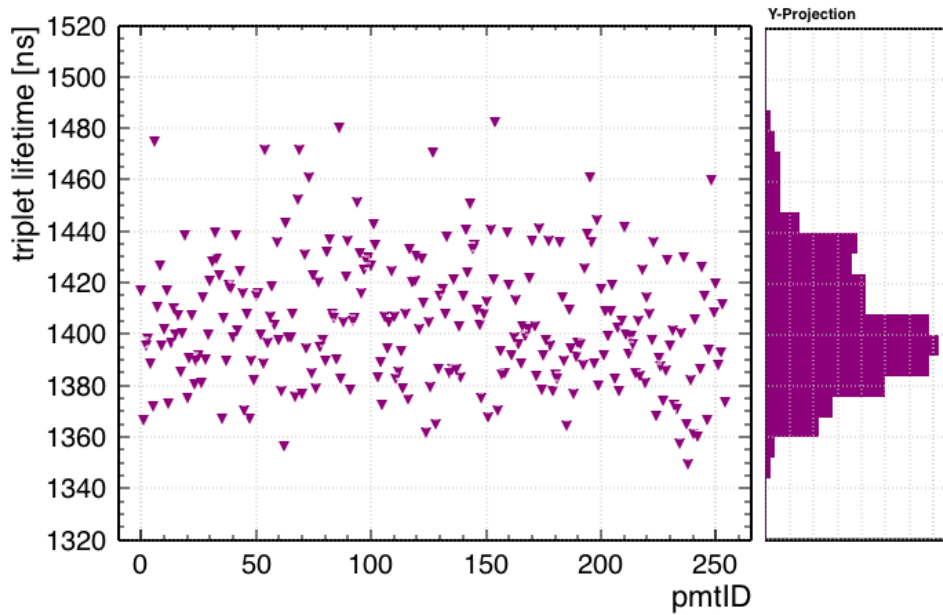
Figure 36: Triplet lifetime from fits of average PMT-pulse shapes against pmtID. The fit is limited to [500 ns, 3000 ns] and only varies the triplet lifetime and a scale parameter.

Figure 36 shows the fit out triplet lifetime for every PMT. The distribution over the PMT array has a mean of 1404 ns and a standard deviation 24 ns. The observed triplet lifetime therefore falls into the wide range of literature values which lie between 1300 and 1600 ns [12, 18, 24, 25]. The large standard deviation across the PMT array, even after correcting for PMT-specific effects, is not fully explained to-date. Varying the TPB fluorescence lifetime within the uncertainties cited in the publication adds an additional 8 ns systematic uncertainty. It should be noted that excluding TPB fluorescence has a very large impact on the fit and results in a fit out triplet lifetime of approximately 1600 ns.
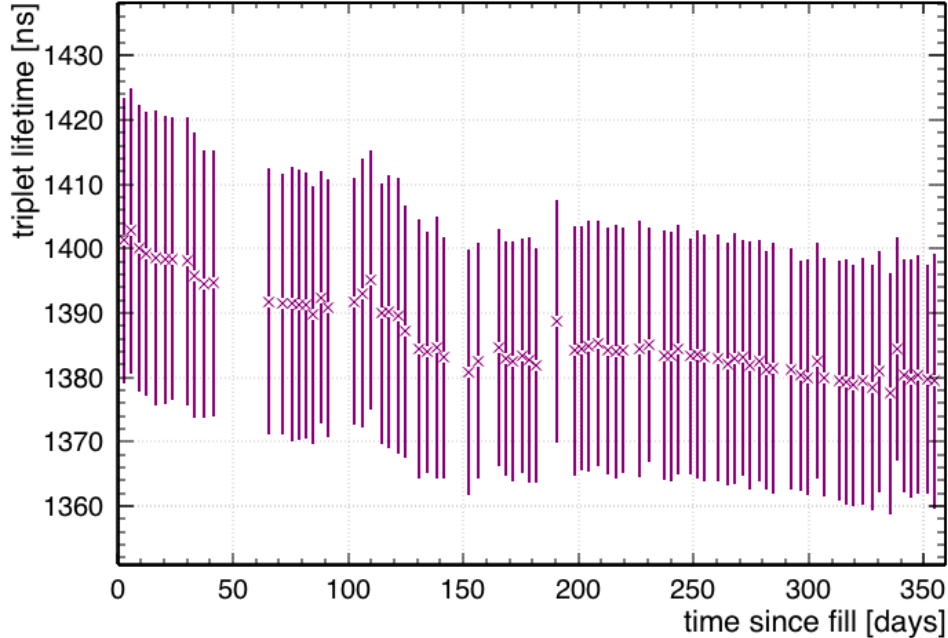
Figure 37: Triplet lifetime against time since completion of the LAr fill. The error bars are the RMS across the PMT array for that run.

**Monitoring the triplet lifetime over time**   As measured in [27–29], the triplet lifetime decreases significantly upon contamination of the argon. As over the lifetime of the experiment material from the detector walls will outgas into the argon, the triplet lifetime is expected to decrease in a period after the detector fill. This effect weakens PSD, which relies on the difference of the singlet and triplet lifetimes and decreases the detector sensitivity. If a significant drop in the triplet lifetime would be observed, the installed argon purification system could be used to conserve the detector sensitivity. Also, a leak in the detector could be spotted using this data. To quantify the impact of outgassing on the triplet lifetime, the fit described in the prior section is repeated over a variety of runs from October 2016 to October 2017. Figure 37 shows the average fit out triplet lifetime across PMT array against time. Here, the outgassing can be observed in the first 150 days after the fill as triplet lifetime decreases with approximately 0.1 ns/day. Afterwards, the stays constant within errors at 1380 ns afterwards. This indicates that it is possible to maintain a strong PSD performance in a single-phase liquid argon detector over a long period of time as discussed in more detail in [54].

# D   In-situ verification of the afterpulsing calibration measurement

Several analysis rely on understanding of the afterpulsing properties of the PMTs. Most notably, the uncertainty of the afterpulsing is the dominant uncertainty in the position of the nuclear recoil band in $F_{\mathrm{prompt}}$. This adds a large uncertainty to the estimated nuclear recoils acceptance and therefore

limits the WIMP sensitivity of the experiment. Here, the afterpulsing model used is based on the afterpulsing measurement described in section 3.2, which was conducted with an unfilled detector. This is one of the reasons for the large uncertainties in the afterpulsing model, as PMTs during that time were approximately $30°$ warmer than after the LAr fill. It is unclear whether and how this affects the afterpulsing probabilities and how the afterpulsing probabilities behave over time in general. To estimate the uncertainty and track the afterpulsing rates over time, the rates can be extracted in-situ from the PMT-pulse shapes. Afterpulsing has a low impact on the PMT-pulse shape at $< 4000$ ns. Therefore, this region can be used to fit out a model that describes all non-afterpulsing components (i.e. argon scintillation, TPB fluorescence and dark noise). The difference between the model and the pulse shape at a later time should then give an estimate of the afterpulsing rate.
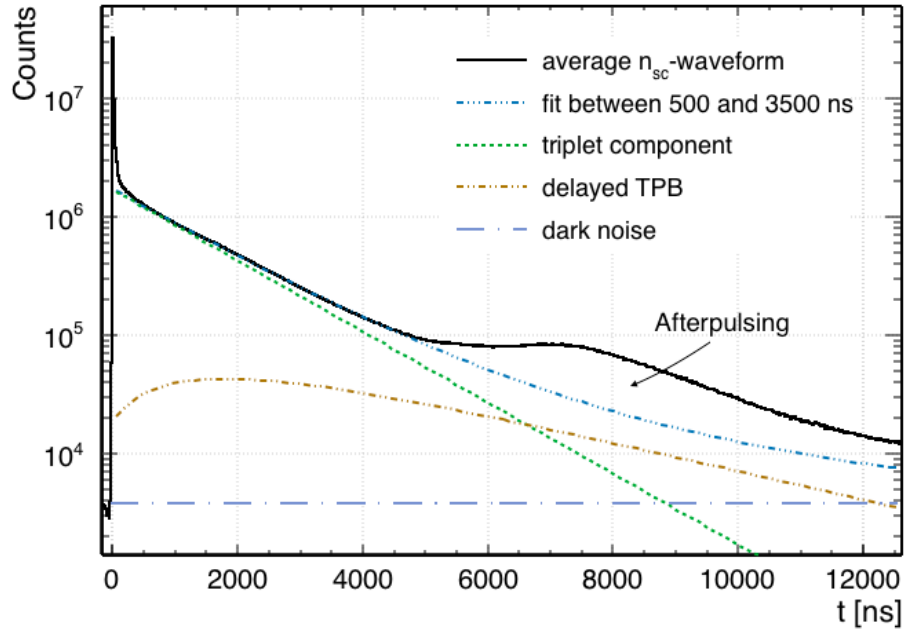


Figure 38: Pulse shape with fit and residual

Figure 38 shows pulse shape, fit and fit components (excluding noise level) for one PMT. The fit is performed from 500 to 3000 ns. The fit function is the same as described in section 4 without the afterpulsing components. To extract an afterpulsing rate, the residual (i.e. the difference between model and extrapolated fit function) is integrated and normalized by the integral of the full waveform. As the pulse shape is charge-weighted, this should approximate the charge-weighted afterpulsing probability. In the following section, this estimate is referred to as the "measured" AP rate, whereas the AP rate calculated from the model is referred to as the "model" AP rate.
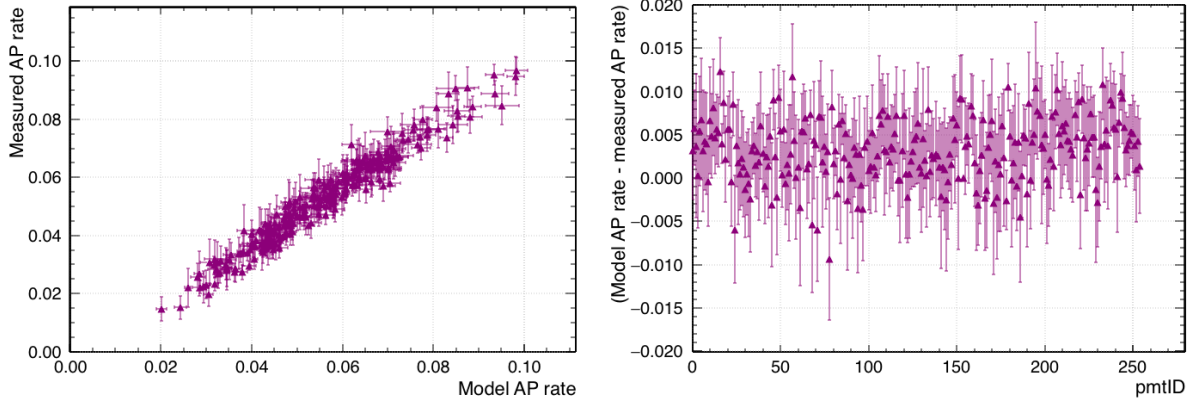
Figure 39: Left: The measured AP rates vs AP rates calculated from the calibration data for a run three days after completion of the LAr fill is shown. Each point here represents a single PMT. The uncertainty of the measured AP rates are obtained from a toy simulation: the fit is repeated 1,000 times where after each iteration parameters of the pulse shape fit (i.e. TPB time constant, dark noise, fit ranges) are drawn from sensible distributions. The error bars are then set to standard deviation of the resulting AP rate distributions. The error bars on the model AP rates are obtained by propagating the uncertainties of the model parameters. Right: model AP rate subtracted by measured AP rate as a function of pmtID.

Figure 39 (left) shows the measured AP rate plotted against the model AP rate for the same PMT. The two datasets are highly correlated with a correlation coefficient of 0.96. This verifies that the method described above indeed extracts a valid estimate for afterpulsing. On the right side of figure 39, the difference of both afterpulsing estimates is shown as a function of pmtID, which is strongly correlated with the PMT temperature. There is no clear trend across pmtID (and therefore temperature). Therefore, there is no indication of a strong temperature dependence on the afterpulsing properties of the PMTs, otherwise a trend over the PMT temperature should be visible.
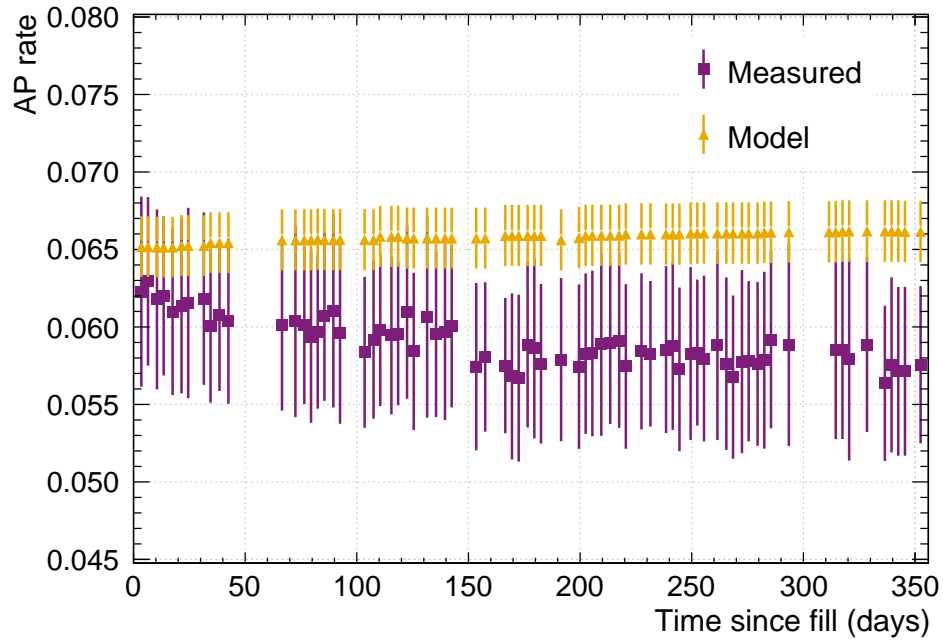
Figure 40: Afterpulsing trend for the model and measured AP rate for PMT 100. The behaviour shown is representative of the average trends of both estimates over the PMT array.

Figure 40 shows both AP rate-estimates over time for a single PMT. The model AP rate changes over time as a function of the SPE charge only, which fluctuates over time, for instance when the PMT-gain in changed. The afterpulsing rate extracted from pulse shapes decreases over time, whereas the calibrated rate increases slightly. This decrease might be due to residual gas accumulating at the PMT walls in the cold PMT over time.

# E  The Gatti-parameter and the likelihood-ratio
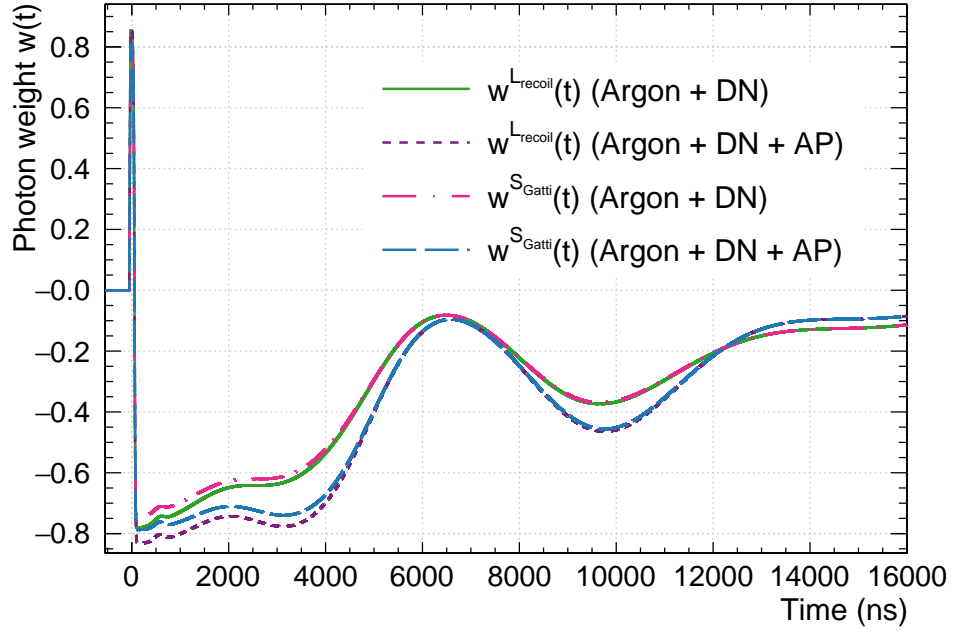


Figure 41: The photon weights under the Gatti parameter $w^{S_{\text{Gatti}}}(t) = \frac{p(t)_{\text{nr}} - p(t)_{\text{er}}}{p(t)_{\text{nr}} + p(t)_{\text{er}}}$ and the log-likelihood ratio $w^{L_{\text{recoil}}}(t) = \log \frac{p(t)_{\text{nr}}}{p(t)_{\text{er}}}$. Because both parameter coincide up to third order around $\frac{p(t)_{\text{nr}}}{p(t)_{\text{er}}} = 1$, both weights coincide around 0 and only show small deviations as they approach -1 and 1.

|  | $\delta$ at 15 keV$_{\text{ee}}$ | $P_{\text{leak}}$ at 15 keV$_{\text{ee}}$ |
|---|---|---|
| $L_{\text{recoil}}$ | $4.72 \pm 0.09$ | $3.4 \cdot 10^{-7}(+3.4 \cdot 10^{-7}/-8.2 \cdot 10^{-8})$ |
| $S_{\text{Gatti}}$ | $4.73 \pm 0.09$ | $3.3 \cdot 10^{-7}(+4.9 \cdot -7/-1.0 \cdot 10^{-7})$ |
| $L_{\text{recoil}}^{\text{sc}}$ | $5.47 \pm 0.10$ | $6.5 \cdot 10^{-8}(+1.0 \cdot 10^{-7}/-6.7 \cdot 10^{-9})$ |
| $S_{\text{Gatti}}^{\text{sc}}$ | $5.48 \pm 0.11$ | $6.4 \cdot 10^{-8}(+4.4 \cdot -8/-9.8 \cdot 10^{-9})$ |

Table 6: Separation ($\delta$) and projected leakage probability at 15 keV$_{\text{ee}}$ for $L_{\text{recoil}}$ and $S_{\text{Gatti}}$ using the two different photon estimators. For the estimator pairs, using the same photon estimate, the leakage performance measure coincide closely as suggested by their weights $w(t)$ (figure 41).
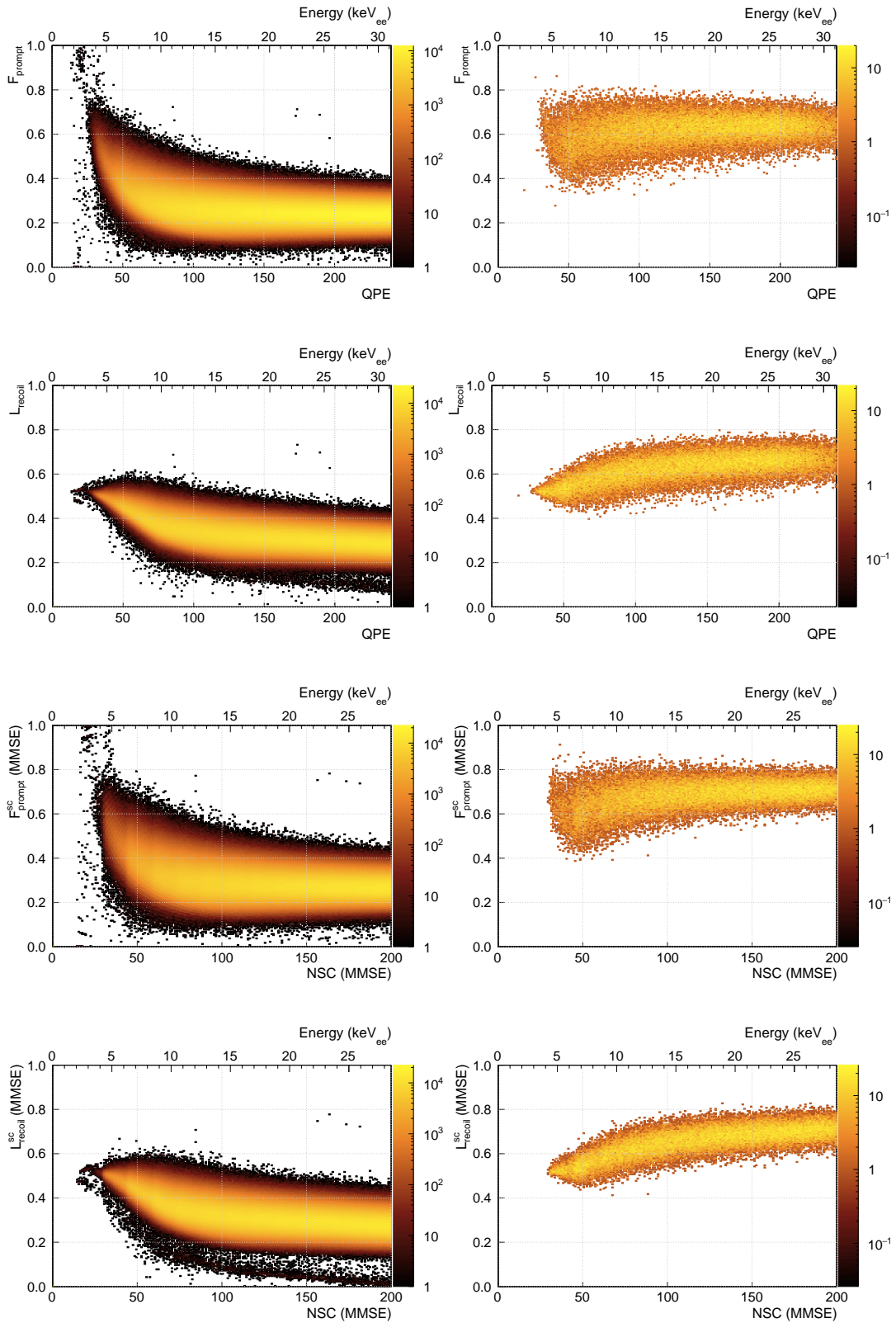
# F    PSD distributions



Figure 42: Distributions of electronic recoil background data (left) and nuclear recoil simulation (right) in energy and the PSD parameters.
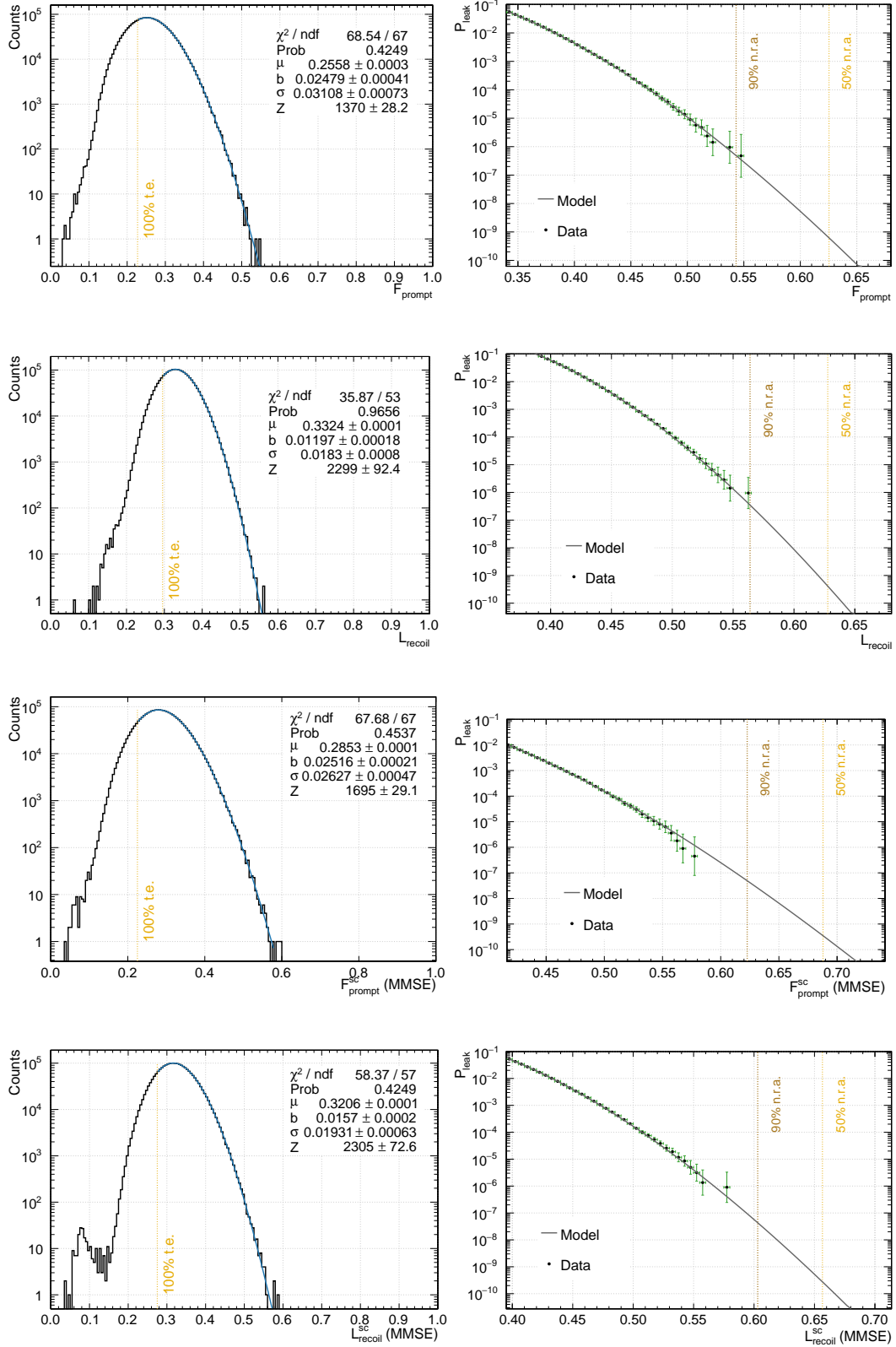
Figure 43: Left: projections of the PSD-distributions between 110 and 120 QPE or 100 and 109 NSC (approx. 15 keV$_{ee}$) are shown. Right: The leakage probability at the same energy as estimated from data and the model.
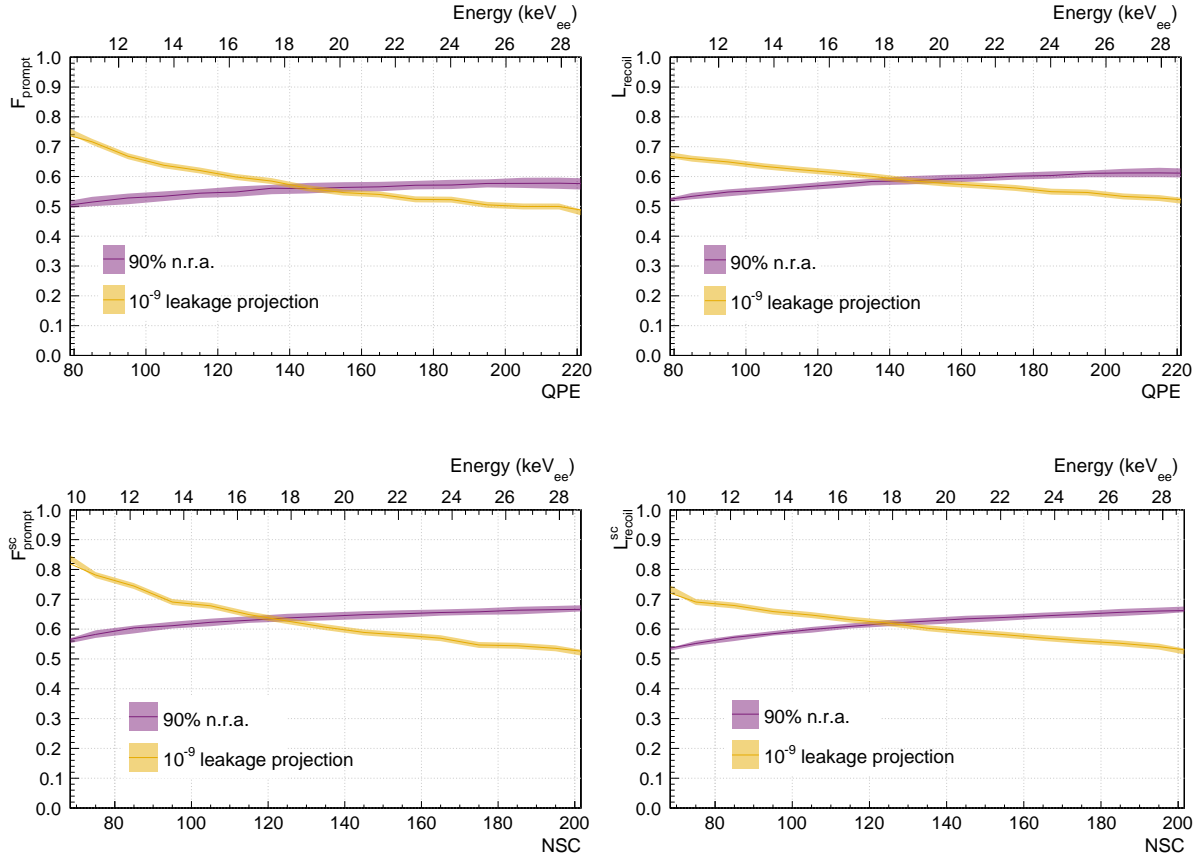
71

Figure 44: The position of the parameter value at which a leakage probability of $10^{-9}$ is reached and the 90 % nuclear recoil acceptance line are shown as a function of energy for all four PSD parameter.

# References

[1] P.F. Smith. Dark matter detection. *Physics Reports*, 1990.

[2] D. Clowe. A direct empirical proof of the exsitence of dark matter. *The Astrophysical Journal*, 2006.

[3] Planck Collaboration. Planck 2015 results. i. overview of products and scientific results. *Astronomy and Astrophysics*, 2015.

[4] K. Freese. Limits on stellar objects as the dark matter of our halo: Nonbaryonic dark matter seems to be required. *arXiv:astro-ph/9904401*, 1999.

[5] Richard J. Gaitskell. Direct detection of dark matter. *Annual Review of Nuclear and Particle Science*, 54(1):315–359, Dec 2004.

[6] M. Aaboud, G. Aad, B. Abbott, J. Abdallah, O. Abdinov, B. Abeloos, S. H. Abidi, O. S. AbouZeid, N. L. Abraham, and et al. Search for dark matter at $\sqrt{s} = 13$ tev in final states containing an energetic photon and large missing transverse momentum with the atlas detector. *The European Physical Journal C*, 77(6), Jun 2017.

[7] IceCube Collaboration. Search for annihilating dark matter in the sun with 3 years of icecube data. *European Physical Journal*, 2017.

[8] D. Hooper. Dark matter annihilation in the galactic center as seen by the fermi gamma ray space telescope. *Physics Letters B*, 2011.

[9] Kluck. Search for low-mass dark matter with the cresst experiment. *arXiv:1711.01285 [astro-ph.IM]*, 2017.

[10] C. Amole. Dark matter search results from the pico-60 c3f8 bubble chamber. *Physical Review Letters*, 2017.

[11] DarkSide Collaboration. Darkside-50 532-day dark matter search with low-radioactivity argon. *arXiv:1802.07198*, 2018.

[12] P.-A. Amaudruz. Measurement of the scintillation time spectra and pulse-shape discrimination of low-energy beta and nuclear recoils in liquid argon with deap-1.pdf. *Astroparticle Physics*, 2016.

[13] C. E. Aalseth. Darkside-20k: A 20 tonne two-phase lar tpc for direct dark matter detection at lngs. *arXiv:1707.08145 [physics.ins-det]*, 2017.

[14] R. W. Schnee. Introduction to dark matter experiments. 2011.

[15] P. Benetti. Measurement of the specific activity of 39ar in natural argon. *Nucl. Instrum. Methods A*, 2008.

[16] Sonnenschein. Measurement of ar39 in argon.

[17] T. Pollmann. Pulse shape discrimination studies in a liquid argon scintillation detector. Master's thesis, Max-Planck-Institut fuer Kernphysik, 2007.

[18] Akira Hitachi. Effect of ionization density on time dependence of luminescence from liquid argon and xenon. *Physical Review B*, 1983.

[19] C. Amsler. Luminescence quenching of the triplet excimer state by air traces in gaseous argon. *JINST 3 P02001*, 2008.

[20] M Miyajima, T Takahashi, S Konno, T Hamada, S Kubota, H Shibamura, and T Doke. Average energy expended per ion pair in liquid argon. *Phys. Rev. A*, 9(3):1438–1443, 1974.

[21] A. Hitachi. Luminescence quenching in liquid argon under charged-particle impact: Relative scintillation yield at different linear energy transfers. *Physical Review B*, 1992.

[22] C. Regenfus. Study of nuclear recoils in liquid argon with monoenergetic neutrons. *Journal of Physics: Conference Series 375*, 2012.

[23] H. Cao. Measurement of scintillation and ionization yield and scintillation pulse shape from nuclear recoils in liquid argon. *Physical Review D*, 2015.

[24] W. H. Lippincott, K. J. Coakley, D. Gastler, A. Hime, E. Kearns, D. N. McKinsey, J. A. Nikkel, and L. C. Stonehill. Scintillation time dependence and pulse shape discrimination in liquid argon. *Physical Review C*, 78(3), Sep 2008.

[25] T. Heindl. The scintillation of liquid argon. *A Letters Journal Exploring the Frontiers of Physics*, 2010.

[26] T. Doke. Absolute scintillation yields in liquid argon and xenon for various particles. *Jpn. J. Appl. Phys.*, 2002.

[27] R. Acciarri. Effects of nitrogen contamination in liquid argon. *JINST*, 2010.

[28] B.J.P. Jones. A measurement of the absorption of liquid argon scintillation light by dissolved nitrogen at the part-per-million level. *JINST*, 2013.

[29] R Acciarri, M Antonello, B Baibussinov, M Baldo-Ceolin, P Benetti, F Calaprice, E Calligarich, M Cambiaghi, N Canci, F Carbonara, and et al. Oxygen contamination in liquid argon: combined effects on ionization electron charge and scintillation light. *Journal of Instrumentation*, 5(05):P05003–P05003, May 2010.

[30] DEAP Collaboration. The deap-3600 dark matter search experiment. *Astroparticle Physics*, 2017.

[31] Franksweb. http://www.frankswebspace.org.uk/scienceandmaths/physics/physicsgce/d1-5.htm.

[32] The DEAP Collaboration. In-situ characterization methods for the hamamatsu 5912 photomultiplier tubes used in the deap-3600 experiment. *JINST*, 2017.

[33] H.O. Meyer. Dark rate of a photomultiplier at cryogenic temperatures.

[34] K. J. Ma. Time and amplitude of afterpulse measured with a large size photomultiplier tube. *Nuclear Instruments and Methods A*, 2009.

[35] J.E.McMillan. Neutron shielding for particle astrophysics experiments. *arXiv:physics/0510186*, 2008.

[36] D. Mei. Evaluation of ($\alpha$, n) induced neutrons as a background for dark matter experiments. *Astroparticle Physics*, 2009.

[37] Provided by Bjoern Lehnert, DEAP Collaboration.

[38] E. Segreto. Evidence of delayed light emission of tetraphenyl-butadiene excited by liquid-argon scintillation light. *Physical Review C*, 91(3), Mar 2015.

[39] C. J. Stanford. Alphas and surface backgrounds in liquid argon dark matter detectors. Master's thesis, Princeton University, 2017.

[40] R.J. Holmes. *Use of Nuclear Techniques Use of Nuclear Techniques in the Mineral Industry*. Australian Atomic Energy Commission Reseach Establishment Lucas Heights, 1982.

[41] Provided by Jocelyn Monroe, DEAP Collaboration.

[42] Bryce Marchick. Internal analysis. University of Alberta.

[43] DEAP Collaboration. First results from the deap-3600 dark matter search with argon at snolab. *arXiv:1707.08042v2*, 2017.

[44] DEAP Collaboration. Measurement of the scintillation time spectra and pulse-shape discrimination of low-energy betas and nuclear recoils in liquid argon with deap-1. *Astroparticle Phyiscs*, 2016.

[45] E. Gatti. A new linear method of discrimination between elemantary particles in scintillation counters.

[46] J. Neyman. On the problem of the most efficient tests of statistical hypotheses. *Philosophical Transactions of the Royal Society A: Mathematical, Physical and Engineering Sciences.*, 1933.

[47] M. Akashi-Ronquest. Improving photoelectron counting and particle identification in scintillation detectors with bayesian techniques. *Astroparticle Physics*, 2014.

[48] Provided by Joseph Walding, DEAP Collaboration.

[49] E. Wilson. Probable inference, the law of succession, and statistical inference. *Journal of the American Statistical Association*, 22(158), 1927.

[50] P.-A. Soderstrom. Digital pulse-shape discrimination of fast neutrons and $\gamma$ rays. *arXiv:0805.0692v1*, 2008.

[51] T. Bayes. An essay towards solving a problem in the doctrine of chances. by the late rev. mr. bayes, communicated by mr. price, in a letter to john canton, m. a. and f. r. s. 1763.

[52] Provided by Alistair Butcher, DEAP Collaboration.

[53] G. Verghese A. Oppenheim. *Signals, Systems and Inference*, volume 1 edition. Pearson, 2015.

[54] Jan-Henrik Schmidt-Dencker. Stability of the prompt fraction discriminator in the deap-3600 dark matter experiment. Master's thesis, TU München, 2018.

# Glossary

**PMT trace** , or event trace: PMT signal as a function of time in a single event

**Pulse shape** , or average pulse shape: sum of PMT traces over many events across the PMT array

**keV$_{ee}$** unit for the detector signal intensity in terms of the energy in keV of an electronic recoil which would cause the same intensity

$Q$ Integrated charge normalized by the PMT's single-photoelectron charge

$n_{nsc}$ Estimate for the number of photons and dark hits in a pulse based on a Bayesian analysis. Unless otherwise specified, the MMSE (Minimum mean square error) estimator is used

$F_{prompt}$ Prompt-window-based discriminator using normalized charge (QPE) with a 88 ns prompt window and 10 μs late window

$L_{recoil}$ Likelihood-based discriminator using normalized charge (QPE) as defined in equation 26. Unless otherwise specified, photon weights based on model PDFs as shown in figure 20are used.

$F^{sc}_{prompt}$ Prompt-window-based discriminator using $n_{nsc}$ with a 88 ns prompt window and 10 μs late window. Unless otherwise specified, the MMSE estimate is used.

$L^{sc}_{recoil}$ Likelihood-based discriminator using $n_{nsc}$. Unless otherwise specified, photon weights based on model PDFs as shown in figure 20 and the MMSE estimate are used.

# Acknowledgements